Politecnico di Torino

Politecnico di Torino

Master's Degree Program in Nanotechnologies for ICTs

A.a. 2020/2021

July 2021

Role of Active Electrode Purity in ECM Memristive Devices

Supervisor:

prof. Carlo Ricciardi

Candidate:

Fabio Michieletti

Co-supervisor:

prof. Ilia Valov

Abstract

In last decades the request for progressively larger dataset elaboration has pushed integrated system technology towards its limit. The development of novel technologies and computational paradigms came out to be necessary for overcoming miniaturization issues and fulfilling future applications requests. In this scenario, redox based resistive switching random access memory (ReRAM), based on memristive devices, has proven to be a promising candidate. Memristive devices encode information in the form of internal resistance variation (called resistive switching), caused by the formation and destruction of highly conductive filaments through a thin oxide layer. The fundamental processes underlying switching effect are redox reactions and ionic motion, driven by an electric field. ReRAM shows suitable properties for digital implementations such as non-volatility, short write/read times, low power consumption, long endurance and retention. Moreover, the opportunity to program the resistance state in an analog way and the device capability to show spike timing dependent plasticity pave the way to neuromorphic applications.
Alongside this favourable features, the full understanding of material-properties relation must still be deepened and the lack of complete design rules, together with the intrinsic high variability due to stochastic switching nature, prevents this technology from large scale employment at present.
In this work the impact of copper electrode purity upon the electrical properties of an electrochemical metallization memory (ECM) is investigated. The specific cell structure under study is a metal-insulator-metal (MIM) stack composed by a platinum reference electrode, a Ta_2O_5 insulating layer and a structured copper active electrode. It is produced by sputtering deposition and photolithographic lift-off in a common bottom electrode fashion. The electrical behavior is characterized through I-V sweep measurements, cyclic voltammetry and pulse measurement for set time evaluation. It has been observed that, regarding set time, low purity devices exhibit a faster switching in the low voltage region, where the time limiting process is assumed to be electron transfer. Furthermore, quasi-static figures of merit, namely set voltage, reset voltage, low-resistance state, high-resistance state and resistance ratio show systematic lower variabilities for high purity devices. For this reason, active metal purity engineering can be expected to have a fundamental role in the overcoming of ReRAM variability issue, permitting to approach the target of industrial production.

Contents

Nomenclature

α	Charge transfer coefficient
$\Delta\phi_{ov}$	Overpotential
ΔG_{nuc}	Nucleation energy barrier
ΔG_{ox}	Oxidation activation energy
ΔG_{red}	Reduction activation energy
ΔW_i	Hopping energy barrier
δ	Roughness
λ	Electron mean free path
$\mathbf{x}$, $w(t)$	Memristor state variable
μ	Carrier mobility
ϕ	Magnetic flux
$\rho_{m,Me}$	Electrode mass density
ρ	Electrical resistivity
σ	Electrical conductivity
θ_C	Total reflection critical angle
θ_i	Incidence angle
θ_r	Refraction angle
A	Current amplifier gain
BRS	Bipolar resistive switching
C_{int}	Integration capacitance
c_{ox}	Ion concentration in mol/cm^3
c	Carrier concentration
CC, I_{CC}	Current compliance
CH	Oscilloscope channel
$CMOS$	Complementary metal-oxide-semiconductor
CRS	Complementary resistive switching

CV	Cyclic voltammetry
D_{ox}	Ion diffusion coefficient
e	Electron charge
e	Electric field
ECM	Electrochemical metallization memory
f	Frequency
$FeRAM$	Ferroelectric random access memories
G_0	Quantum of conductance
$G(\phi)$	Memductance
HP	High purity
HRS	High resistance state
I_{el}	Electronic current
I_{ion}	Ionic current
I_{leak}	Leakage current
I_{sens}	Current sensitivity
I_{Tu}	Tunneling current
IoT	Internet of Things
$j_{0,et}$	Exchange current density
j_{hop}	Hopping current density
J_{ion}	Ionic current density
j_{ox}	Oxidation current density
j_{red}	Reduction current density
j_p	Cyclic voltammetry reduction peak current density
k_B	Boltzmann constant
l_{disc}	Disc length
LiM	Logic in Memory
LP	Low purity
LRS	Low resistive state
m_{hop}	Nucleation limited set time - voltage slope
M_{Me}	Electrode molecular mass
m_{nuc}	Nucleation limited set time - voltage slope
m_{ox}	Oxidation limited set time - voltage slope
m_{red}	Reduction limited set time - voltage slope
$MAGIC$	Memristor-aided logic

MIM	Metal-insulator-metal
N_C	Critical ion number
n	Refractive index
P_{el}	Electrical power
p	Specularity factor
PCM	Phase change memory
PM	Pulse Measurements
PVD	Physical vapor deposition
q	Charge
$R_{E,0}$	Critical radius under applied electric field
R_{el}	Electronic current resistance
R_{ion}	Ionic current resistance
R_{leak}	Leakage current resistance
R_{OFF}, R_{HRS}	High resistive state resistance
R_{ON}, R_{LRS}	Low resistive state resistance
R_{th}	Thermal resistance
R_{Tu}	Tunneling current resistance
R_0	Critical radius at equilibrium
R_f	Filament resistance
$ReRAM$	Redox based resistive switching random access memory
RF	Radio frequency
SOI	Silicon on insulator
SR	Sputter rate
SR, ν	Voltage sweep rate
$SRAM$	Static random access memory
$St.Dev.$	Standard deviation
$STT-MRAM$	Spin transfer torque magnetic random access memory
t_{app}	Voltage application time
t_{nuc}	Nucleation time
T_{pause}	Pause time
t_{read}	Read time
t_{reset}	Reset time
t_{rise}	Rising time
t_{set}	Set time

T	Temperature
TCM	Thermochemical memory
URS	Unipolar resistive switching
$V_{\ddot{O}}$	Oxigen vacancies
V_{app}	Applied voltage
V_{disc}	Voltage drop on disc
V_{emf}	Electromotive force voltage
v_{hop}	Ion hopping velocity
V_{read}	Read voltage
V_{reset}	Reset voltage
V_{set}	Set voltage
V_{th}	Threshold voltage
VCM	Valence change memory
XRR	X-rays reflectometry
z	Electron number

List of Tables

List of Figures

Introduction

In last decades the increase in electronic devices performance required for novel applications such as Internet of Things (IoT) and large datasets elaboration has been driven by continuous miniaturization of complementary metal-oxide-semiconductor (CMOS) technology according to Moore's law [1]. This empirical law predicts the exponential increase of transistor numbers and performances per integrated circuit (IC) due to minimum feature size reduction. However, since year 2000, the downscaling process has slowed down owing to intrinsic physical constrains of metal-oxide-semiconductor field-effect transistor (MOSFET) devices. Indeed, dimensions reduction and non-proportional voltage scaling led to the increase of sub-threshold current and power consumption [3] [5]. In order to partially mitigate this issue, high-k materials and different structures such as FinFET and silicon on insulator (SOI) have been employed [6], inevitably causing a progressive increase in production costs that will not be anymore affordable in the near future. Overcome this limit requires a completely new approach to innovation, focusing on co-development of the following system levels: device level, 3D stack integration processes and architecture [3]. In particular, the introduction of novel devices based on different physical mechanisms with respect to FET could overcome miniaturization constrain. Among all the possible candidates for memory application, most promising are redox based resistive switching random access memories (ReRAM) [7], ferroelectric RAM (FeRAM) [8], spin transfer torque magnetic RAM (STT-MRAM) [9] and phase change memories (PCM) [10].

In details, ReRAM is based on memristive devices, components able to store information in the form of internal resistance variation due to reduction-oxidation reactions and ionic motion. Depending on the specific physical and chemical processes involved in resistive switching, they can be divided in three main classes: electrochemical metallization memories (ECM), valence change memories (VCM) and thermochemical memories (TCM) [11]. From the applicative standpoint, ECM and VCM are reported to be the most promising [12]. In several research works, they proved to exhibit low power consumption, low switching time, high scalability, in addition to non-volatility and multiple resistance states

programmability [3] [5]. These features, in principle, pave the way for both old technology replacement and totally new structures and architectures. Regarding memory application, Boukhobza in ref. [13] reported that ReRAM can be competitive with both static random access memories (SRAM) and non volatile NAND flash memories. Table 1 reports a performance comparison between above mentioned technologies in terms of IC area (where F represents the minimum feature dimension achievable through lithography), operative voltage, read time (t_{read}), write time (t_{write}), write energy per bit, retention (i.e. the time lapse for which a stored bit can be maintained) and endurance in terms of write-erase operation number before failure [14]. It can be observed that ReRAM, with respect to Flash memories, show significant lower write and read times. Jung *et al.* reported in ref. [15] an 8 GB architecture achieving up to 88% lower latency. With respect to SRAM, ReRAM demonstrate to be superior in mignaturization only, with significant higher latency. In other studies, such as the one from Dong *et al.* in ref. [16], also lower power consumption is reported. This result suggests the possibility of utilizing memristive technology as volatile memories for applications in which power consumption is a dominant constraint.

Performance Comparison			
Technology	SRAM	NAND Flash	ReRAM
Area	$> 100F^2$	$< 4F^2$	$< 4F^2$
Voltage	< 1 V	< 10 V	< 3 V
$\mathbf{t_{read}}$	~ 1 ns	~ 10 µs	< 10 ns
$\mathbf{t_{write}}$	~ 1 ns	~ 100 µs	< 10 ns
Write energy	$\sim 1 \frac{fJ}{bit}$	$\sim 10 \frac{fJ}{bit}$	$\sim 100 \frac{fJ}{bit}$
Retention	-	10 y	10 y
Endurance	$> 10^{16}$	$> 10^4$	$\sim 10^{12}$

Table 1: *Performance comparison between SRAM, NAND flash and ReRAM technologies. F represents the minimum feature dimension achievable through lithography. Adapted from [14].*

Also logic units based on memristor-aided logic (MAGIC) architecture can be exploited [17], even if not for high performance computation applications where they are shown to be not competitive [5]. This could open the door to Von Neumann bottleneck overcome by performing Logic in Memory (LiM) for simple logical operations [18] and also 3D integration directly on top of the CPU (enabled by low temperature process) [19], reducing interconnection length. Analog behavior instead, permitted by an almost continuous range of resistances achievable, attracted attention for completely new computing paradigms.

For example, by programming the resistances of a crossbar array, it is possible to solve various mathematical problems (such as linear systems and eigenvalues problems) in one shot thanks to Ohm's law [20]. The most fundamental analog implementation is the *in situ* storing and tuning of synaptic weight in Artificial neural networks thanks to non-volatility and spike-timing-dependent plasticity [5]. As reported by Zoppo *et al.* in ref. [21] it is possible to design completely analog recurrent neural networks with efficiency higher than 90% in pattern recognition and reconstruction.

Despite the promising properties of memristive devices, many issues not permit market implementation yet. In particular, stochastic nature of switching leads to unbearable variability both between devices and also from cycle to cycle. [22] For this reason a huge characterization work must still be done in order to have a deep knowledge of material-properties-performance relation, mitigate non-idealities and formulate complete design rules.

This work will focus on the study of copper electrode metal purity influence onto device characteristics of an ECM cell. In details, memristive structure that will be analyzed is a $Pt/Ta_2O_5/Cu$ stack, where platinum acts as inert electrode, tantalum oxide as switching layer and Cu as active electrode. The first chapter will present an overview on memristive devices circuit theory and physical mechanisms at the basis of resistive switching. In the second chapter, production process and experimental methods will be illustrated. Results elaboration and discussion will be exposed in the third chapter, followed by a conclusive result summary and an outlook on desirable further research deepening.

Chapter 1

Theoretical fundamentals

Memristive devices are two-terminals nonvolatile elements whose resistance can be switched between two or more values, called *resistance states*. Their basic structure is depicted in figure 1.1 and is composed by a metal-insulator-metal (MIM) stack. Application of an external voltage induces a local rearrangement of atomic defects in the insulator - also called *switching layer* - which leads to formation and destruction of highly conductive paths. Cell state is then read by applying a suitable voltage (V_{read}) and recording current flowing. In this sense, ionic currents are responsible for cell resistance state variation, while electronic one is measured to probe it.

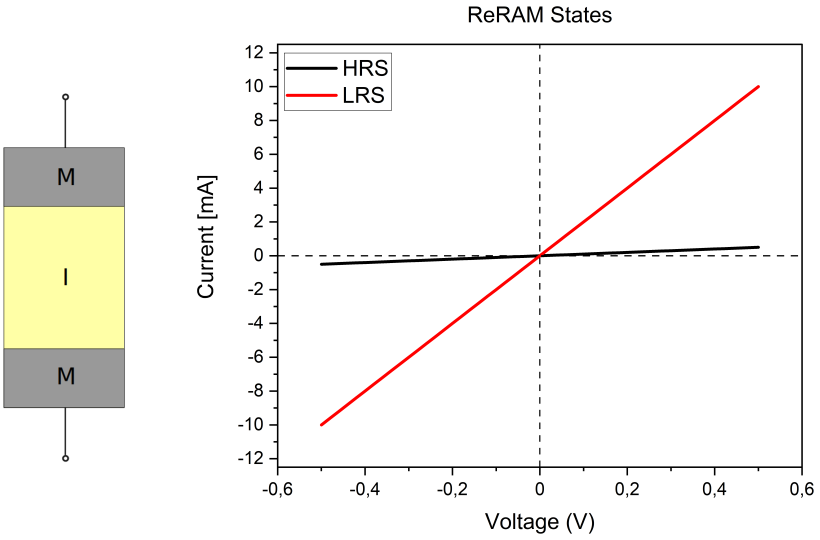

Figure 1.1: *Memristive device MIM structure (left) and example of two possible resistance states (right)*

Most important parameters, defining device properties, are:

- *OFF resistance (R_{OFF} or R_{HRS})*: is the ReRAM cell resistance value in *high resistance state (HRS)*;
- *ON resistance (R_{ON} or R_{LRS})*: is the ReRAM cell resistance value in *low resistance state (LRS)*;
- *resistance ratio*: is the ratio between HRS and LRS resistances ($\frac{R_{HRS}}{R_{LRS}}$);
- *SET voltage (V_{set})*: is the voltage at which transition from HRS to LRS (*write* operation) is triggered;
- *RESET voltage (V_{reset})*: is the voltage at which transition from LRS to HRS (*erase* operation) is triggered;
- *SET time (t_{set})*: is the time laps between application of a constant voltage ad the write event, defining so write speed;
- *endurance*: is the number of set-reset cycles for which each resistance state assume a stable constant value, or lie in an acceptable confidence interval;
- *retention time*: is the time for which a resting cell can maintain a programmed state.

According to Ielmini *et al.* in ref. [23], several devices classifications can be performed based on their properties. A first one concerns switching polarity - i.e. the sign of V_{set} and V_{reset} - as shown in figure 1.2. *Unipolar resistive switching (URS)* is characterized by the same polarity of write and erase voltages. When cell lies in HRS, increasing applied voltage over a threshold value V_{th1} will cause a set event. From this point on, by stressing with a voltage higher then V_{th2}, device will reach again HRS. This polarity independence suggests heating as driving parameter for switching [23]. In *Bipolar resistive switching (BRS)*, V_{set} and V_{reset} have opposite voltage polarities, indicating a voltage driven process. As reported by Ielmini *et al.* in ref. [23], this is the class for which most literature is present. *Complementary resistive switching (CRS)* can be obtained by connecting two BRS cells in antiserial fashion [24] or by employing specific single cell production processes [25]. Devices belonging to this group can be set by using a voltage $V_{set}>V_{th2}$, reset with $V_{reset}<V_{th4}$ and read in the window between V_{th1} and V_{th2}.
Memristive devices can also be classified geometrically, according to the spatial distribution of the switching process, as shown in figure 1.3. Considering vertical direction,

switching can take place at M-I interfaces, in the center or along the entire path. For what concerns lateral geometry, the event can be confined in a single position (*filamentary switching*) or can spread along all the contact area (*area-dependent switching*). This clear separation is however a simplification, since more than one filament can be present or lateral confinement can be in an intermediate extension area.

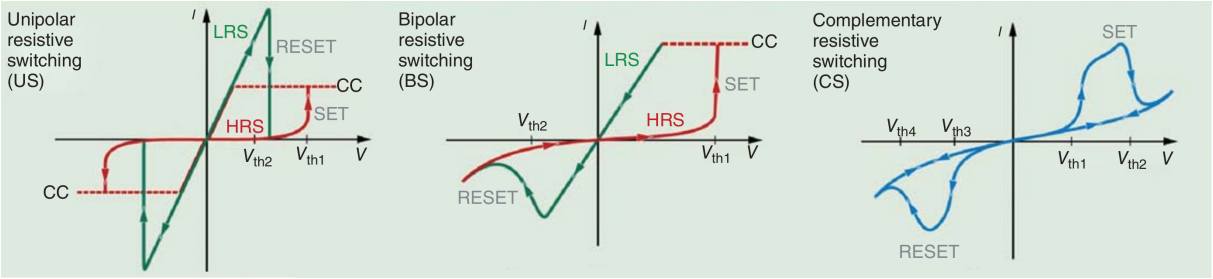

Figure 1.2: *Schematics of device classification based on switching polarity. Adapted from [23].*

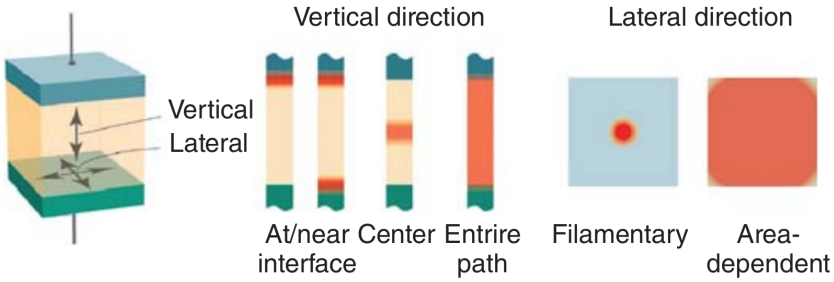

Figure 1.3: *Schematics of device geometrical classification [23].*

A final classification can be made according to microscopic physical and chemical processes responsible for resistance switching.

- *Electrochemical metallization memories (ECM)*: the conductive filament is formed by anodic dissolution of electrochemically active electrode metal and successive ions migration and crystallization onto the inert counter electrode. LRS is obtained when filament connection is well established between the electrodes, therefore shortening them. This devices show typically bipolar and filamentary switching.

- *Valence change memories (VCM)*: conductive path is formed by a stoichiometric change in insulating oxide matrix due to oxygen vacancies ($V_{\ddot{O}}$) migration. As a result, a virtual cathode starts approaching the anode until current can flow thanks to tunneling events or contact. Despite bipolar and filamentary switching is usually observed, in some cases area dependence can be present.

- *Thermochemical memories (TCM)*: a controlled partial dielectric breakdown is induced by electrical power flow. During this event, a filament is formed, which can be composed by metal atoms, impurities or oxide heating products. Filament is then broken again by power dissipation induced melting. As a result, this device class is filamentary and unipolar.

The first section of this chapter will describe memristive devices circuit theory and electrical modeling. In the second section, switching physical mechanisms will be detailed. Only ECM and VCM cells will be deepened, since showed theirselves to be the most promising candidate for practical implementations and solely ECM cells are experimentally investigated in this thesis work.

1.1 Circuit theory

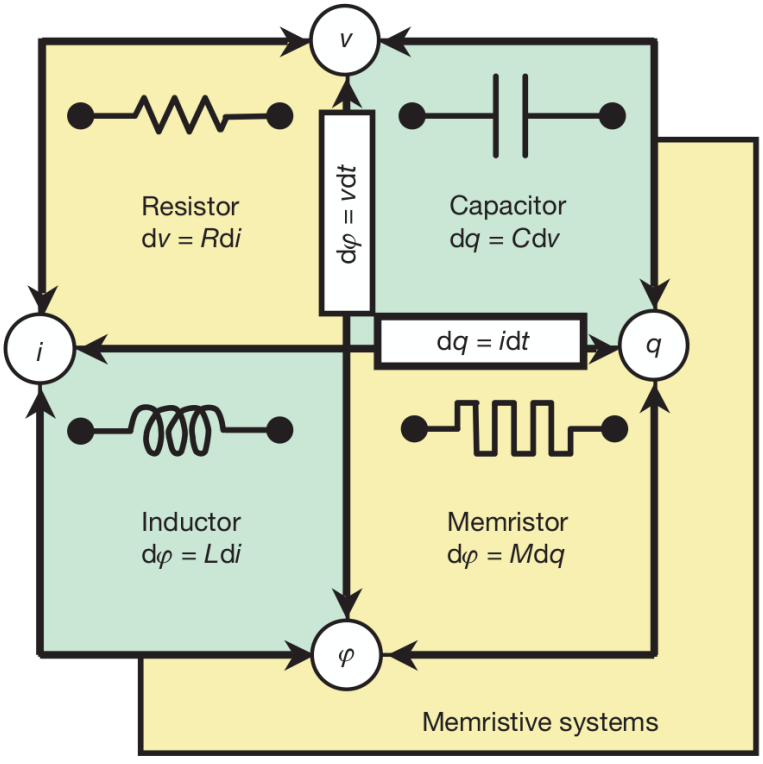

Figure 1.4: *Schematics of fundamentals circuital elements and respective electrical variables relations [26].*

Memristive devices have been, in some cases, associated to *memristor* (from memory resistor) concept. In 1971 Leon Chua hypothesised, for symmetry principle, its existence

as the fourth fundamental electric element besides resistor, capacitor and inductor [27]. As shown in figure 1.4, it links charge (q) and magnetic flux (ϕ), which is the voltage integral over time (eq. 1.2). Current-voltage relation is reported in eq. 1.1 (dynamical system equation), where G(ϕ) is the *memductance* (reciprocal of the *memristance*). Its name comes from memory conductance, since its value depends on the previous history of the component. Memristor I-V characteristics has the shape of a pinched hysteresis loop, which tends to collapse into a linear behavior for high frequencies, as shown in figure 1.5. This is due to component impossibility of following stress variation. [27]

$$I = G(\phi) \cdot V \tag{1.1}$$

$$\dot{\phi} = V \tag{1.2}$$

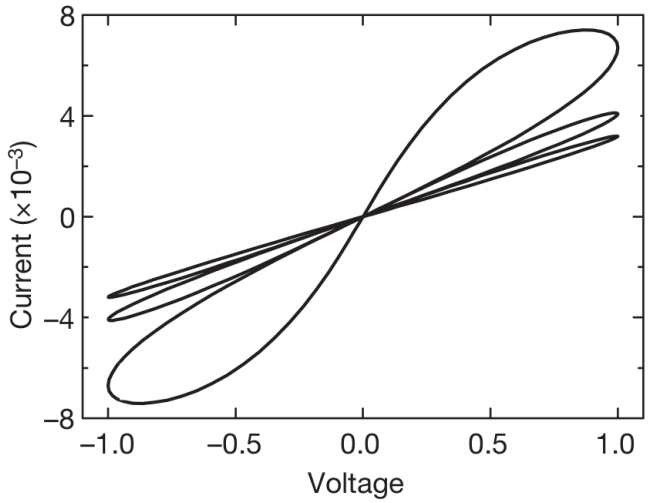

Figure 1.5: *Example of typical I-V pinched characteristics and hysteresis collapse due to frequency increase. Adapted from [26].*

Despite the attractiveness of this association, it has been demonstrated both analytically [28] and experimentally [23] that memristive devices cannot be considered memristors. A generalization of system equation must be performed, as done in eq. 1.3 - 1.4 [23]. Here, conductance depends on a general state variable describing cell state variation ($\boldsymbol{x}$), applied voltage and time (t). State variable accounts for all the complex microscopic processes taking place during operations.

$$I = G(\mathbf{x}, V, t) \cdot V \tag{1.3}$$

$$\dot{\mathbf{x}} = f(\mathbf{x}, V, t) \tag{1.4}$$

Moreover, a real memristive device behavior is a consequence of many effects, which are associated to different circuit elements. For this reason, memristive device definition must be extended in order to comprise them. For ECM cells, for example, three current contributions must be considered, namely electronic (I_{el}), ionic (I_{ion}) ad leakage (I_{leak}) with their respective resistances (R_{el}, R_ion, R_{leak}). Moreover, the MIM structure is the same of a capacitor with its own capacitance C. Finally, the formation of an electrical double layer at electrode-oxide interface generates an electromotive force which can be modeled as a voltage source (V_{emf}). This effect is called *nanobattery effect* [29] and causes device to become partially active. Figure 1.6 reports electrical schematics of the generalized cell described above.

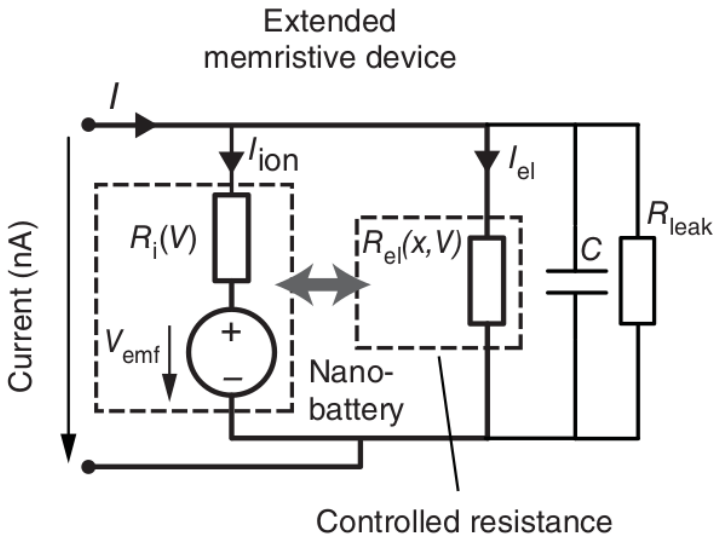

Figure 1.6: *Circuital scheme of the extended memristive device. Adapted from [29].*

1.1.1 Compact models

In order to predict by simulations the behavior of a certain device, it is important to build compact models. This is fundamental both for industrial application - where performances estimation are needed for optimization - and for research, especially when memristive devices are used for studying new functionalities in complex architectures. Figure 1.7 reports the three possible approaches for modeling.

- *Black box* models are based on reproducing experimental results without accounting for internal physical processes. They have the advantage of being very compact and easy to implement, but can fail in predicting behaviors under new conditions.
- *White box* models are built on the complete physical description of device kinetics. They can be very accurate and general, but requires the full knowledge of cell switching mechanisms. Since wide research must still be done in order to satisfy this requirement, white box approach cannot be used for memristive devices at present.
- *Gray box* approach is intermediate between previous two and partial device dynamic knowledge is complemented with measurement results. This is the most suitable method for memristive devices modeling.

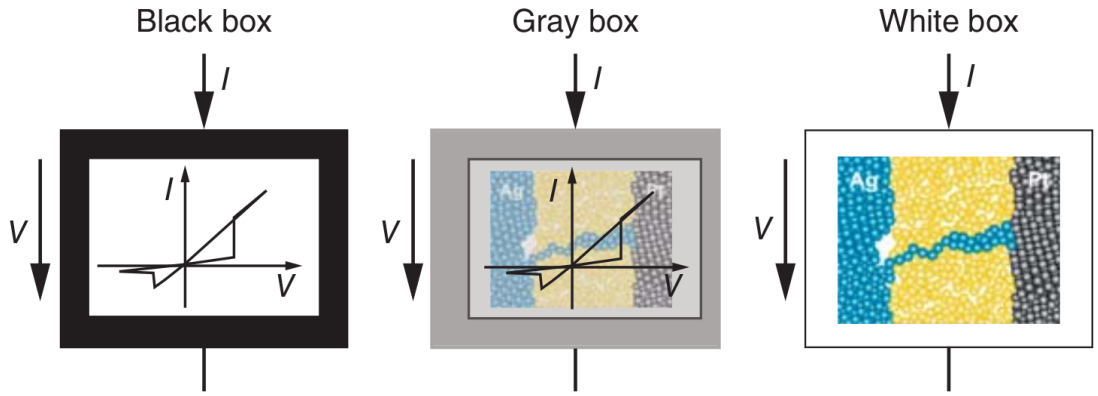

Figure 1.7: *Figurative representation of memristive black, gray and white box models [23].*

In the following will be firstly presented a black box model proposed by Strukov *et al.* in ref. [26]. Then, two gray box models will be exposed: one for ECM cells proposed by Linn *et al.* in ref. [30] and one for VCM cells proposed by Abdalla *et al.* in ref. [31].

1.1.1.1 Black box general model

Figure 1.8 depicts the general concept at the basis of this model. To switching layer of length D are associated two regions divided by a moving interface. The first region of length $w(t)$ is composed by a highly conductive doped semiconductor with resistance R_{ON}, while the second one of length $D-w(t)$ is composed by a low conductivity undoped semiconductor of resistance R_{OFF}. Total device resistance is the series connection of R_{ON} and R_{OFF}, whose values are dependent on barrier position and so time dependent.

I-V relation is reported in eq. 1.5 in a current controlled fashion, while eq. 1.6 describe barrier displacement as a function of current flow. In this example, barrier position $w(t)$ represents the state variable.

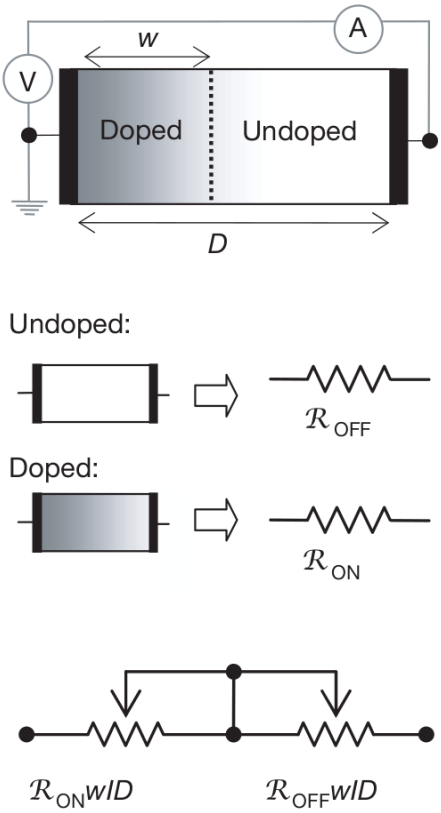

Figure 1.8: *Schematic representation of the Strukov's model. Adapted from [26].*

$$v(t) = \left(R_{ON} \frac{w(t)}{D} + R_{OFF} \left(1 - \frac{w(t)}{D} \right) \right) i(t) \tag{1.5}$$

$$\frac{dw(t)}{dt} = \mu_V \frac{R_{ON}}{D} i(t) \tag{1.6}$$

An expansion of this model has been made by Yakopcic *et al.* in ref. [32] by considering threshold switching effect and the barrier slowing down when approaching limiting values. It must be noticed that both this models are purely conceptual and completely nonphysical, since device stoichiometry is not respected.

1.1.1.2 Gray box model for ECM devices

Figure 1.9 shows equivalent circuit of the ECM cell implemented in this model. A detailed description of the conductive mechanism modeled will be provided in section 1.2.1.4, while, in the following, a brief overview will be made in order to understand mathematical implementation.
In a situation in which a short gap divides the filament from the electrode, total current flowing (I_{el}) is the sum of a faradaic component (I_{ion}) and of one tunneling through the gap (I_{Tu}), as reported in eq. 1.7. Gap width (x) is the system state variable, whose time evolution is described by Faraday law [33] in eq. 1.8. Here M_{Me} is the molecular mass of electrode material, $\rho_{m,Me}$ its mass density, z the ionization number and J_{ion} the ionic current density. Mathematical integration of this equation is circuitally performed by the auxiliary circuit where V_w corresponds to x, current I to the integrated value and $C_{int} = 1$ to the integration capacitance.

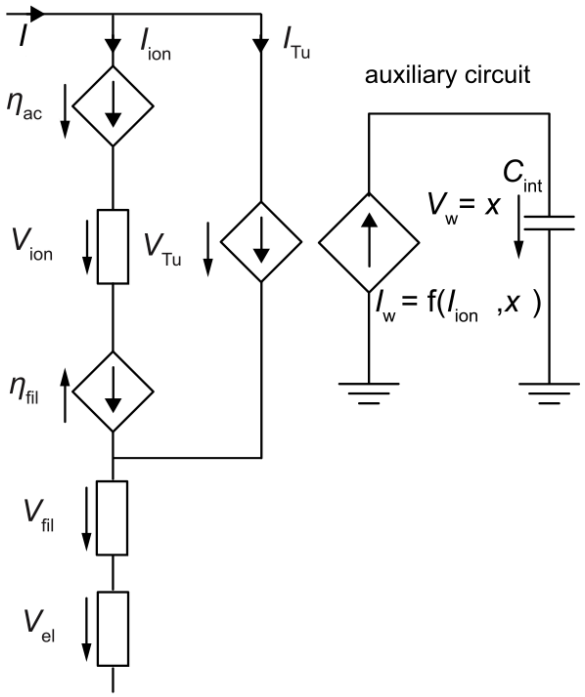

Figure 1.9: *Circuital design of the ECM device grey box model proposed by Linn et al. Adapted from [30].*

$$I_{el} = I_{Tu}(x, V) + I_{ion}(x, V) \tag{1.7}$$

$$\frac{dx}{dt} = -\frac{M_{Me}}{ze\rho_{m,Me}} J_{ion} \tag{1.8}$$

Ionic current is evaluated through Tafel equation. At filament/insulator interface, it is expressed by eq. 1.9 - 1.10, respectively for set and reset branches. At active electrode/insulator interface instead, it is expressed in eq. 1.11 - 1.12, respectively for set and reset branches again. In these equations, e is the electron charge, k_B the Boltzmann constant, T the temperature, j_0 the exchange current density, α the charge transfer coefficient, A_{fil} the filament/insulator interface area, A_{ac} the active electrode/insulator interface area, $\Delta V_{set,fil}$, $\Delta V_{set,ac}$ respectively filament/insulator and active electrode/insulator set overpotentials, while $\Delta V_{reset,fil}$, $\Delta V_{reset,ac}$ respectively filament/insulator and active electrode/insulator reset overpotentials.

$$I_{fil}(V \geq 0) = j_0 A_{fil} \left(e^{-\frac{\alpha e z}{k_B T} \Delta V_{set,fil}} - 1 \right) \tag{1.9}$$

$$I_{fil}(V < 0) = j_0 A_{fil} \left(e^{\frac{(1-\alpha) e z}{k_B T} \Delta V_{set,fil}} - 1 \right) \tag{1.10}$$

$$I_{ac}(V \geq 0) = j_0 A_{ac} \left(e^{\frac{(1-\alpha) e z}{k_B T} \Delta V_{set,ac}} - 1 \right) \tag{1.11}$$

$$I_{ac}(V < 0) = j_0 A_{ac} \left(e^{-\frac{\alpha e z}{k_B T} \Delta V_{set,ac}} - 1 \right) \tag{1.12}$$

Finally, tunnel current is evaluated through Simmons equation [34], reported in eq. 1.13. Here, m_{eff} is the effective tunneling mass, ΔW_0 the height of tunneling barrier, h the Planck's constant and V_{Tu} the tunneling voltage evaluated as $V_{Tu} = \eta_{ac} - \eta_{fil} + I_{ion} R_{ion}$. R_{ion} is the ionic resistance of the gap evaluated in eq. 1.14, where ρ_{ion} is the switching layer ionic resistivity and A_{ion} the area of ionic drift.

$$I_{Tu} = \frac{3\sqrt{2 m_{eff} \Delta W_0}}{2x} \frac{e}{h}^2 e^{-\frac{4\pi x}{h}\sqrt{2 m_{eff} \Delta W_0}} A_{fil} V_{Tu} \tag{1.13}$$

$$R_{ion} = \frac{\rho_{ion} \cdot x}{A_{ion}} \tag{1.14}$$

This model is completely composed by equations describing physical switching mechanism. However, it must rely on measurement results for the numerical evaluation of material and interfacial parameters.

1.1.1.3 Gray box model for VCM devices

VCM simulation is completely based on tunneling current trough a variable gap x, which is the state variable also in this case. Current I is evaluated by means of tunneling equation reported in eq. 1.15 and all the parameters are obtained through equations from 1.16 to 1.23. Here A is the filament area, ϕ_0 the tunneling barrier height in electronvolts, V_g the voltage across the gap, ϵ_0 the vacuum permittivity and k the dielectric constant of the material. Equations 1.24 and 1.25 illustrate, instead, the state variable dynamic.

$$I = \frac{J_0 A}{\Delta x^2} \cdot \left(\phi_I \cdot e^{-B\sqrt{\phi_I}} - (\phi_I + e|V_g|) \cdot e^{-B\sqrt{\phi_I + e|V_g|}} \right) \tag{1.15}$$

$$\phi_I = \phi_0 - e|V_g| \frac{x_1 + x_2}{x} - \frac{1.15\lambda x}{\Delta x} \ln\left(\frac{x_2(x - x_1)}{x_1(x - x_2)} \right) \tag{1.16}$$

$$B = \frac{4\pi \Delta x \sqrt{2m}}{h} \tag{1.17}$$

$$x_1 = \frac{1.2\lambda x}{\phi_0} \tag{1.18}$$

$$x_2 = x_1 + x\left(1 - \frac{9.2\lambda}{3\phi_0 + 4\lambda - 2e|V_g|} \right) \tag{1.19}$$

$$\lambda = \frac{e^2 ln(2)}{8\pi k \epsilon_0 x} \tag{1.20}$$

$$J_0 = \frac{e}{2\pi h} \tag{1.21}$$

$$\Delta x = x_2 - x_1 \tag{1.22}$$

$$V_g = V_{device} - I \cdot R_s \tag{1.23}$$

$$\dot{x}(I > 0) = f_{off} \sinh\left(\frac{|I|}{I_{off}} \right) \exp\left(-\exp\left(\frac{x - a_{off}}{x_c} - \frac{|I|}{b} \right) - \frac{x}{x_C} \right) \tag{1.24}$$

$$\dot{x}(I < 0) = -f_{on} \sinh\left(\frac{|I|}{I_{on}} \right) \exp\left(-\exp\left(\frac{a_{on} - x}{x_c} - \frac{|I|}{b} \right) - \frac{x}{x_C} \right) \tag{1.25}$$

All the not mentioned parameters are extracted from cell fitting. This characteristic causes the model to be less physical then the one described in section 1.1.1.2, revealing

its proximity to black box approach. It is not useful for predicting any physical specific behavior. This shows the importance of having the most complete possible knowledge of cell inner dynamic, in order to neglect specific effects in simulations only when it is feasible.

1.2 Physical description

In this section, a detailed description of memristive devices working principles and internal dynamics will be exposed. In a first part, electrochemical metallization memories will be deepened, while in the second one valence change memories. It must be noticed that, despite general agreement on many evidences, wide research must still be done for complete comprehension of underlying physical processes.

1.2.1 Electrochemical metallization memories

Electrochemical metallization memories are a class of devices with a structure composed by an electrochemically active metal electrode, a solid electrolyte or an insulator layer (such as a metal oxide) and an inert electrode. By applying a voltage stress, a filament composed by active metal atoms can be formed and dissolved, causing resistive switching.

1.2.1.1 Working principle

Figure 1.10 shows a typical ECM I-V sweep characteristics together with representations of filament dynamics during switching. In particular a $Pt/Ta_2O_5/Cu$ device is represented, which is the one studied in this work. In the following, a description of each operation step of this cell is provided, but it is valid for every standard ECM cell. [35]

A) Initially, device is in pristine state.

B) During the application of a positive voltage on the active electrode, Cu atoms starts anodic dissolution into the oxide, following oxidation reaction 1.26.

$$Cu \rightarrow Cu^{+} + e^{-} \tag{1.26}$$

Cu cations then drift towards inert electrode driven by electric field.

C) Once reached Pt electrode, Cu ions nucleates at the interface undergoing voltage assisted reduction 1.27.

$$Cu^{+} + e^{-} \rightarrow Cu \tag{1.27}$$

Cu protrusions so created produce a local intensification of electric field, favoring successive growth in this region. The repetition of this process forms a filament which, when contacting both electrodes, causes cell switching to LRS. A *current compliance (CC)* if forced in order to avoid irreversible oxide breaking due to excessive power dissipation.

D) Voltage is decreased and device behaves as a low value resistor.

E) Voltage is reversed and filament atoms are again dissolved, drift towards Cu electrode and oxidize again. This causes return to HRS due to filament breaking.

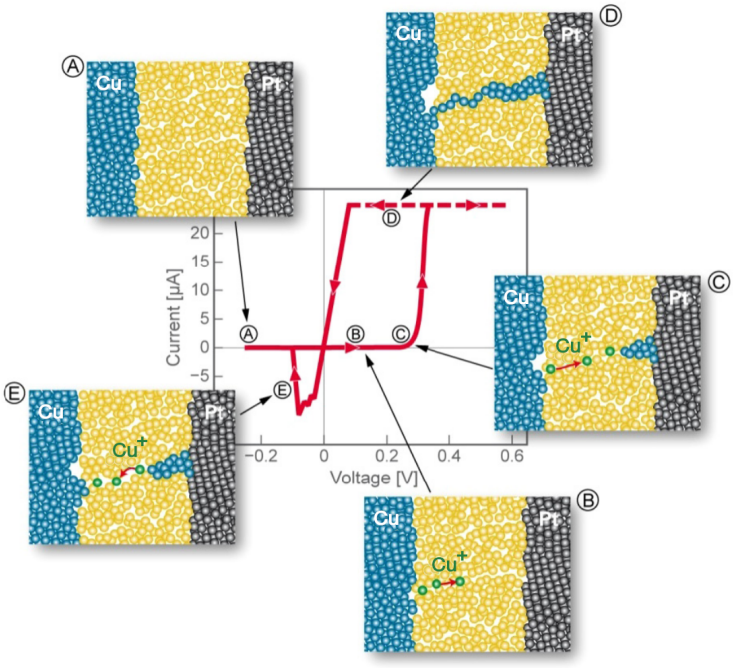

Figure 1.10: *Working principle of ECM cells. Adapted from [35].*

1.2.1.2 Electroforming

Before obtaining stable resistive switching operation, device must undergo an initial process called *electroforming* [35]. It consists in a positive sweep with voltage significantly higher with respect to successive set voltages, as shown in figure 1.11.

During this step, some filaments starts their growth, until one of them connects the electrodes (with dynamic described in section 1.2.1.1). As it can be observed in figure 1.12, by applying the first reset pulse, only a small filament portion at the active electrode/oxide interface is dissolved. Next switching cycles will then make the filament close (LRS) and open again (HRS) this short gap only. [36].
Electroforming is reported to be mandatory in every ECM cell, unless specific production processes are implemented, as in the case of ref. [37].

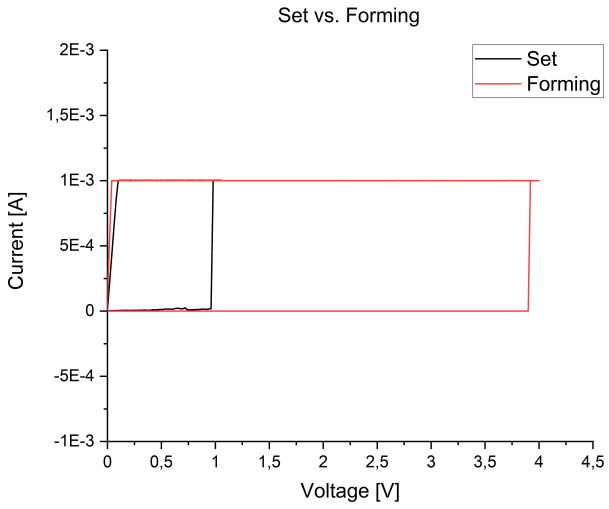

Figure 1.11: *Comparison between setting and electroforming sweeps.*

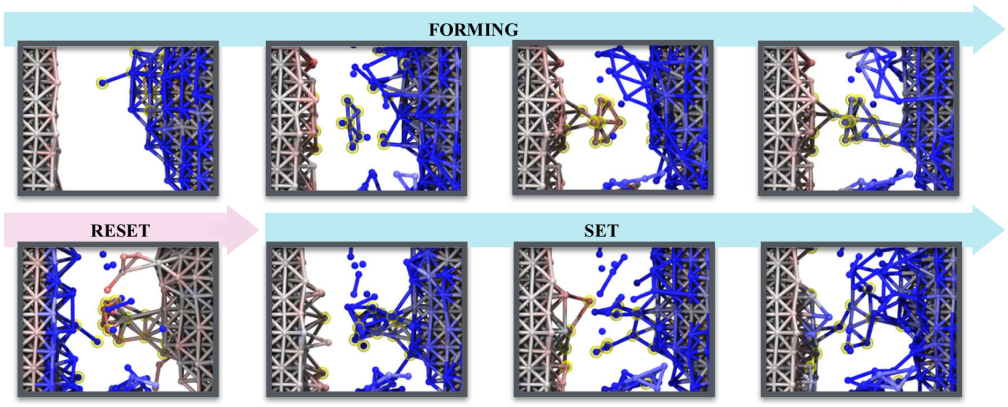

Figure 1.12: *Simulation of forming, set and reset processes. Red color indicates negatively charged atoms, blue color positively charged ones. It can be clearly noticed that set transition involves a significantly shorter path in the oxide with respect to forming. Adapted from [36].*

1.2.1.3 Switching kinetics

The possibility of detecting cell resistance and negligibly influence its state, by applying a small voltage, is ensured by set time nonlinear dependence on voltage [38]. Three processes are reported to be rate limiting, each of which in different potential ranges. Namely, *filament nucleation* is limiting at small, redox *electron-transfer* at intermediate and *ion migration* at high voltages [11]. Boundaries between prevailing processes are dependent on device under test and more then one can be rate limiting at the same potential.
Filament nucleation involves a process of electrocrystallization, where the filament nucleates through reduction at the inert electrode/oxide interface, assisted by electric field. A stable filament can form only if possesses a certain minimum number of ions N_C, and so a minimum radius R_0 (*crytical radius*). Figure 1.13 shows the free energy profile as a function of nucleus radius. It can be observed that field application modifies the curve, leading to a critical radius lowering ($R_{E,0}$). Karpov *et al.* proposed this effect as one of the possible origins of threshold switching in ref. [39]. Equation 1.28 describes the exponential dependence of nucleation time (t_{nuc}) on the nucleation overpotential ($\Delta\phi_{ov}$) and so on the applied voltage. ΔG_{nuc} is the nucleation energy barrier. The first exponential represents the classical equation for zero-field nucleation time, while the second describe barrier lowering and associated critical radius decreasing. [11]

$$t_{nuc} \propto e^{\frac{\Delta G_{nuc}}{k_B T}} \cdot e^{-\frac{(N_C+\alpha)ze}{K_B T}\Delta\phi_{ov}} \tag{1.28}$$

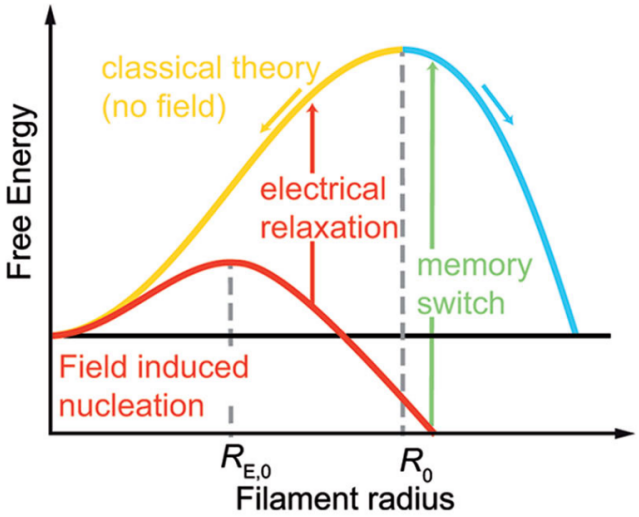

Figure 1.13: *Filament nucleation free energy as a function of filament radius. Red curve shows the relation variation under electric field application [11].*

Electron-transfer rate limitation is associated to reductions and oxidations at metal/oxide interfaces. Figure 1.14 depicts the free oxidation energy profile of an electrode atom (left valley) and reduction one for a metal ion in the oxide close to the interface (right valley). Gray curve represents the equilibrium situation and ΔG^0_{ox} and ΔG^0_{red} are respective activation energies. In this situation, oxidation current density (j_{ox}) and reduction current density (j_{red}) are opposite and both equal in magnitude (the so called *exchange current density ($j_{0,et}$)*). Resulting net current is therefore null. Under the application of a voltage, and so of an overpotential $\Delta\phi_{ov}$ ($\Delta\eta$ in the picture), electrode Fermi energy is shifted of a value $-ze\Delta\phi_{ov}$. Taking into account the charge transfer coefficient, activation energies vary according to equations 1.29 and 1.30, resulting in the red energy profile. Reduction reaction is favored in this exemplary case, but it is dependent on voltage polarity. [11][40]

$$\Delta G_{ox} = \Delta G^0_{ox} + (1-\alpha)ze\Delta\phi_{ov} \tag{1.29}$$

$$\Delta G_{red} = \Delta G^0_{ox} + \alpha ze\Delta\phi_{ov} \tag{1.30}$$

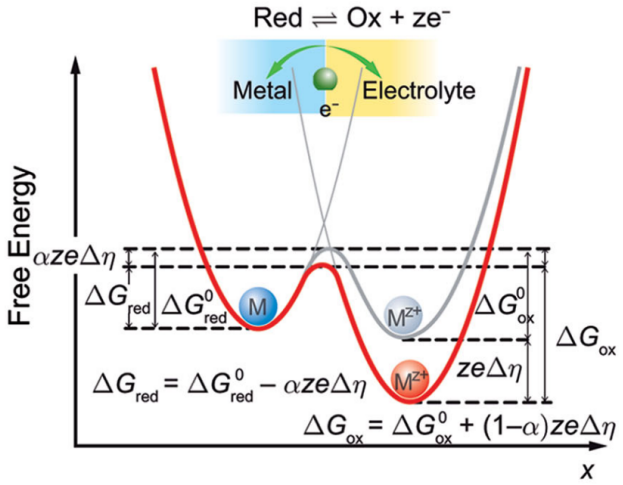

Figure 1.14: *Redox free energy profile of an interfacial metal atom. Red curve shows the barrier variation under electric field application [40].*

Resulting net current density has an exponential dependence on applied voltage described by the Butler-Volmer equation in eq. 1.31. Positive term is related to oxidation, which dominates for $\Delta\phi_{ov} > 0$, while negative term is related to reduction and dominates in the opposite situation.

$$J = J_0 \left(e^{(1-\alpha)\frac{ze\Delta\phi_{ov}}{k_B T}} - e^{-\alpha\frac{ze\Delta\phi_{ov}}{k_B T}} \right) \tag{1.31}$$

Ion migration is the ionic displacement in the oxide matrix, under an electric field application, which takes place when metal cation travels from the electrode to the filament and vice versa. Movement is due to hopping between insulator sites by overcoming the energy barrier $\Delta W_{i,0}$, which is constant in perfect crystal approximation. With the latter, also the hopping distance between sites (a) can be considered constant. In absence of electric field E, hopping is thermally activated and directionally casual. This situation is shown on the top of figure 1.15, where $\Delta W_a = \Delta W_{i,0}$. Under the application of an electric field (bottom of figure 1.15), energy barrier is altered according to equation 1.32, breaking symmetry and inducing a net ion flow.

$$\Delta W_i = \Delta W_{i,0} + \frac{1}{2} zeaE \tag{1.32}$$

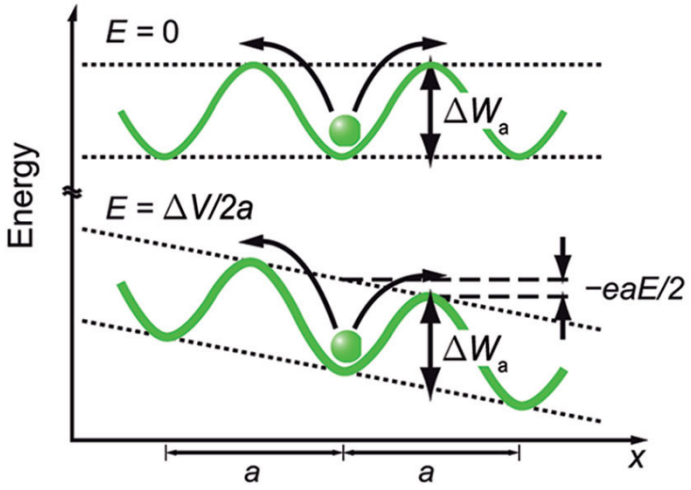

Figure 1.15: *Potential profile for an ion in the switching layer without (top) and with (bottom) the application of an electric field during hopping [40].*

Resulting current follows the Mott-Gurney law for ion hopping, reported in eq 1.33, where f is the electrical stimulus frequency [11]. Considering eq. 1.34, and that the hyperbolic sine can be approximated as an exponential for high electric fields, hopping velocity can be shown to assume the form expressed in eq. 1.35

$$j_{hop} = 2zecafe^{-\frac{\Delta W_{i,0}}{k_B T}} \sinh\left(\frac{aze}{2k_B T} E\right) \tag{1.33}$$

$$v = \frac{j}{zec} \tag{1.34}$$

$$v_{hop} = afe^{-\frac{\Delta W_{i,0}}{k_B T}} e^{\frac{aze}{2k_B T}E} \tag{1.35}$$

Following the approach used by Menzel *et al.* in ref. [41], ion migration time (t) through filament gap x can be evaluated as in eq. 1.36. Similar consideration for electron transfer, together with eq. 1.34, leads to exponential dependence of set time on applied voltage in all three rate limiting processes.

$$t = \frac{x}{v} \tag{1.36}$$

As shown in figure 1.16, by evaluating set time with pulse measurements at different pulse voltages (which will be described in details in section 2.2.3), it is possible to clearly identify three regions with respective rate limiting processes described above. For each of them, logarithmic plot slopes are reported in equations from 1.37 to 1.40, where m_{nuc} is nucleation process slope, m_{ox} oxidation, m_{red} reduction and m_{hop} ion migration. It must be underlined that oxidation and reduction equations are valid only if relative reaction is the only one present, which is never the case.

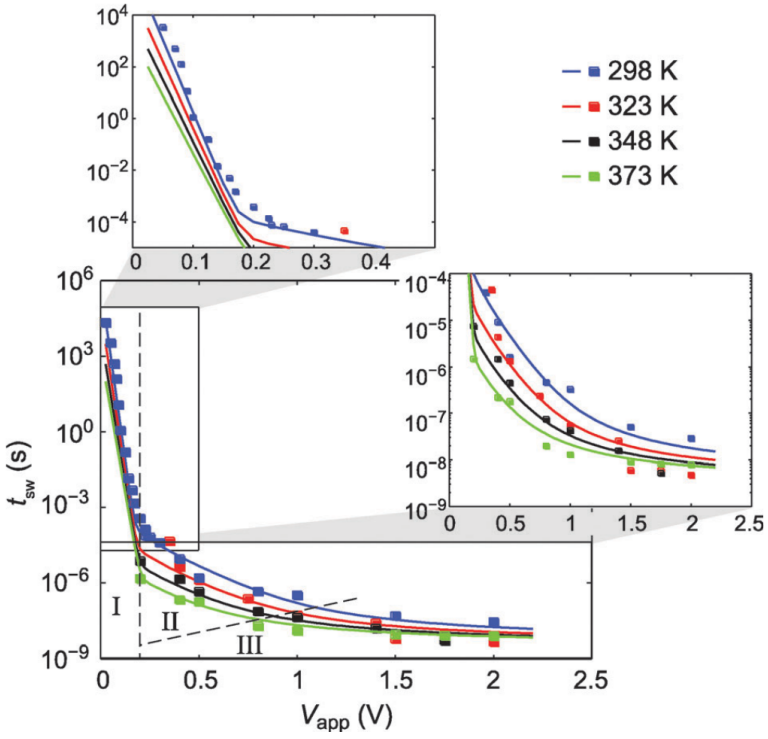

Figure 1.16: *ECM set time characteristics as a function of applied voltage at different temperatures. Nucleation is rate limiting in section I, electron transfer in section II and ion hopping in section III [38].*

$$m_{nuc} = -\frac{(N_c + \alpha)ze}{k_B T} \tag{1.37}$$

$$m_{ox} = \frac{(1 - \alpha)ze}{k_B T} \tag{1.38}$$

$$m_{red} = -\frac{\alpha ze}{k_B T} \tag{1.39}$$

$$m_{hop} = -\frac{aze}{2k_B T w} \tag{1.40}$$

1.2.1.4 Conductivity analysis

The wide interval of resistance states that a memristive device can assume cannot be justified by a single phenomenon. For this reason, two different state variables are proposed by Ielmini *et al.*: tunneling gap and filament diameter. They are described respectively by the so called *variable-gap* and *variable-diameter* models. [23] Figure 1.17 reports resistance values simulated by means of both models. It can be observed that filament lateral growth can justify resistances up to 10^4-$10^5\,\Omega$, while higher values must be adducted to gap variation.

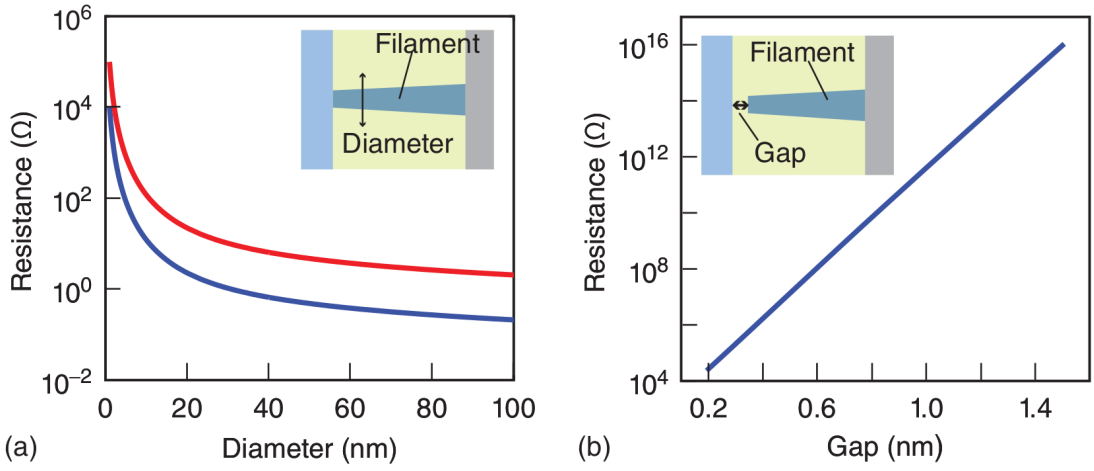

Figure 1.17: *Resistance values evaluated for variable-diameter (left) and variable-gap (right) models. In left plot, blue curve is obtained with resistivity $\rho = 200\,\mu\Omega\,cm$ and red one with $\rho = 400\,\mu\Omega\,cm$ [23].*

Variable-gap current follows Simmons equation (eq. 1.13), as already discussed in section 1.1.1.2, and the associated resistance is R_{Tu}. It can be evaluated, in the approximation of complete applied voltage (V_{app}) drop on the gap, as in eq. 1.41.

$$R_{Tu} = \frac{V_{app}}{I_{Tu}} \tag{1.41}$$

More realistically, total resistance must be evaluated as a series connection of variable diameter filament resistance R_f and R_{Tu}. Considering a filament with constant circular area of diameter d, R_f can be evaluated following equation 1.42, where L is filament length and ρ its resistivity. The latter assumes values higher respect to the one of bulk material, since monodimensional filament nature causes significant carrier scattering at its surface [23]. Corrected resistivity can be evaluated through equation 1.43, by exploiting Fuchs–Sondheimer approximation [42]. Here, λ is the electron mean free path, while p is the specularity factor which describes electron probability of being elastically scattered at the surface.

$$R_f = \rho \frac{4L}{\pi d^2} \tag{1.42}$$

$$\rho = \rho_{bulk} \left(1 + \frac{3\lambda}{4d}(1-p) \right) \tag{1.43}$$

When the filament is still not connecting the electrodes, total resistance can be approximated as R_{Tu}, while after connection, it is null and only R_f remains.
During transition between gap-dominating and diameter-dominating states, filament reaches the electrode initially with a single atom. Successively, filament grows a discrete number of atoms at a time. In this condition, *quantum point contact* is formed and electrons are subjected to 1D conduction. [43] Due to energy quantization, conductance results quantized as a multiple of the quantum G_0 (eq. 1.44), increasing for each atom becoming part of the filament. This phenomenon can be clearly seen in figure 1.18, where R_{ON} is the total measured resistance.

$$G_0 = \frac{2e^2}{h} = 7.748 \cdot 10^{-5} S \tag{1.44}$$

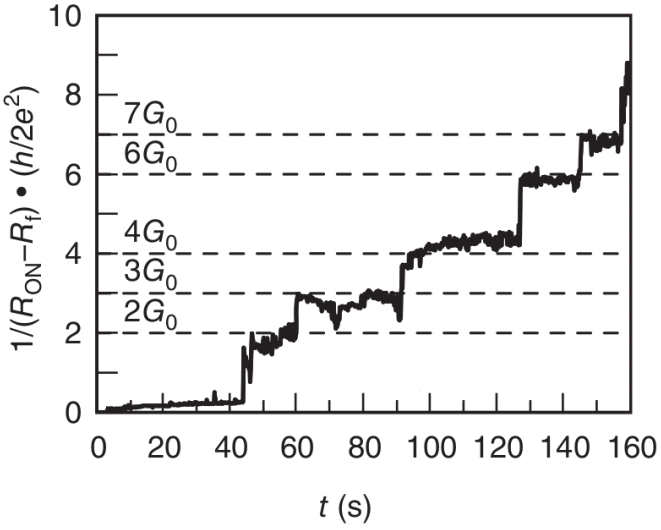

Figure 1.18: *Device conductance during set operation where quantized state can be clearly distinguished. Adapted from [43].*

1.2.2 Valence change memories

Valence change memories are devices typically structured in a MIM fashion, where metal electrodes can be composed by same or different materials and insulator layer is an oxide. Oxygen atoms drifts under the application of an electric field and a sub-stoichiometric filament is formed, leading to high conductivity. Reversing voltage, oxygen vacancies redistribute, breaking so the filament.

1.2.2.1 Electroforming

As discussed in section 1.2.1.2 for ECM devices, also VCM cells requires an initial electroforming step. Its role is to induce a strong asymmetry inside the cell, as evidenced by forming polarity dependent switching reported by Jeong *et al.* in ref. [45]. Figure 1.19 shows on top the forming process and, on bottom, successive switching (which will be explained in details in section 1.2.2.2). Under the application of significative voltage, pristine cell oxygen ions drifts towards the anode (red dots). Double positively charged vacancies form a virtual cathode, which approach the anode. Once contact is established, LRS is obtained. Successive stable switching is reached by resetting the cell producing a gap (also called *disc*) and by shorting it again.
Oxygen ions, after reaching anode, can react with it and form a metal oxide [46], can release electrons and form O_2 bubbles [46] or can be chemisorbed by electrode at grain boundaries (in case of noble metals) [47].

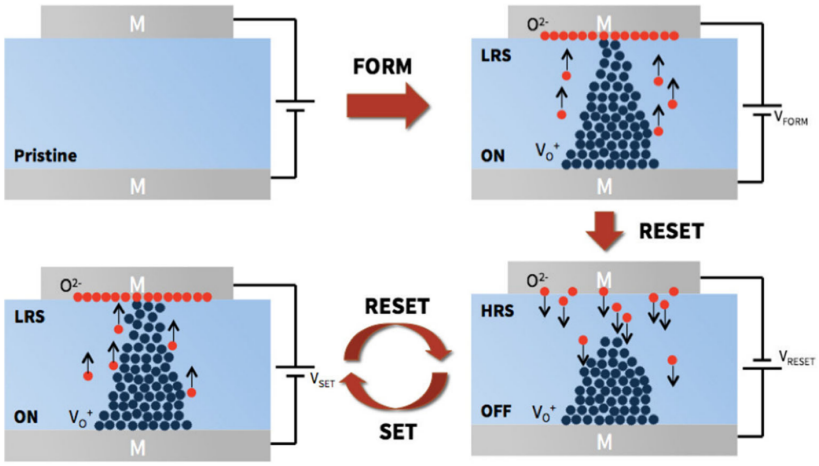

Figure 1.19: *VCM cell forming process (top) and successive switching (bottom) [36].*

1.2.2.2 Working principle

Figure 1.20 shows a typical I-V curve for a VCM device together with illustrations of physical mechanism in different operation steps, which are detailed below [40]. It must be noticed that a cell with negative set and positive reset voltages is reported. As stated in previous section, switching polarity depends on forming step. As a remark, oxygen vacancies behavior is typically studied when discussing VCM cells operation.

A) In OFF state, filament and anode are separated by the gap produced during electroforming. Cell lies in HRS.

B) Increasing voltage until V_{set}, oxygen vacancies migrates towards anode, filling the gap and leading to LRS.

C) Cell lies in ON state and voltage is reduced until negative values.

D) After V_{reset} is reached, $V_{\ddot{o}}$ migrates again towards the filament. Gap is so reformed and device switch to HRS.

1.2.2.3 Conductivity analysis

Models exposed in section 1.2.1.4 are in general valid for every filamentary switching device and so also for VCM ones. Filament resistivity must however be evaluated in a different way, due to its dissimilar nature. According to ref. [48], oxide conductivity (σ)

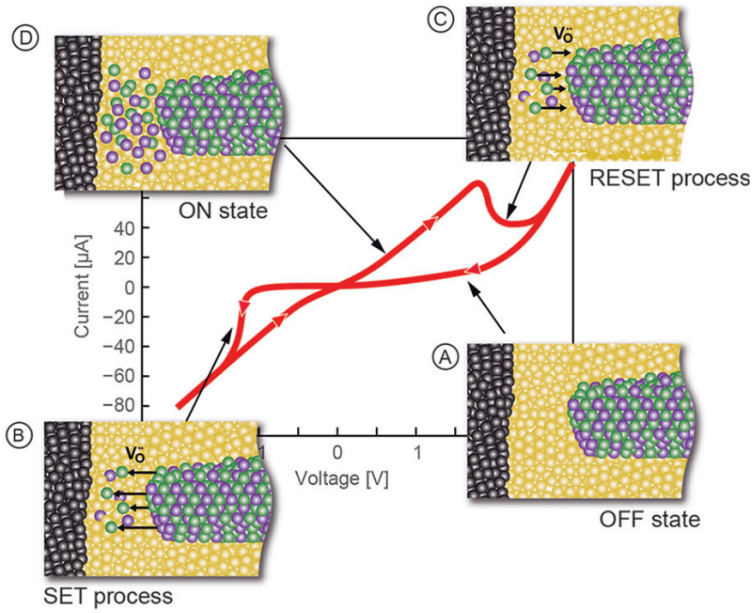

Figure 1.20: *Working principle of VCM cells [40].*

can be evaluated as in eq. 1.45, where i indicates the specific charge carriers contributing to conduction, c their concentration and μ their mobility.

$$\sigma = \sum_i |z_i| e c_i \mu_i \tag{1.45}$$

Considering as only carriers oxygen vacancies double charges, it is obtained $|z| = 2$ and $c = c_{V_{\ddot{o}}}$. Resulting conductivity is shown in equation 1.46, where direct dependence on vacancies concentration justifies filament low resistivity ($\rho = \sigma^{-1}$).

$$\sigma = 2 e c_{V_{\ddot{o}}} \mu \tag{1.46}$$

1.2.2.4 Switching kinetics

Set time relation with pulse voltage is reported in figure 1.21. Several cells data coming from literature are shown, namely TiN/HfO_x/TiN [49][50], TiN/Ti/HfO_x/TiN [51], TiN/HfO_x-AlO_x/Pt [52],Ti/HfO_2/Pt [53], Pt/TiO_x/Pt [54], Ta/TaO_x/Pt [55] and Ti/$SrTiO_3$/Pt [56].

It can be observed that kinetics are characterized by a single slope and so by a single rate limiting process, despite few cases in which a second slope arises. As reported by Menzel *et al.*, ion migration is considered as the prevalent mechanism. [11] According to

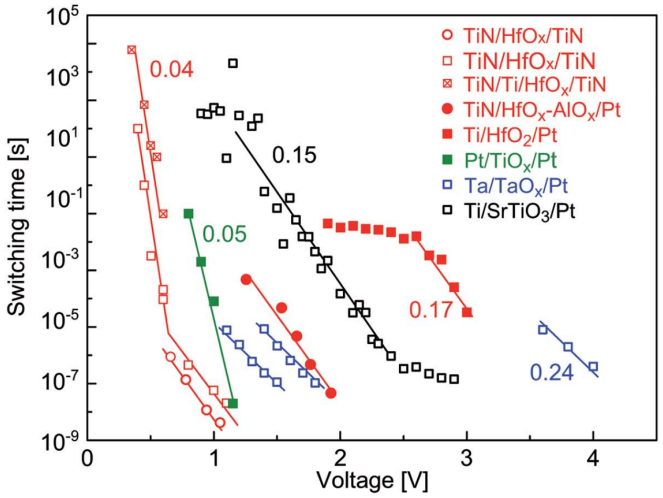

Figure 1.21: *VCM set time characteristics as a function of applied voltage for different cells. Adapted from [11]. Data, following legend order, are reported in ref. [49][50][51][52][53][54][55][56].*

their approximation, set time is evaluated as the time needed for ions to travel across disk length l_{disc} at constant hopping velocity, as expressed in equation 1.47.

$$t_{set} = \frac{l_{disc}}{v_{hop}} \tag{1.47}$$

In high field approximation, Mott-Gurney law (eq. 1.33) reduces to equation 1.48, where V_{disc} is the voltage fraction dropping on the disc. Set time is so evaluated in equation 1.49, where exponential dependence on applied voltage becomes explicit.

$$v_{hop} \approx afe^{-\frac{\Delta W_{i,0}}{k_B T}} e^{\frac{aze}{2k_B T}\frac{V_{disc}}{l_{disc}}} \tag{1.48}$$

$$t_{set} \approx \frac{l_{disc}}{af} e^{\frac{\Delta W_{i,0} - \frac{1}{2}aze\frac{V_{disc}}{l_{disc}}}{k_B T}} \tag{1.49}$$

In order to describe completely switching kinetics, it is necessary to consider hopping velocity dependence on temperature. The exponential relationship has origin in hopping thermal activation, i.e. thermal energy contribution to barrier overcoming. As described in equation 1.50, local rise of initial temperature T_0 is produced by dissipation of electrical power P_{el} on the filament, according to its thermal resistance R_{th}. Being P_{el} the product of applied voltage and current flowing through the cell (I), set time exponential power dependence is reported in equation 1.51. [11]

$$T = T_0 + R_{th} \cdot P_{el} = T_0 + R_{th} \cdot V_{app} \cdot I \tag{1.50}$$

$$t_{set} \approx \frac{l_{disc}}{af} e^{\frac{\Delta W_{i,0} - \frac{1}{2} a z e \frac{V_{disc}}{l_{disc}}}{k_B (T_0 + R_{th} \cdot V_{app} \cdot I)}} \tag{1.51}$$

According to Menzel *et al.*, current flowing through the filament can have different behaviors: ohmic (eq. 1.52) or nonlinear and temperature dependent, in a diode-like fashion (eq. 1.53). Figure 1.22 shows resulting switching time characteristics without considering Joule heating and by using both thermal model described above. Temperature role has clearly strong impact on kinetics, especially in diode-like current model at high voltages. [11].

$$I = \frac{V_{app}}{R_{HRS}} \tag{1.52}$$

$$I = I_0 \left(e^{e \frac{V_{app}}{k_B T}} - 1 \right) \tag{1.53}$$

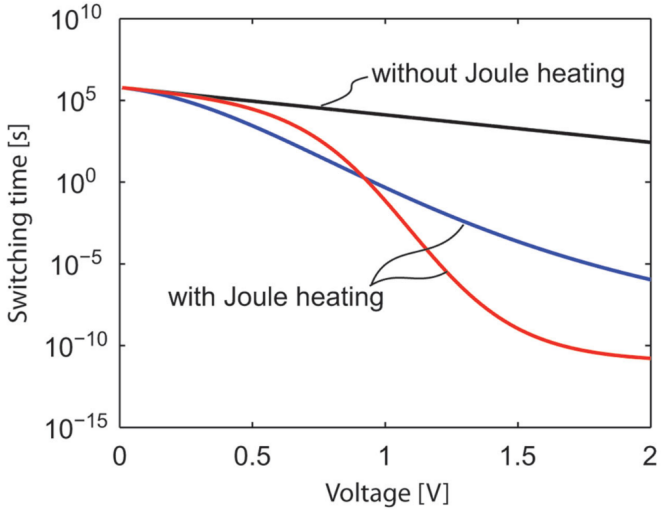

Figure 1.22: *VCM set time evaluation. Black curve is obtained without considering Joule heating. Blue and red ones consider heating effect, respectively with constant and diode-like current models [11].*

Power dependence evidence in VCM cells is experimentally observed by Nishi *et al.* in ref. [56]. Figure 1.23(a) depicts set time results for two different TaO_x based devices as a function of applied voltage, while figure 1.23(b) as a function electrical power. Since cells

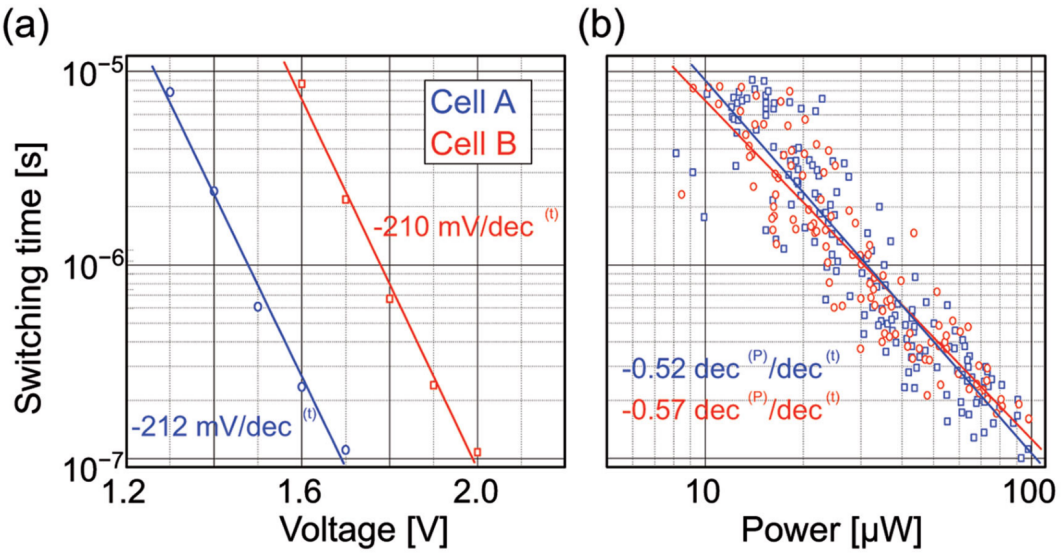

Figure 1.23: *Set time function of voltage applied (a) and power flowing (b) for two tantalum oxide based VCM cells. Reproduced from [11]. Data are provided in [56].*

data difference disappear when P_{el} is considered, it can be deduced that Joule eating is the dominant parameter driving device kinetics.

Chapter 2

Experimental setup

Setup description used during the research activity is fundamental in order to permit experimental reproducibility and a correct results interpretation. In this chapter, the whole experimental procedure, from sample preparation to electrical characterization, will be outlined. In the first section, a discussion on general working principles of production techniques employed will be performed. The latter comprehend radiofrequency magnetron sputtering for material depositions, x-rays reflectometry for layer thickness and sputter rate evaluation and photolithography for pattern transferring. In the second section, principles of electrical characterizations will be explained, in particular of I-V sweeping for quasi-static properties determination, cyclic voltammetry for redox analysis and pulse measurements for ion kinetics study. Finally, specific processes and measurements parameters used for this work will be provided.

2.1 Sample production techniques

In this section, samples fabrication techniques are outlined in their physical basis together with a detailed description of the equipment used in this work. The knowledge of this details is fundamental to correctly understand process impact onto measurements results and device performances.

2.1.1 Radiofrequency magnetron sputtering

Sputtering process belongs to the physical vapor deposition (PVD) techniques and is suitable for layer deposition in the nanometric scale. As it can be seen in figure 2.1, the substrate is placed on a sample holder, while, in front of it, the material source for the ions to be deposited (*target*) is mounted on a support called *sputter gun* or *sputter head*.

An inert gas plasma (such as argon) is excited by external electrical stimulus and under reduced pressure, ablating the target material and depositing ions onto the substrate.

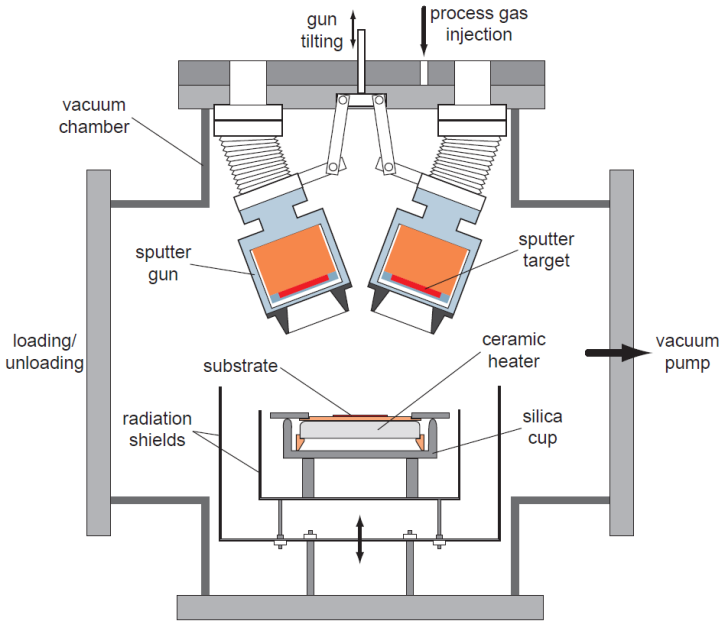

Figure 2.1: *Construction example of a sputtering chamber [57].*

The process can be classified according to the nature of the electrical stimulus:

- *DC sputtering*: the voltage is constant, the target acts as a cathode while the substrate as an anode. Plasma ions are attracted towards the cathode and extract atoms from the target by impact, which then condense onto the substrate forming a film. The main problem of this configuration is the impossibility of depositing insulating materials. This is due to substrate and target charging, which repels incoming ions reducing the impinging rate. [58]

- *RF sputtering*: the voltage is alternating in the radio frequency (RF) range, typically at 13.56 MHz. Target acts as the exciting electrode, while substrate and chamber walls act as the reference one. Target lower area permits itself to attract ions (as explained below), which bombardment extracts the atoms. The latter, also in this case, condense onto the substrate forming the desired layer. The main advantage of this configuration is the possibility of depositing insulating layers. An increase in complexity is however required, due to necessity of inserting a matching network between the transmission line coming from the generator and the chamber, in order to prevent power reflection. Compounds deposition can also be obtained by means

of reactive sputtering by injecting in the chamber reactive gases. Oxide, for example, can be deposited by injecting O_2. Plasma dissociates molecular oxygen into radicals, which react with sputtered atoms, depositing the oxide. [59]

In the whole subsequent text the analysis will focus on RF sputtering only, since it is the configuration exploited in this work.
As said before, the asymmetry of the electrodes areas in necessary for the correct behavior of the system. The current flowing through the target (I_t) is balanced by the ones flowing through the walls (I_w) and the substrate (I_s) (eq. 2.1). As shown by equations 2.2 - 2.3, target current density (j_t) results higher than substrate (j_s) and walls (j_w) ones, due to target area (A_t) lower then substrate (A_s) and walls (A_w) ones. This variation causes a prevalent effective voltage drop adjacent to the cathode, as can be observed in figure 2.2. This effect permits both the preservation of the deposited material from being damaged by the plasma, but also the minimization of chamber walls sputtering. In this way, the unwanted contamination of the produced layer from walls material atoms (such as iron from stainless steel) can be strongly limited. [60]

$$I_t = I_s + I_w \tag{2.1}$$

$$j_t \cdot A_t = j_s \cdot A_s + j_w \cdot A_w \tag{2.2}$$

$$j_t = j_s \cdot \frac{A_s}{A_t} + j_w \cdot \frac{A_w}{A_t} \tag{2.3}$$

It is also possible to improve ionization and sputtering efficiency by performing the so called *magnetron sputtering*. In this configuration a magnetic field is applied near the target, forcing the electron into an elicoidal path. This ensures them a longer path and so an higher probability of scattering with an atom, increasing the ionization rate. [61]

Figure 2.3 shows the custom made RF magnetron sputtering system, called *CT1000*, used in this work. It is composed by six vacuum chambers and a loadlock, with a robotic arm for sample movement. Each chamber hosts three sputter heads, tilted by 45° with respect to the sample, which is made rotating during the whole deposition, ensuring a greater uniformity. Sputter heads are provided by *AJA International* in the model *ST20 - Stiletto Series Magnetron*, designed for 2" circular targets. Tantalum oxide is deposited by sputtering of a 3N5 tantalum target, low purity copper by a 4N target, while high purity copper by a 6N target provided by EVOCHEM.

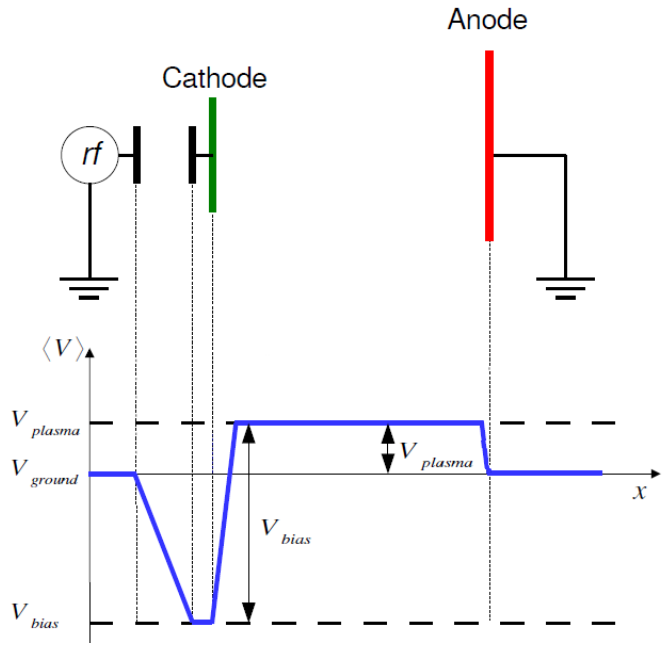

Figure 2.2: *Electrodes schematic and relative effective voltage distribution. Adapted from [62].*

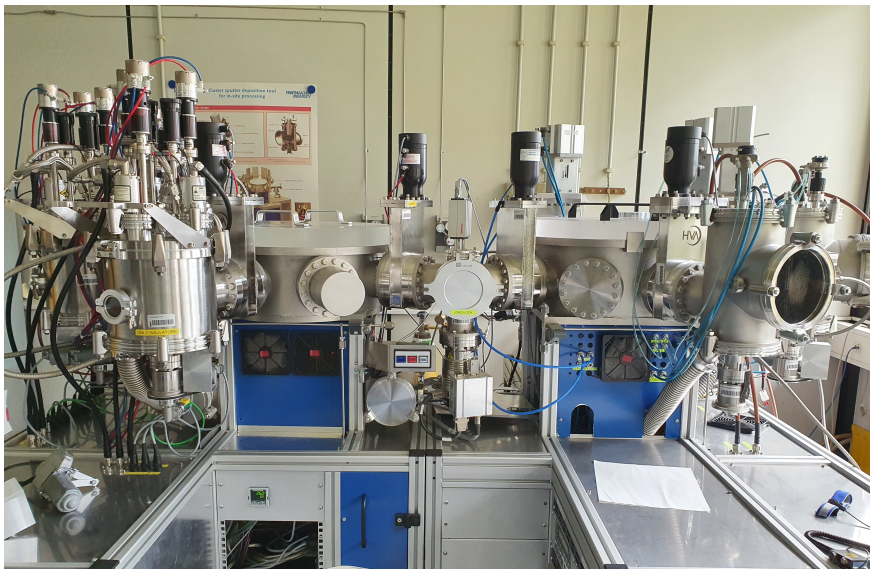

Figure 2.3: *Picture of the CT1000.*

2.1.2 X-rays reflectometry

X-rays can be used for characterizing deposited layer thickness, roughness and density with the X-rays reflectometry (XRR) technique. This properties are extracted by analysing the total reflection critical angle (θ_C) and the interference pattern between the wave portion

reflected at the top surface and the one reflected at the interface between the layer and the underlying material.
Measurement setup is composed by an X-ray tube source, a tiltable and shiftable sample holder and a detector, as shown in figure 2.4.

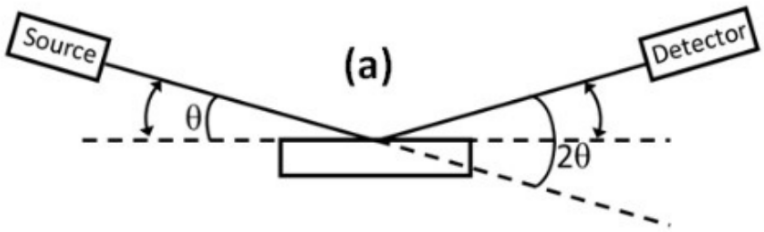

Figure 2.4: *XRR experimental setup schematic [63].*

Measurement starts by irradiating the sample surface with an incidence angle (θ) lower than the total reflection critical one (eq. 2.8). In this condition, the whole incoming wave (except from the evanescent component) is reflected. The incidence angle is then incremented, by tilting the sample holder, to a maximum value (greater than θ_C) dependent on the structure under analysis. The wave is partially reflected and partially refracted, penetrating the layer. Transmitted component propagates towards the next interfaces and is subjected to the same phenomena. Both the interactions are shown in figure 2.5.

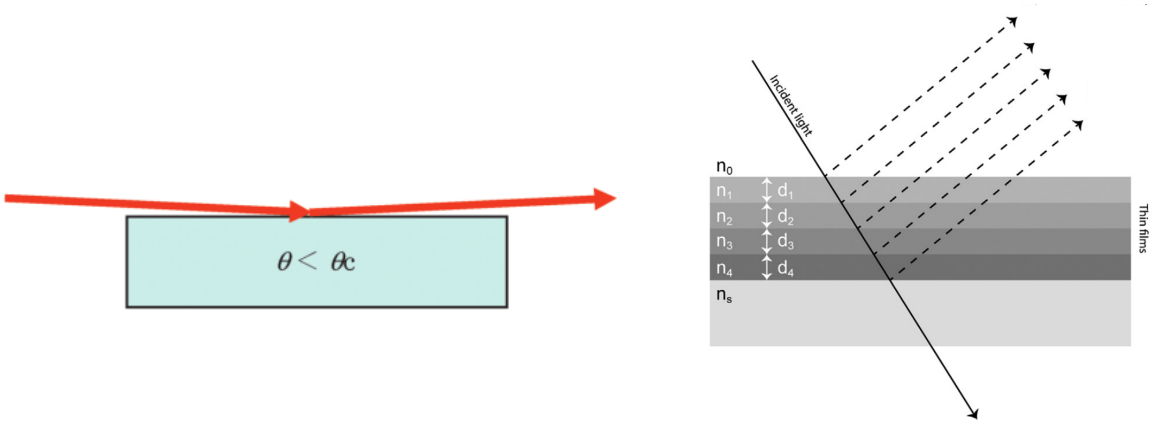

Figure 2.5: *X-rays interaction with surface below (left [64]) and above (right [65]) critical angle.*

The detector records the intensity of reflected components superposition, as a function of incidence angle (the so-called *interferogram*). Interference between these waves produces observable fringes, called Kiessing fringes [66], whose properties are dependent on layers composition and morphology. [64]

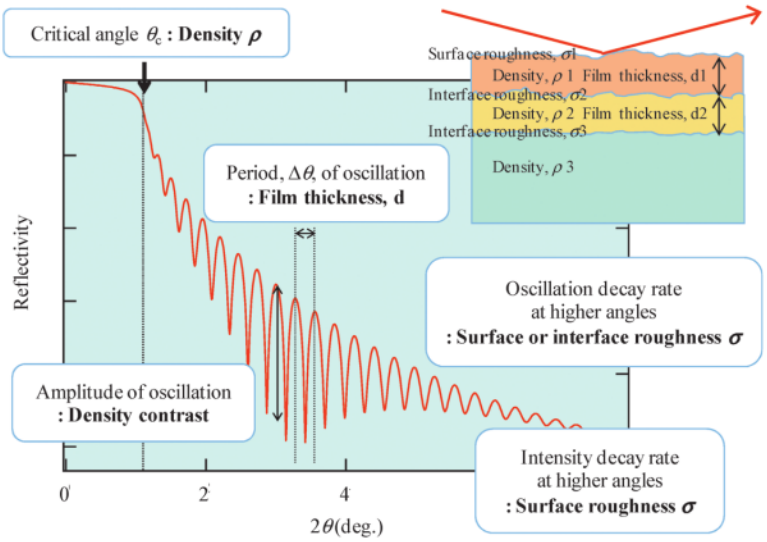

Figure 2.6: *Reflectivity curve general profile. In text-boxes, related properties are provided [64].*

Figure 2.6 shows a general example of reflectivity profile together with a summary of obtainable layers properties. The latter and their relations with interferogram parameters are detailed below, following ref. [64].

- *Layer density*: it influences the refractive index of the material, as shown in equations from 2.4 to 2.6, where r_e is the electron radius, N_0 the Avogadro number, λ the X-ray wavelength, ρ the mass density, z the atomic number, M the atomic weight, x the molar ratio, f' and f'' the atomic scattering factors. Subscript i identifies the specific atom which acts as photon scattering center.

$$n = 1 - \delta - i\beta \tag{2.4}$$

$$\delta = \frac{r_e \lambda^2}{2\pi} N_0 \rho \frac{\sum_i x_i (Z_i + f_i')}{\sum_i x_i M_i} \tag{2.5}$$

$$\beta = \frac{r_e \lambda^2}{2\pi} N_0 \rho \frac{\sum_i x_i (Z_i - f_i'')}{\sum_i x_i M_i} \tag{2.6}$$

  Refractive index enters directly in critical angle definition through Snell's law. It is reported in equations 2.7 and 2.8, where i and r subscripts indicate respectively incident and refracted light. For this reason, material density can be estimated

by analyzing θ_C value, as can be seen in figure 2.7. Moreover, oscillations amplitude is observed to be proportional to density difference between the layer and the subsequent one.

$$n_i \sin(\theta_i) = n_r \sin(\theta_r) \tag{2.7}$$

$$\theta_C = \arcsin\left(\frac{n_r}{n_i}\right) \tag{2.8}$$

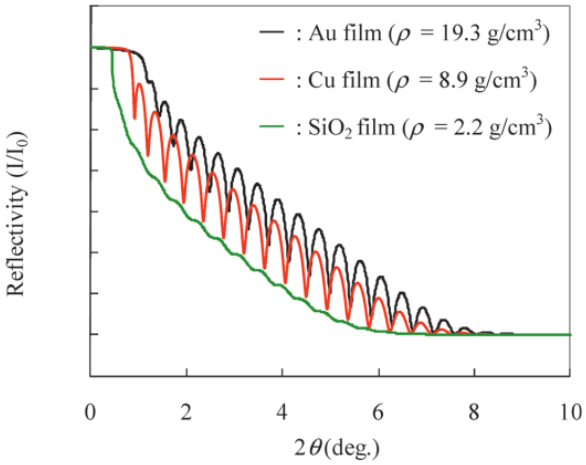

Figure 2.7: *XRR curve for materials with different densities, on common Si substrate [64].*

- *Layer thickness*: it can be obtained by studying the oscillation period. Indeed, intensity follows the behavior reported in equation 2.9. Figure 2.8 shows an example of reflectivity pattern for two gold films of different thickness. It makes clear that a thicker layer implies a shorter period.

$$I \propto \cos\left(\frac{4\pi d}{\sqrt{\sin^2\theta - 2n}}\right) \tag{2.9}$$

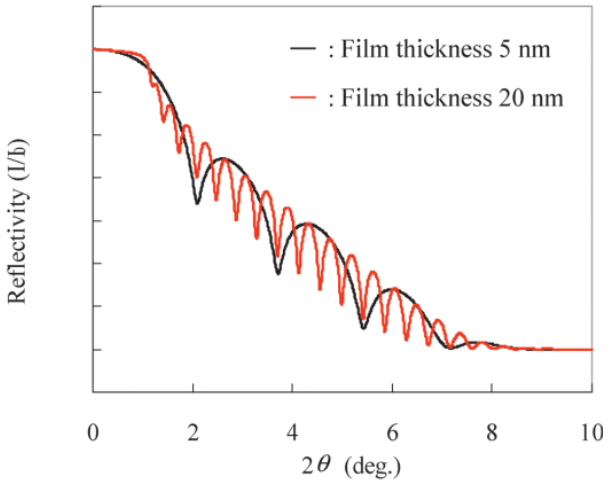

Figure 2.8: *XRR curve for Au layers of different thickness [64].*

This is the only parameter that can be easily obtained by means of a Fourier transformation of the reflectivity curve. It will present a peak at the exact thickness value.

- *Interface raughness*: its increasing will cause a stronger damping in oscillation amplitude (for layer-substrate roughness) and curve decay (for air-layer roughness) (figure 2.9). It is due to the local variability of incidence angle due to non-perfect surface.

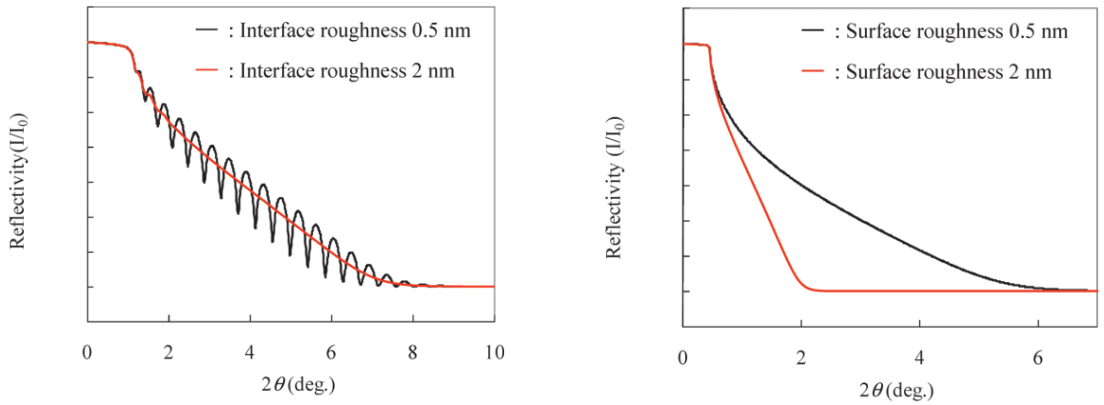

Figure 2.9: *Reflectivity curve for Au layers of different bottom (left) and top (right) surface roughness.[64]*

In this work, an *X'Pert PRO* equipment by *PANalytical*, with a Cu Kα x-rays source,

is used. Acquired data are post-processed by using *X'Pert Reflectivity* software, provided by the instrument producer.

2.1.3 Photolithographic patterning

Photolithography is a technique which permits to transfer nanometric features from a master (*mask*) to a photoactive polymeric film (*photoresist*) in a one-shot process. This protection layer prevents the covered areas from being altered by the subsequent process, permitting high spatial resolution in each device fabrication step. Photolithography procedure flow is depicted in figure 2.10 and is detailed below [67].

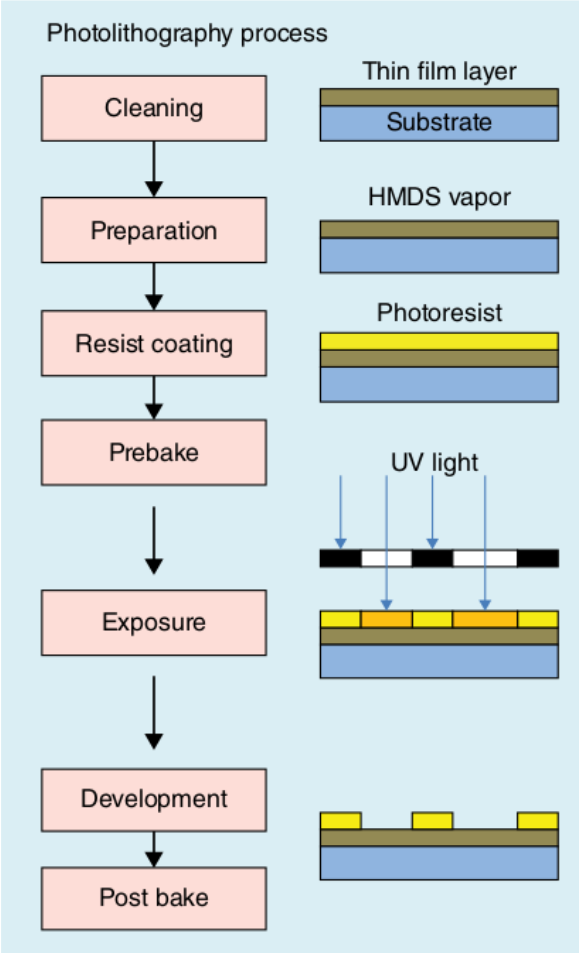

Figure 2.10: *Photolithography process flow. Adapted from [68].*

1. *Cleaning:* sample surface to be manipulated must be ideally perfectly cleaned in order to have the best resist adhesion possible. For this reason the whole process

takes place inside a clean room and, sometimes, in specific sections of higher class. Surface is typically cleaned by immersion and sonication with acetone, isopropanol and deionized water, in succession. Then, it is dried by an inert gas flow, such as nitrogen. At the end of this step, particulate or charged species has been removed.

2. *Preparation with HDMS primer deposition:* HDMS is deposited from vapor phase and has the role to improve successive photoresist coating. This step is optional, depending on surface material and application.

3. *Photoresist spin-coating:* sample is attached to a vacuum chuck in the spin coater. Resist is distributed on the sample surface and excess is removed through rotation by means of centrifugal force, resulting in a thin layer in the micrometer range.

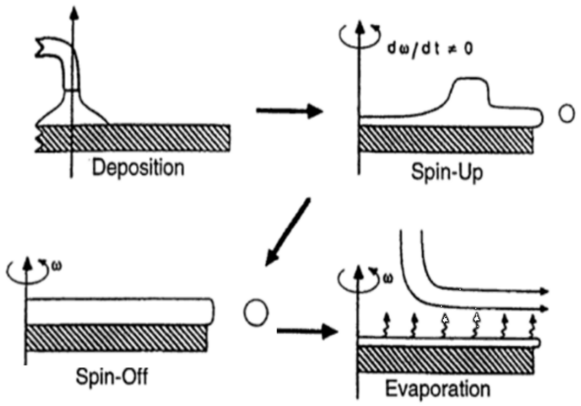

Figure 2.11: *Photoresist spreading during spin-coating [69].*

4. *Soft bake (or prebake):* coated film undergoes thermal treatment on a hot plate at constant temperature ranging from 90 °C to 115 °C. This causes residual solvent evaporation and adhesion improvement.

5. *Exposure:* photoresist is illuminated by UV light through the mask. Exposed regions becomes soluble by polymeric chains breaking, in case of *positive* resist, or insoluble by cross-linking, for *negative* resist. The possible configurations for this step are depicted in figure 2.12 and are differentiated in the mask-resist interface. In *contact* mode, mask is in direct contact with the resist. In *proximity* mode, a gap is present in between, which reduces the possibility of resist contamination. *Projection* mode insert a lens in the gap, permitting a dimensional shrinking of projected features, increasing spatial resolution. In this configuration, several adjacent mask pattern can be transferred onto the sample by raster scanning. It is the one employed for

industrial application, but, despite its advantages, requires a significant increase in complexity and costs. [70]

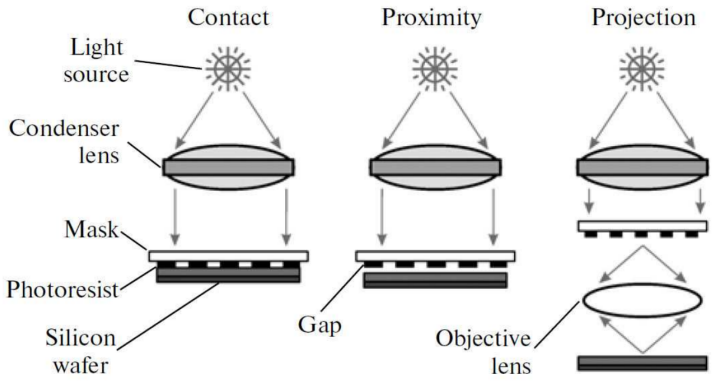

Figure 2.12: *Exposure in contact, proximity and projection configurations [70].*

6. *Post-exposure bake:* in this optional step, exposed sample is heated in a temperature range from 110°C to 125°C. In this way, photogenerated chemicals are redistributed, improving pattern uniformity. Furthermore, standing waves effect is progressively suppressed, as shown in figure 2.13. This effect implies a periodic fluctuation of exposed region borders, due to impinging light interference with substrate reflected component. A thermal treatment forces chemical redistribution, smoothing affected edges.

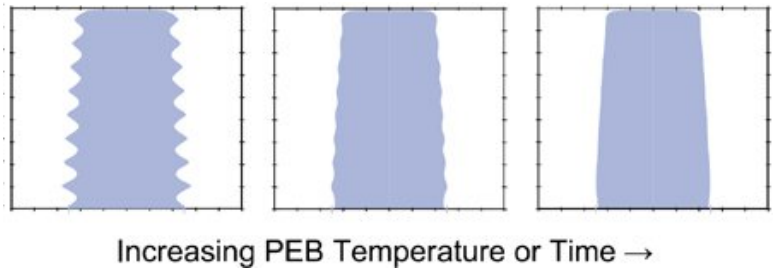

Figure 2.13: *Standing waves progressive suppression function of post-exposure bake time or temperature [71].*

7. *Development:* sample is immersed in an appropriate solvent, dissolving soluble regions of the photoresist. At the end of this step, an exact replica of mask pattern is obtained if the resist is positive, otherwise complementary pattern is obtained, as sketched in figure 2.14.

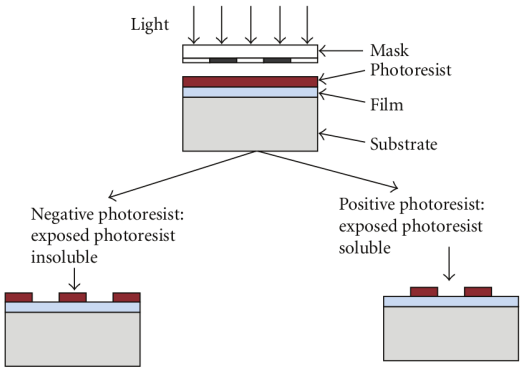

Figure 2.14: *Negative (left) and positive (right) photoresist behavior. Adapted from [72].*

8. *Hard bake:* a final bake at temperature between 110 °C and 125 °C can be optionally performed in order to improve resist adhesion and hardness.

At the end of photolithography, a desired portion of the surface is exposed to the next process, while the complementary is protected. Several kinds of modifications can be performed such as compositional (oxidation, diffusion, implantation, etc.) or structural (deposition, etching, etc.).
Focusing on structural alterations, a patterned film can be obtained by etching or lift-off, as illustrated in figure 2.15. In the first case, film is deposited, lithography is performed on top of it and the etchant is put in contact with the sample, removing the uncovered parts. Lift-off, instead, is a process in which material is deposited on the resist, previously patterned over the substrate. Subsequently, resist is removed by means of a solvent, together with the material deposited on top of it. In this way, a film patterned as the uncovered surface is obtained. This technique has the advantages of not using any acid, relaxing health safety cautions and masking layers choice. [73]
However, some additional constrains must be taken into account [74]:

- in order to be successfully removed, resist must have thickness typically greater than $2\,\mu m$;
- for the same reason, deposited layer thickness must be lower than resist one;
- in order not to remove unwanted film portions, a strong discontinuity in the film at the resist edges should be present. This can be obtained by using image reversal resist technique, producing undercut edges, as can be seen in figure 2.16.

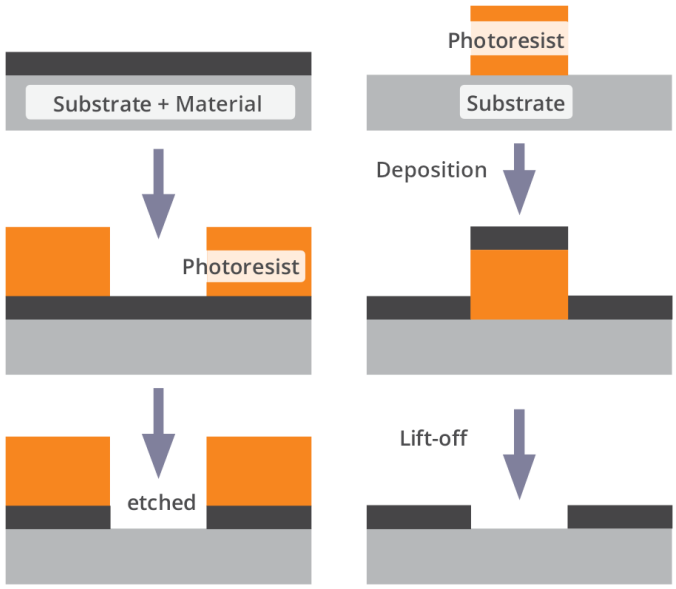

Figure 2.15: *Comparison between standard etching (left) and lift-off (right) patterning. Adapted from [75].*

Figure 2.16: *Deposited film features onto undercut (left) and standard (right) profile [73].*

This result can be obtained with the process depicted in figure 2.17. The flow is the same of standard lithography until exposure. Then, an image reversal bake is performed, leading to illuminated part insolubility. Afterwards, sample is flood exposed without any mask and developed. The final result is a resist pattern complementary to the mask one. It must be noticed that the effect is the same obtained with an opposite polarity resist, with the advantage of negative edge slope.

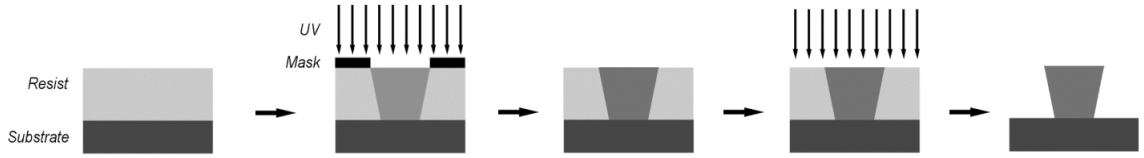

Figure 2.17: *Reversal bake process. Adapted from [73].*

In this work, contact mode exposure and lift-off procedure are used, by employing an ad hoc designed photoresist and a mask produced by *Peter Grünberg Institut* located in Jülich. The whole process takes place in a class 100 cleanroom with a temperature range of $23\,^{\circ}\mathrm{C} \pm 1\,^{\circ}\mathrm{C}$ and a relative humidity range of $45\,\% \pm 5\,\%$. In table 2.1 is reported a list of all the chemical product used while, in table 2.2, a list of the main equipment employed.

Chemicals		
Product	**Name**	**Producer**
Photoresist	*AZ 5214 E*	*Microchemicals®*
Developer	*AZ 826 MIF*	*Microchemicals®*
Acetone	-	*Microchemicals®*
Isopropanol	-	*Technic®*

Table 2.1: *List of used chemical products.*

Equipment		
Product	**Name**	**Producer**
Ultrasonic bath	*Transsonic Digital S*	*Elma®*
Spin coater	*Delta 10*	*Süss Microtec®*
Mask aligner	*MA 6*	*Süss Microtec®*

Table 2.2: *List of main equipment employed.*

2.2 Electrical characterization

In this section, a description of measuring techniques principles and specific configurations used in this work is reported. Since results interpretation is directly related to data acquisition methodology, this explanation is necessary to ensure correct reproducibility.

2.2.1 I-V sweeping

I-V sweeping measuring technique is utilized for studying memristive devices quasi-static behavior. As shown in figure 2.18, a first positive triangular voltage stimulus and then a negative one are applied to the device top electrode (TE), recording current flowing. The bottom electrode (BE) is grounded and acts as voltage reference. Initially, cell lies in high resistance state. During the first positive ramp, current slightly grows until set

voltage, where switching takes place. Resistance suddenly decreases and low resistance state is reached. Voltage is then reduced and, at reset voltage, switching back to HRS is triggered.
Despite these working condition is different from real application, where the stress is in the form of constant pulses, useful information can be acquired. For example, an estimation of device variability and reliability, together with obtainable resistance values can be made.

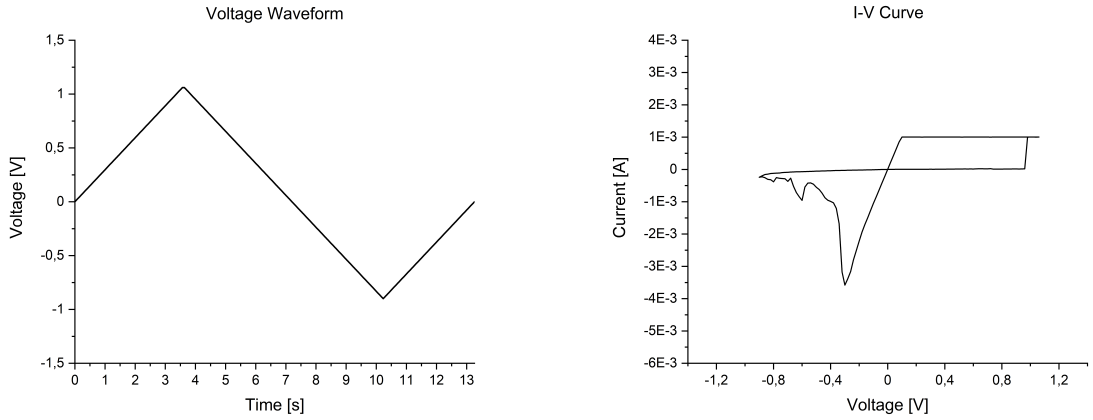

Figure 2.18: *Example of voltage applied stimulus (left) and associated I-V curve (right).*

Sweeping and measuring can be performed both with separate instruments or directly through a source meter. Additionally, two different configurations can be exploited, namely two-wires and four-wires. Circuital schematics are reported in figure 2.19. In two-wires setup, voltage source and amperometer are connected to sample electrodes through the same interconnections. Voltage applied to the device is assumed to be equal to the one delivered by generator, causing an overestimation due to voltage drops on interconnections parasitic resistances. Four-wires design can overcome this issue, since a voltmeter is added in parallel to the cell, directly reading actual ReRAM voltage drop.

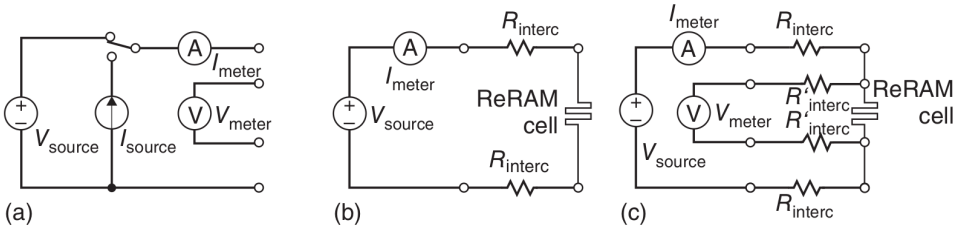

Figure 2.19: *Source meter (a), two-wires setup (b) and four-wires setup (c) circuital schematics [23].*

As can be seen in the I-V curve in figure 2.18, shortly after set event, a current compliance is forced. This limitation is necessary since prevents a burning through caused by an excessive energy flow in the cell. Indeed, it would lead to an irreversible low resistance state due to oxide breakdown. CC provide also the possibility to program multiple resistances levels in a single device, since an increasing in current leads to a reduction of the obtained LRS. Figure 2.20 shows three different solutions that can be implemented for current limitations, which are detailed below.

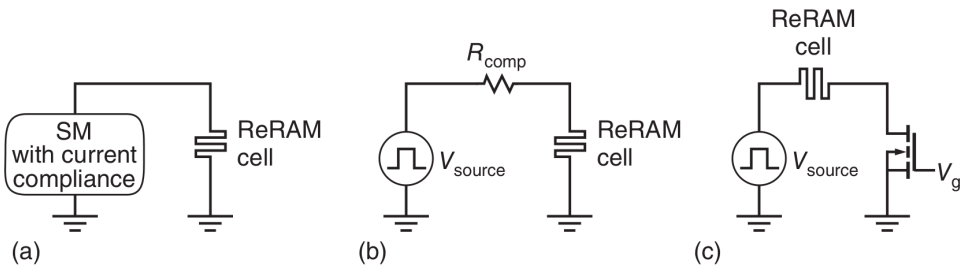

Figure 2.20: *Current compliance setup by source meter embedded circuit (a), limiting resistor (b) and transistor (c). Adapted from [23].*

- *Source meter* often directly embed a feature which permit to program a compliance value. In particular, when current measured overcomes the limit, voltage source mode is replaced by constant current source mode. Despite the advantage of easy boundary choice, instrument response time can represent a problem. In specialized equipments, its value is approximately 60 ns [23]. During this period, a significant current overshoot can be present before system limitation is applied, as depicted in figure 2.21. Depending on the excess magnitude, it could cause device unexpected behavior and, in the worst case, breaking.

- A *limiting resistor (R_{comp})* can be inserted in series with the cell, in order to keep resistance seen from the generator high enough when LRS is reached. In this way, the maximum current that can flow is $I_{max} = V_{source}/R_{comp}$ and response time is overcame. With respect to the previous method, this cause a strong reduction in CC tuning flexibility. An overshoot can however still be present due to setup parasitic capacitance (C_{par}) charging. For this reason, is important to generally minimize C_{par} and to insert resistor the closest possible to the device, if feasible also integrated.

- Alternatively, a *transistor* can be inserted instead of a resistor. Maximum current allowed can be forced by choosing the appropriate saturation current with the rel-

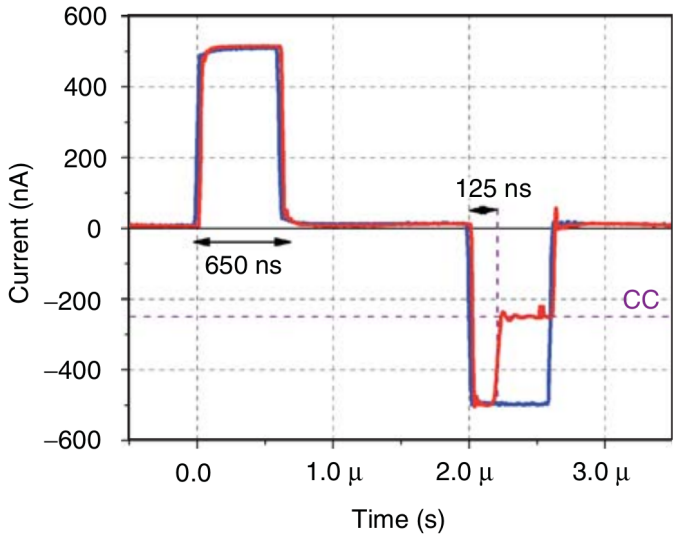

Figure 2.21: *Example of current overshoot due to response delay [23].*

ative gate voltage application (V_g). This permits to easily tune CC by varying V_g, according to equation 2.10, in case of a n-type MOSFET. Here μ_n is the electron mobility, C_{ox} the oxide capacitance, W the channel width, L the channel length, V_{th} the threshold voltage and V_d the drain voltage. Also in this case, same consideration on the role of parasitic capacitance are valid.

$$i_D = \mu_n C_{ox} \frac{W}{L} (V_g - V_{th}) V_d \tag{2.10}$$

As highlighted at the beginning of this section, I-V sweeping is not suitable for device characterization in conditions similar to applicative ones. One important reason is the switching dependence on the *sweep rate (SR)*, which is the voltage variation per unit time ($SR = dV/dt$). In details, as illustrated in figure 2.22, decreasing the sweep rate leads to a reduction in switching voltage magnitude, both during set and reset operations. This can be attributed to a longer exposition to voltage signal, resulting in a longer forming time, even if at lower potential.

In this work, measurements are performed at room temperature and pressure, in a custom made probe station. It's main components are two micro-tips moved by mechanical micromanipulators, a microscope for manual tip - sample connection, and an anti-vibration base. A *Keithley 6430* source meter in used, with embedded current compliance limiter and two-wires configuration. The latter is schematized in figure 2.23 and, as can be observed, voltage signal is delivered to Cu top electrode, while Pt bottom electrode is connected to reference potential.

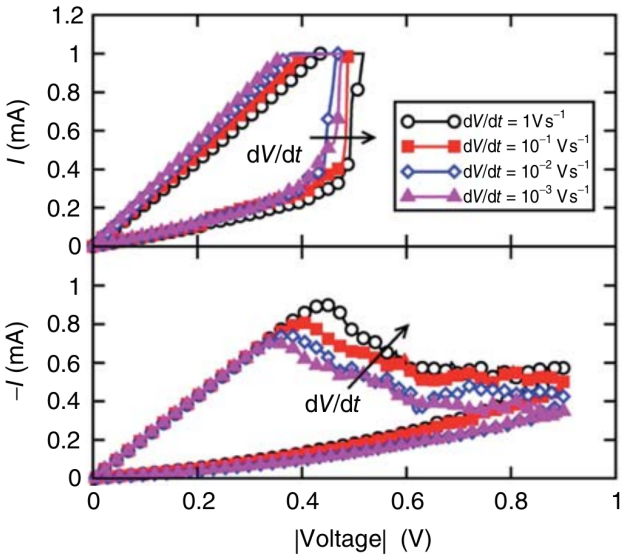

Figure 2.22: *Example of set (top) and reset (bottom) voltage dependence on sweep rate [50].*

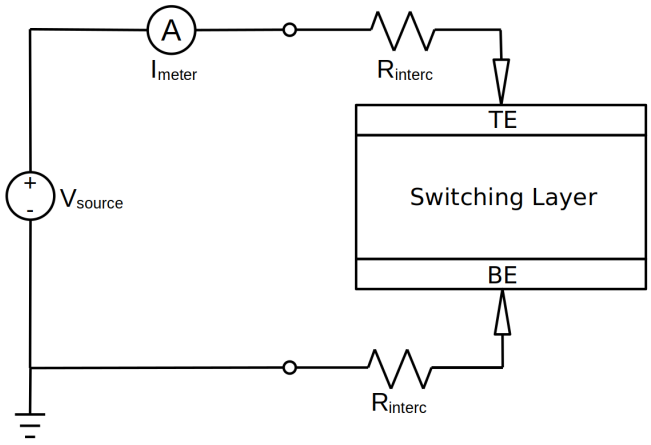

Figure 2.23: *Schematics of this work setup.*

2.2.2 Cyclic voltammetry

Cyclic voltammetry (CV) is an electrical characterization technique suitable for the analysis of electrode reaction kinetics. In particular, oxidation and reduction of interfacial electrode ions can be studied. In order to do so, typically pristine cells are analyzed since they are not formed yet and ohmic conductance is negligible. Typical configuration is the same of two-wires I-V sweeping, tough a central reference electrode should be present in order to correctly quantify half-reactions. Unfortunately, reference is technologically complicated to be implemented in planar devices, as the one under study. For this reason, two-probe setup is used which still permits to obtain qualitative results. [76]

Also in this process, a triangular stimulus is used, with low enough voltage in order not to trigger electroforming. In the meanwhile, current is recorded and a curve similar to the one reported in figure 2.24 is obtained. During the initial increasing of voltage, low electronic current (typically due to leakage) is measured. When the voltage is high enough, the atoms can overcome the potential barrier and oxidize, causing a peak of faradaic current. In the negative voltage side, ions are reduced at the appropriate potential, resulting in a negative peak. It must be noticed that, in both polarities, more than one peak can be observed depending on the number of possible oxidation states. It is also a possibility that an observed single peak results from the superposition of different reactions. [77]

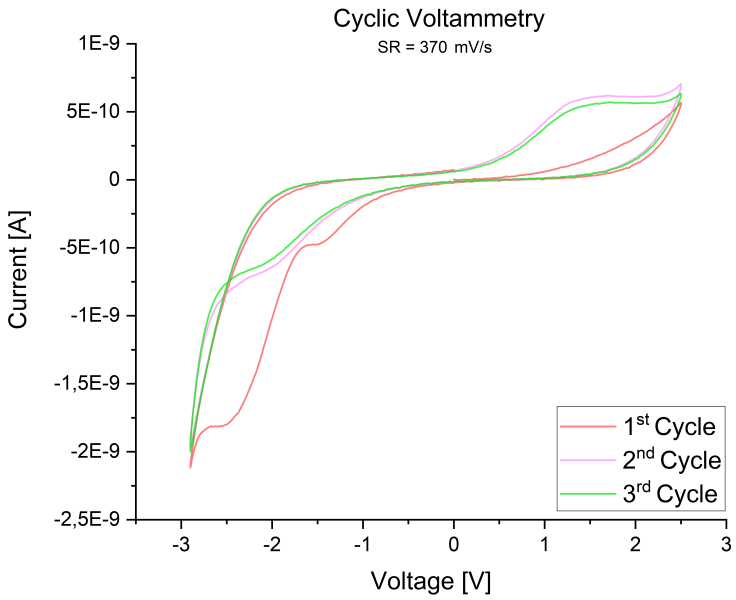

Figure 2.24: *Example of cyclic voltammogram with sweep rate* $SR = 370\,\frac{mV}{s}$.

As stated before, current measured posses a leakage component. However, in many cases, it can be assumed to be negligible. The evaluations presented below are performed considering a pure faradaic current. In this condition, integrating the positive branch in time provides the total number of charges exchanged and so the oxidized ion number. Starting from this value, it is possible to estimate the ion diffusion coefficient (D_{ox}) by exploiting equation 2.11 (Randles–Sevcik equation) [78]. Here j_p is the current density of the reduction peak, z the number of electron transferred during the reduction, c_{ox} the ion concentration in mol/cm^3, α the charge transfer coefficient and ν the sweep rate.

$$j_p = 2.99 \cdot 10^5 \cdot z^{\frac{3}{2}} \cdot c_{ox} \sqrt{\alpha D_{ox} \nu} \tag{2.11}$$

Inserting D_{ox} in equation 2.12 (Nernst-Einstein equation [77]), the ion mobility (μ) can be estimated. Here e is the electron charge, k_B the Boltzmann constant and T the absolute temperature.

$$\mu = \frac{D_{ox} z e}{k_B T} \tag{2.12}$$

As a final remark, CV permits also to study the progressive electrode passivation. Indeed, as shown in figure 2.24, a systematic decrease in current magnitude is observed for successive cycles. In this specific case, it is caused by the oxidation of electrode copper, forming an insulating film of copper oxide.
In this work, the same experimental setup described for I-V sweeping in section 2.2.1 is used.

2.2.3 Pulse measurements

In order to evaluate device behavior in conditions similar to applicative ones and to obtain information about switching kinetics, pulse measurements are used. In a two-wires setup, a series of squared voltage pulses is applied to the sample, while current is evaluated by means of an oscilloscope [79]. Figure 2.25 shows in black a typical voltage waveform applied to ReRAM cell, while in red is reported the recorded device response. The detailed description of the pulse is the following:

- in A, a read voltage (V_{read}) with maximum value of 0.2 V is used to read the initial cell resistance state;
- long pulse B is the actual applied voltage (V_{app}), used to trigger a set event and its value is dependent on the specific measurement;
- in C, a second read pulse checks the effective result of the setting;
- negative D pulse is used to reset the cell to HRS;
- the final cell state is monitored by applying a final read pulse E.

In this configuration, it is possible to evaluate the set time, which is a measure of the delay between voltage application and device switching. From the applicative standpoint it is a key parameter, indicating the maximum frequency at which ReRAM cell can operate. By definition, t_{set} is determined as the time interval elapsing between half maximum of both input voltage and device current, as shown in equation 2.13.

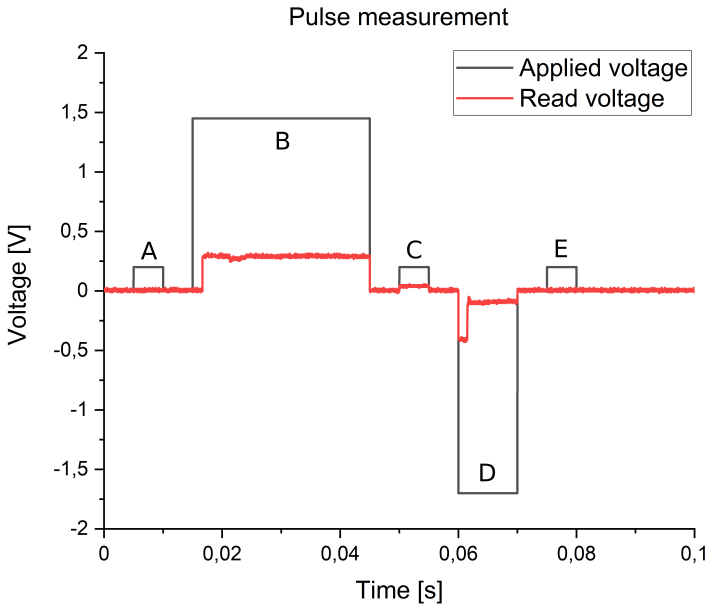

Figure 2.25: *Example of applied waveform (black) and measured device voltage (red).*

$$t_{set} = t\left(\frac{1}{2} \cdot V_{app,max}\right) - t\left(\frac{1}{2} \cdot I_{meas,max}\right) \tag{2.13}$$

Considering that measured current maximum can be influenced by charging effects of parasitic capacitances, it is useful to evaluate t_{set} as the time lapse between half rising time (t_{rise}) of input and output signals. Rising time is defined as the time needed from the signal to grow from 10% to 90% of its maximum, as reported in equations 2.14 - 2.15

$$t_{rise,V} = t\left(90\% V_{app,max}\right) - t\left(10\% V_{app,max}\right) \tag{2.14}$$

$$t_{rise,I} = t\left(90\% I_{meas,max}\right) - t\left(10\% I_{meas,max}\right) \tag{2.15}$$

This measurement technique can be also exploited to study ionic kinetics of the device and especially rate limiting processes, as described in section 1.2.1.3. As additional remark, the final flat characteristics in figure 1.16 can be attributed to setup limitation, where t_{set} becomes lower than generator rising time. Sample results then subject to a voltage ramp, in the same fashion of an I-V sweeping measure. [38]

Setup used in this work is schematized in figure 2.26. A *100 MHz Synthesized Arbitrary Waveform Generator* (from *Wavetek, Model 395*) is connected to the sample TE.

A *DPO 7254C Digital phosphor Oscilloscope* (from *Tektronix*) is used to record the signals. Considering its low voltage sensitivity in high frequencies applications, evaluation of the high resistance state is critical. For this reason, ReRAM BE is connected to a *Hewlett-Packard 04192-61001* power splitter. One branch is directly measured (for LRS state) and the other is connected to an *HCA High Speed Current Amplifier* (from *Femto*), with gain A=5 kV/A. Output signals go to three oscilloscope channels: CH1, CH2 and CH3. Each channel embed a 50 Ω resistor (R_{CH1}, R_{CH2}, R_{CH3}), which are necessary to convert currents into voltages, readable from the oscilloscope (V_{CH1}, V_{CH2}, V_{CH3}). V_{CH1} is a copy of the waveform generated by the signal source, CH2 is connected to the non-amplified current flowing through the device, while CH3 is connected to the amplifier and is used for HRS reading.

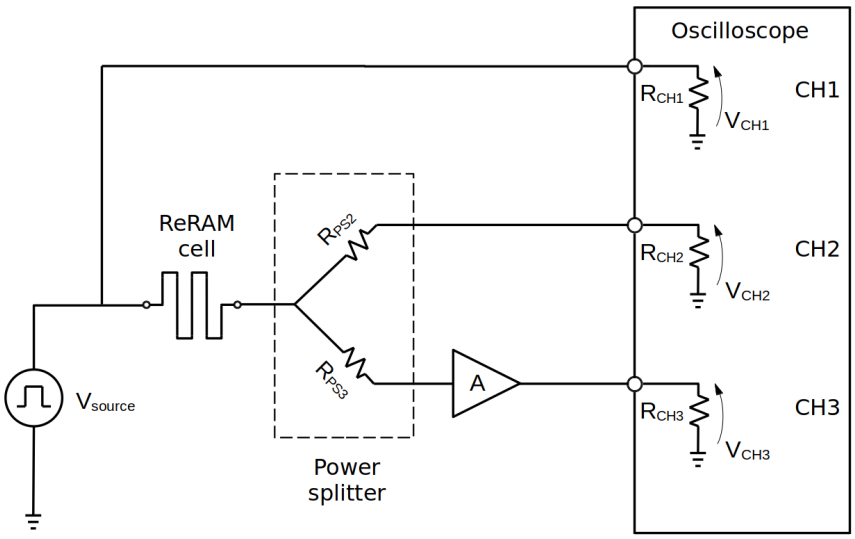

Figure 2.26: *Measurement setup electrical schematic.*

Finally, by applying voltage dividers and Ohm's law, resistances can be evaluated as reported in equations 2.16 - 2.18. Equation 2.17 is used to evaluate the magnified current exiting from the amplifier. It must be noticed that R_{ON} and R_{OFF} equations are suitable only for the respective reading pulses. As a final remark, external shells of measuring probes are connected together in order to eliminate cables parasitic capacitances.

$$R_{ON} = \frac{\Delta V_{LRS}}{I_{LRS}} = (V_{read,CH1} - 2 \cdot V_{read,CH2}) \frac{50\Omega}{2 \cdot V_{read,CH2}} \tag{2.16}$$

$$I_{amp} = \frac{V_{read,CH3}}{A} \tag{2.17}$$

$$R_{OFF} = \frac{\Delta V_{HRS}}{I_{HRS}} = \frac{V_{read,CH1} - 2 \cdot 50\Omega \cdot I_{amp}}{2 \cdot I_{amp}} \tag{2.18}$$

2.3 Experimental application

This section is devoted to describe how processes and techniques outlined in sections 2.1 and 2.2 had been applied for the acquisition of this work outcomes. All process parameters and precise measuring conditions will be detailed in order to ensure accurate interpretation of results and of their limits.

2.3.1 Sputter rate evaluation

Before sputtering any layer, *Sputter Rate (SR)* evaluation is necessary in order to obtain a desired thickness. SR is defined as the thickness deposited per unit time at a fixed plasma power. In the following, all used materials data will be discussed.

- *Tantalum oxide* (Ta_2O_5): sputter rate values was measured by another group member at 11 W.
$$SR_{Ta_2O_5} = 2.83\frac{nm}{min}$$
- *Platinum* (Pt): as in the previous case, sputter rate was already given at 80 W.
$$SR_{Pt} = 36.14\frac{nm}{min}$$
- *Low purity copper* ($Cu\ LP$): even if SR was already provided, a double check on the value was performed after target removal and reinsertion into sputtering chamber. Figure 2.27 shows the XRR measurement for a layer sputtered at 10 W for 12.8 min. Analysis results are reported in table 2.3.

Cu low purity (10 W)	
Time	12.80 min
Thickness	30.00 nm
Sputter rate	2.34 $\frac{nm}{min}$

Table 2.3: *Low purity copper sputter rate data.*

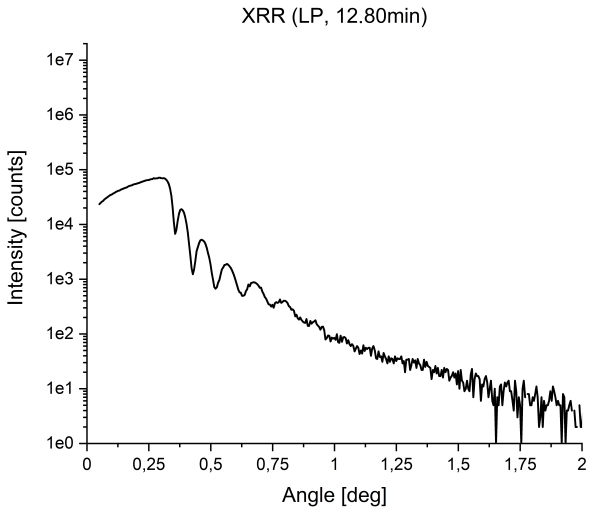

Figure 2.27: *XRR curve for low purity copper film, sputtered for 12.8 min at 10 W.*

- *High purity copper* (*Cu HP*): for this new target, the whole analysis was performed from scratch. In order to overcome the possibility of sputter rate nonlinear dependence over time, four layers of different thickness were analyzed. Figure 2.28 shows the XRR interferograms for all the layers, while table 2.4 reports the relative parameters and results.

Cu high purity (10 W)				
Time [min]	7.00	8.55	12.80	17.10
Thickness [nm]	15.14	18.88	26.93	35.78
Sputter rate $[\frac{nm}{min}]$	2.16	2.21	2.10	2.09

Table 2.4: *Low purity copper sputter rate data.*

A plot of the sputter rate time dependence is shown in figure 2.29. As can be observed, the relationship is nonlinear, despite the deviations are compatible with the uncertainty intrinsic in the deposition process. It is however taken into account and, for each thickness value falling between two data points, is used the SR value extracted from the segment uniting them.

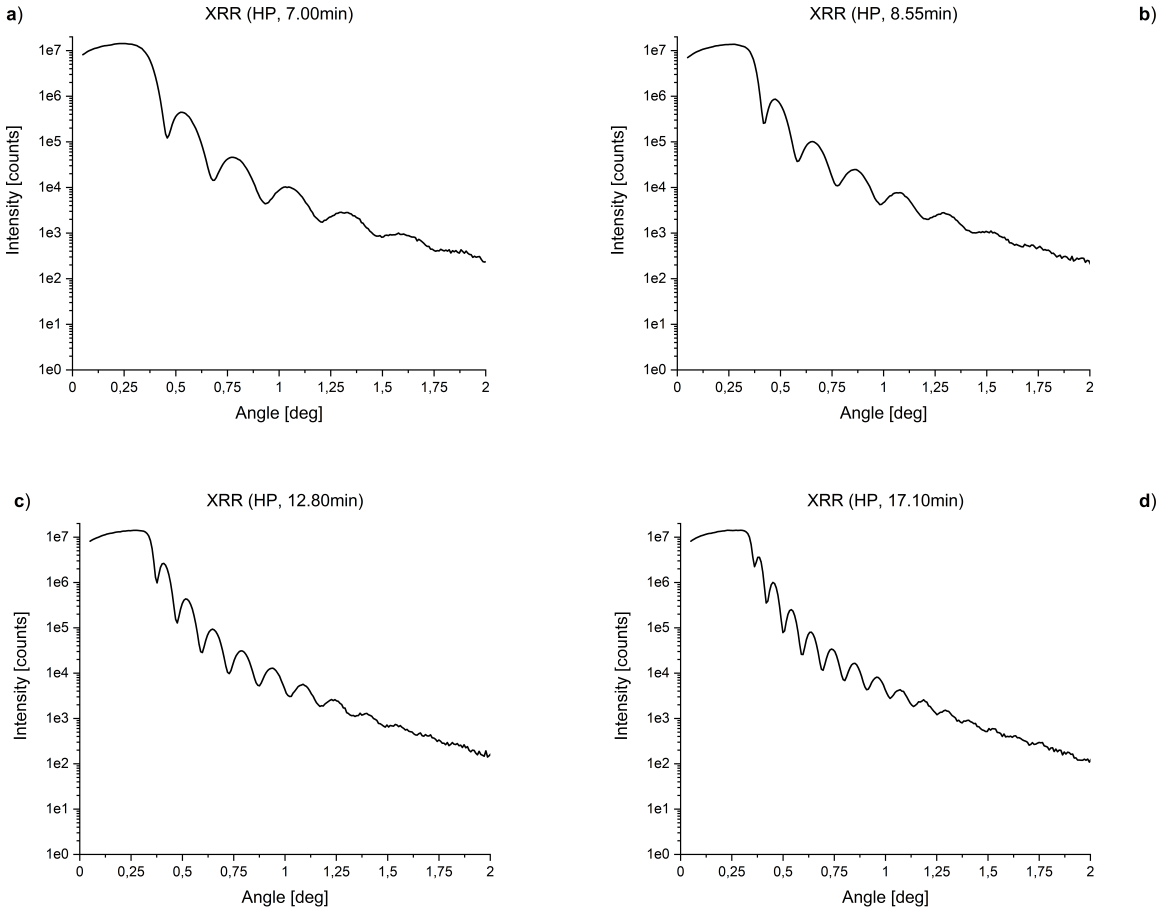

Figure 2.28: *XRR curves for high purity copper layer, sputtered at 10 W for 7 min (a), 8.55 min (b), 12.8 min (c) and 17.1 min (d).*

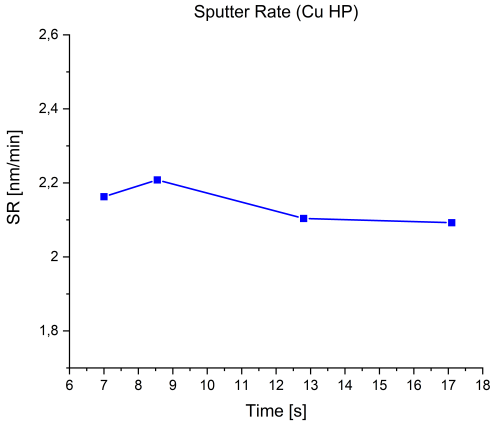

Figure 2.29: *High purity copper sputter rate as a function of time.*

2.3.2 Thin films deposition

Samples produced and characterized in this work have the structure depicted in figure 2.30, where bottom electrode is formed by a unique film and only top electrode is patterned (*common bottom electrode* configuration). A platinum BE 30 nm thick is deposited onto a 5 nm titanium film which acts as adhesion layer onto a silicon oxide substrate [80]. The latter is obtained by thermal oxidation of silicon, while Pt and Ti films are produced by electron beam deposition. Ta_2O_5 10 nm switching layer is deposited by means of reactive sputtering of a tantalum target with O_2 injection in the chamber. A photoresist coating is then patterned on top of this structure in order to be ready for the lift-off of successive layers. This process, together with the final dissolution of the resist will be detailed in section 2.3.3. Copper top electrode is consecutively sputtered with a thickness of 30 nm. Finally, in order to avoid copper oxidation due to environment exposition, 30 nm of platinum are used as a capping layer. Table 2.5 reports in details all the parameters used for sputtering deposition.

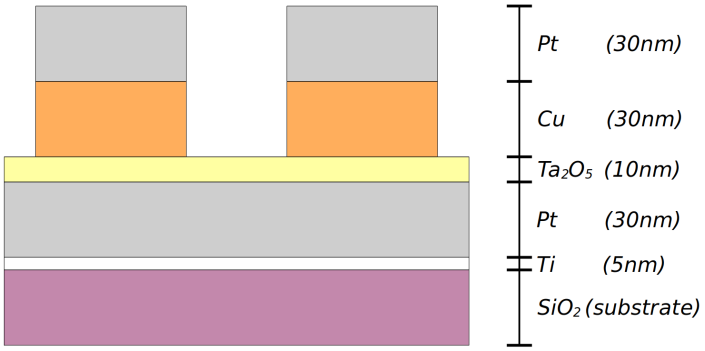

Figure 2.30: *Structure schematics of produced samples.*

Sputtering parameters							
Film	**Thickness [nm]**	**Target**	**Power [W]**	**Pressure [mbar]**	**Ar flow [sccm]**	**O_2 flow [sccm]**	**Time [min]**
Ta_2O_5	10	Ta	150	0.040	12	8	3.02
Cu (LP)	30	Cu (LP)	10	0.004	15	0	12.80
Cu (HP)	30	Cu (HP)	10	0.004	15	0	13.66
Pt	30	Pt	80	0.005	15	0	0.83

Table 2.5: *Sputtering parameters for each film deposition.*

2.3.3 Pattern transfer

As declared in section 2.1.3, top electrode patterning is performed by means of UV photolithography and lift-off. The whole process is described below in its all steps.

1. Photoresist is deposited onto Ta_2O_5 layer by spin coating at 4000 rpm for 40 s.
2. Soft bake is performed on an hot plate at 90 °C for 5 min.
3. Sample is exposed through the mask shown in figure 2.31 for 4.5 s.

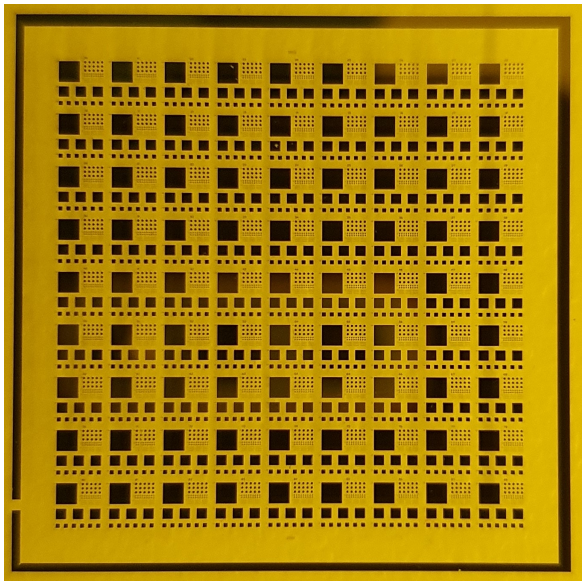

Figure 2.31: *Picture of the lithographic mask.*

4. Photoresist undergoes image reversal baking on an hot plate at 115 °C for 2 min.
5. Complementary part of the resist is made soluble through flood exposure for 14.5 sec.
6. Sample is immersed into the developer for 25 sec, then cleaned using deionized water and dried with nitrogen flow.

After copper top electrode and platinum capping layer are sputtered, acetone bath is used in order to complete the lift-off. Figure 2.32 reports a microscope picture of the obtained pattern. It consists in a matrix of sections, each of which contains several squared electrodes of different area. In detail, considering the square edge, each section contains: 1 electrode of 1 mm, 3 of 500 µm, 6 of 200 µm, 15 of 100 µm, 18 of 50 µm and 45 of 25 µm. For the sake of clearness, figure 2.32 shows only the three smallest dimensions.

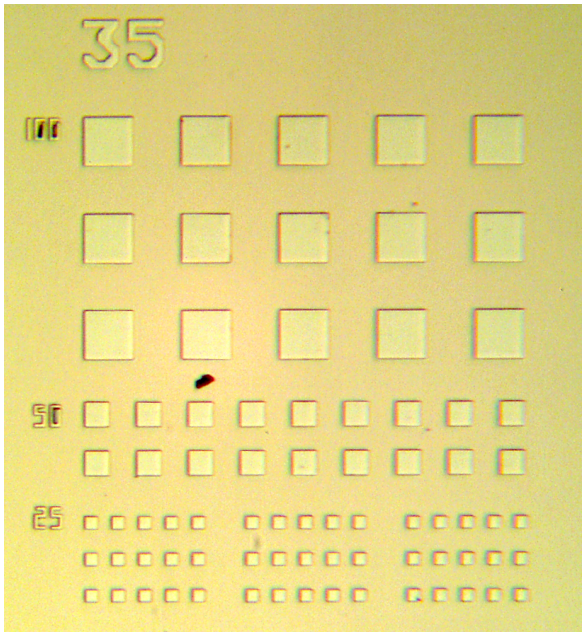

Figure 2.32: *Microscope image of patterned top electrodes.*

2.3.4 I-V sweeping

This characterization is performed by controlling the source meter through a custom made *Lua* script. A part from the flexibility in parameter variation, it implements a function which stops the positive voltage rising as soon current compliance is reached. This feature is important since permits to reduce time consumption and overcome the cycle to cycle changing in maximum voltage choice, necessary due to device variability. First step of sweeping measurements is electroforming, i.e. an initial high voltage positive stress for first conductive filament formation. Figure 1.11 reports a comparison between the initial forming positive branch and one of the successive. As can be seen, switching event is triggered at significant higher voltage than a standard setting. For this reason, current compliance is lowered by a thousand factor in order to limit the applied power and prevent breakdown. Specifically, current limit is set to $I_{CC,form} = 1\,\mu A$.

Sweeping parameters	
V_{min}	$0.9\,V$
I_{CC+}	$1\,mA$
SR	$296\,\frac{mV}{s}$

Table 2.6: *I-V sweeps measuring parameters.*

As a second step, device must undergo some cycles before reaching a stable behavior. Typically 20 cycles are sufficient. Table 2.6 details the electrical parameters used for all measurements. I_{CC+} indicates the current compliance applied only on the positive ramp, because reset process often requires a significantly higher absolute current value. For devices analyzed in this work, a reset current $I_{reset} = 40\,mA$ is typically necessary. This asymmetry impacts negatively on source meter current sensitivity (I_{sens}), which cannot be lower than the maximum current magnitude measured. This is due to the automatic application of a compliance equal to sensitivity value, not permitting cell reset. For this reason, sweeping results presented in this work are obtained with $I_{sens} = 40\,mA$. Measurements in HRS state are particularly afflicted by this limitation, considering that current is usually in the sub-microampere range.
With this technique V_{set}, V_{reset}, R_{HRS}, R_{LRS} and resistance ratio ($\frac{R_{HRS}}{R_{LRS}}$) are obtained. In particular set and reset voltage are defined as the values at which state transition starts, and R_{HRS} and R_{LRS} are both evaluated in the positive branch with a read voltage equal to 0.1 V. Due to high cycle to cycle device variability, each figure of merit is studied statistically, with a normal distribution constructed on 60 cycles. This value has been fixed considering that statistics is observed to converge from this point on, as shown in figures 2.33 - 2.34.

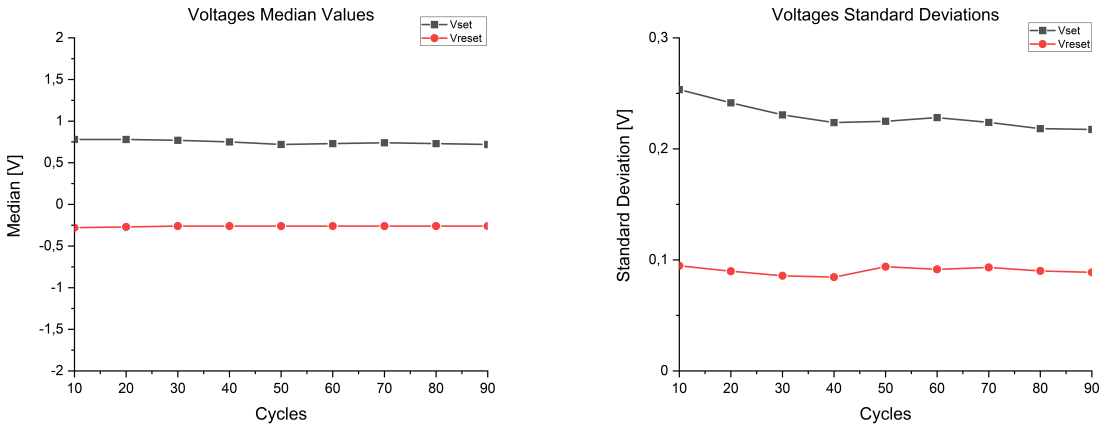

Figure 2.33: *V_{set} and V_{reset} median values (left) and standard deviations (right) as a function of cycles number.*

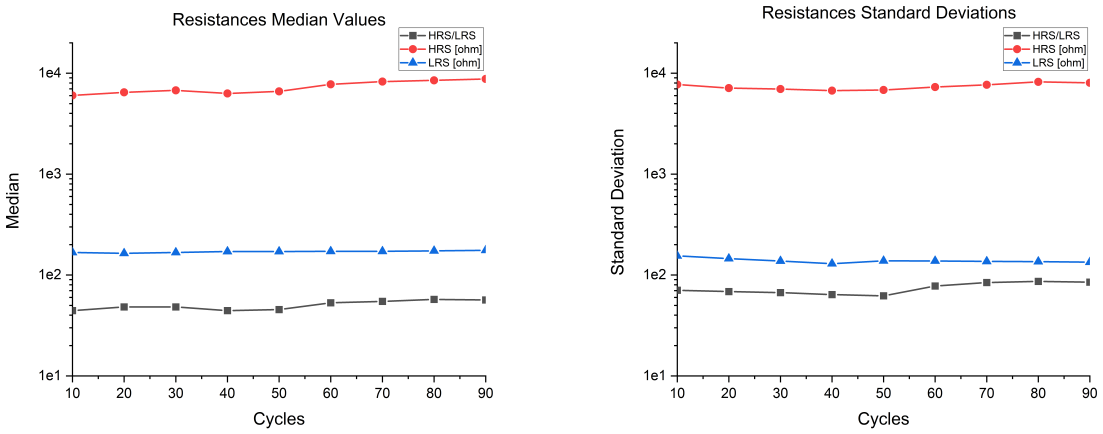

Figure 2.34: *HRS, LRS and resistance ratio median values (left) and standard deviations (right) as a function of cycles number.*

2.3.5 Cyclic voltammetry

Cyclic voltammetry measurements are performed with the same setup described for I-V sweeps. All the devices are characterized by performing three cycles, due to high observed switching probability in the fourth one. Voltage swing goes from -2.9 V to 2.9 V with a varying sweep rate, which, in particular, takes the following values: 74 $\frac{mV}{s}$, 222 $\frac{mV}{s}$, 370 $\frac{mV}{s}$, 518 $\frac{mV}{s}$, 666 $\frac{mV}{s}$, 814 $\frac{mV}{s}$, 962 $\frac{mV}{s}$. Due to SR set voltage dependence described in section 2.2.1, devices are always observed to form in the first cycle for the two lowest sweep rates. For this reason, in these conditions, voltage range is reduced to [-2.1 V, 2.2 V]. To conclude, all the measurements are done with a current sensitivity value of 1.6 nA.

2.3.6 Set time evaluation

Set time is evaluated by applying a voltage pulse with the general shape depicted in black in figure 2.25. V_{app} is made vary from 0.7 V to 1.95 V with a step of 0.25 V, while V_{reset} is kept constant at 1.95 V and V_{read} at 0.2 V. Respective pulses durations are called t_{app}, t_{reset} and t_{read}, while the 0 V pauses between them are called t_{pause}. In order to ensure correct device switching, their values are varied with applied voltage. Detailed waveforms intervals are reported in table 2.7. For each voltage point, a number of measurements ranging from 20 to 32 are recorded and analysed statistically, as for I-V sweepings. This different number of data is due to difficulty in acquiring points for some devices, caused by cells breaking. In details, for high purity copper, 20 points at 0.7 V, 0.95 V, 1.45 V,

1.7 V and 23 points at 1.2 V are recorded. For low purity copper, 20 points at 0.7 V, 0.95 V, 27 at 1.2 V, 32 at 1.45 V and 28 at 1.7 V are measured. In order to ensure similar initial conditions, only values with HRS resistances at beginning of voltage application in the range between 7 $k\Omega$ and 13 $k\Omega$ are considered valid.

Pulses time intervals				
$\mathbf{V_{app}}$ **[V]**	$\mathbf{t_{app}}$	$\mathbf{t_{reset}}$	$\mathbf{t_{pause}}$	$\mathbf{t_{read}}$
0.70	11 s	2.0 s	2.0 s	2.0 s
0.95	9 s	1.5 s	1.5 s	1.5 s
1.20	100 ms	10 ms	10 ms	10 ms
1.45	100 ms	20 ms	10 ms	10 ms
1.95	50 ms	30 ms	10 ms	10 ms

Table 2.7: *Pulses widths function of the applied voltage.*

Equipment sensitivity strongly depends on applied voltage rising time and, when it is comparable with set time, recorded values are discarded. It must be noticed that 0.7 V and 0.95 V results are extracted manually on the oscilloscope. In the other cases, a MATLAB script is used to first smooth the noisy signals and then extract the desired values.

Chapter 3

Results

In this chapter, measurements results will be reported and discussed. In the first part, I-V cycling and electroforming results will be discussed with particular focus on copper purity impact on devices variability. In the second part, based on cyclic voltammetry the electrochemical reactions at the Cu/Ta_2O_5 interface will be discussed. Finally, set time results will be used for discussing switching kinetics dependence on copper purity. As final remark, all data are acquired at temperature $T = 23\,°C \pm 3\,°C$ and relative humidity $RH = 22\,\% \pm 4\,\%$.

3.1 Devices variability

I-V cycling measurements were performed on $Pt/Ta_2O_5/Cu$ devices with a low (13 devices) or high purity (25 devices) copper top electrode of area 25*25 μm^2. In the following, raw data are compared by means of box plots, while figures of merit statistics are obtained through normal distribution fitting.
In order, figure 3.1 reports set voltage, reset voltage, HRS resistance, LRS resistance and resistance ratio box plots for all tested samples. In this plots, whiskers represents the 5^{th} and the 95^{th} percentiles, colored box borders the 25^{th} and the 75^{th} percentiles, while inner line indicates the median value. From the statistical point of view, measured data have a probability of 50 % to fall in the colored region and of 90 % between lines whiskers. Values depicted as dots are detected in 10 % of the measurements and can be considered outliers. Table 3.1 reports average statistical description of the same quantities in terms of mean value and absolute and relative standard deviations (St.Dev.). The latter is obtained by dividing the absolute one by the mean value and is expressed in percentage. In tables from A.1 to A.4 (in appendix A) are shown normal distribution fitting results for each device.

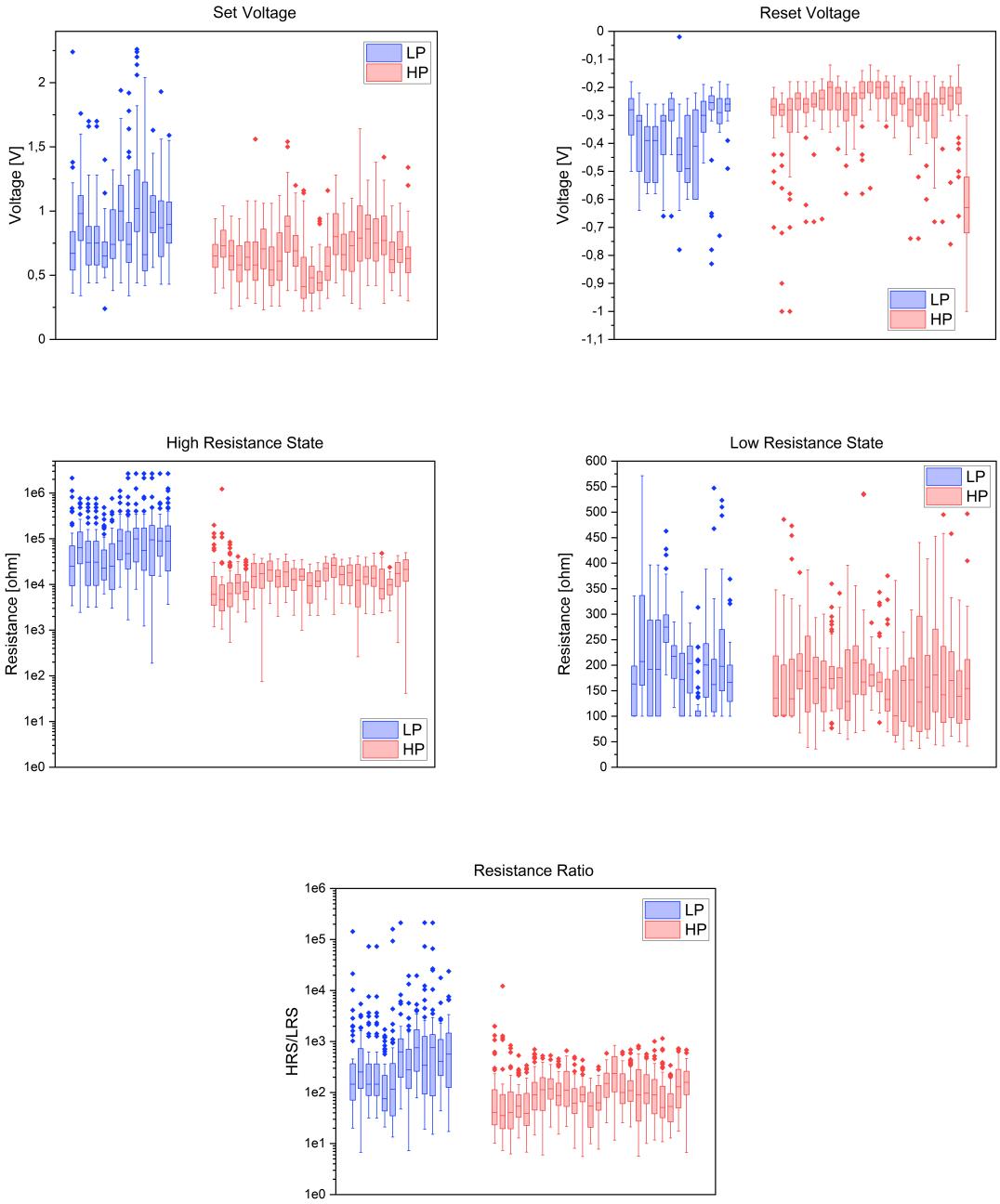

Figure 3.1: *V_{set}, V_{reset}, HRS resistance, LRS resistance and resistance ratio box plots for low purity (blue) and high purity (red) copper devices.*

It can be observed that average absolute standard deviation is always significantly lower

in high purity copper samples, with reset voltage showing the lowest difference ($\approx 19\,\%$). Percentual values follow the same behavior, except from V_{reset}, where an inversion arises. Considering that it concerns relative standard deviation only, deriving from lower HP absolute mean value, it can be considered in line with the other results. It must however be noticed that standard deviations are globally very high, not permitting any comparison between mean values. For this reason, despite average mean values being lower (in magnitude) for all the parameters, no deduction can be made.

Average Statistics Data						
Quantity	**Mean**		**St.Dev (abs.)**		**St.Dev. [%]**	
	HP	**LP**	**HP**	**LP**	**HP**	**LP**
$\mathbf{V_{set}}$ **[V]**	0.677	0.908	0.197	0.378	29.440	41.307
$\mathbf{V_{reset}}$ **[V]**	-0.224	-0.360	0.083	0.103	29.486	28.354
$\mathbf{R_{HRS}}$ **[Ω]**	17.824E+3	417.678E+3	17.711E+3	1.868E+6	85.193	368.878
$\mathbf{R_{LRS}}$ **[Ω]**	179.873	549.272	143.015	2775.878	72.646	224.083
$\mathbf{R_{HRS}/R_{LRS}}$	1.497E+2	2.666E+3	2.043E+2	12.291E+3	117.124	376.098

Table 3.1: *Set voltage, reset voltage, HRS resistance, LRS resistance and R_{HRS}/R_{LRS} ratio statistics data. Mean value, absolute and percentual standard deviation (St.Dev.) are reported.*

Same approach is used for electroforming voltage study. In this case, five LP and six HP samples were tested and 30 device each were formed. Furthermore, a comparison is made between devices with 25*25 µm^2, 50*50 µm^2 and 100*100 µm^2 electrode area.
Figure 3.2 depicts forming voltage box plots comparing HP and LP samples in increasing area order, while table A.5 (in appendix A) reports respective statistical parameters. Global voltage dependence on area is shown in figure 3.3 and table 3.2 summarizes average statistical values for all the samples. In the former figure, each box plot groups all devices data for the respective area and purity.
Significant standard deviation is observed also in these measurements. For this reason no conclusions can be derived from mean values, despite HP ones showing progressive reduction with electrode area increasing. Focusing on standard deviation, high purity copper samples do not show any trend. In low purity copper ones instead, it demonstrates an increment together with electrode area enlargement. In details, the LP average variability is lower than the HP one for 25*25 µm^2 and 50*50 µm^2, while overcomes it for 100*100 µm^2.

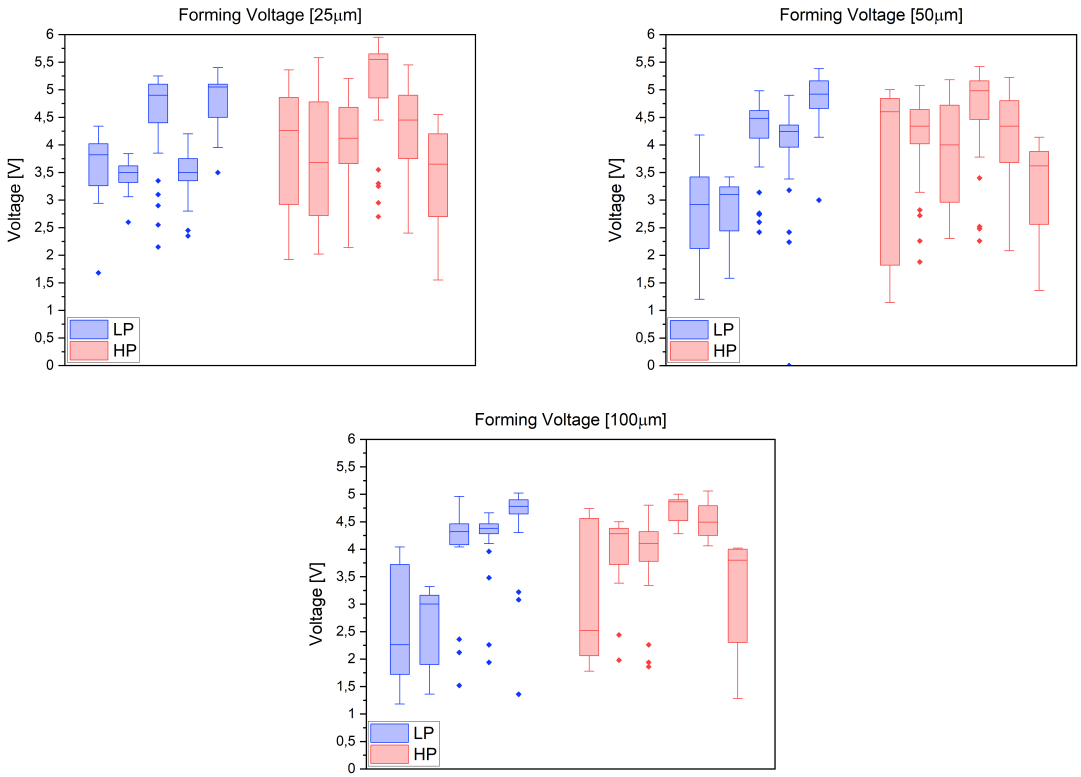

Figure 3.2: *Electroforming voltage box plots for low purity (blue) and high purity (red) copper devices with 25 µm, 50 µm and 100 µm edge top electrodes.*

Average Forming Voltage						
Electrode edge [µm]	**Mean [V]**		**St.Dev. [V]**		**St.Dev. [%]**	
	HP	**LP**	**HP**	**LP**	**HP**	**LP**
25	4.212	3.973	0.981	0.540	23.615	13.425
50	4.040	3.706	1.022	0.749	25.921	21.192
100	4.056	3.571	0.642	0.814	17.441	24.722

Table 3.2: *Average values of electroforming statistics data as a function of top electrodes edge. Mean value, absolute and percentual standard deviation (St.Dev.) are reported.*

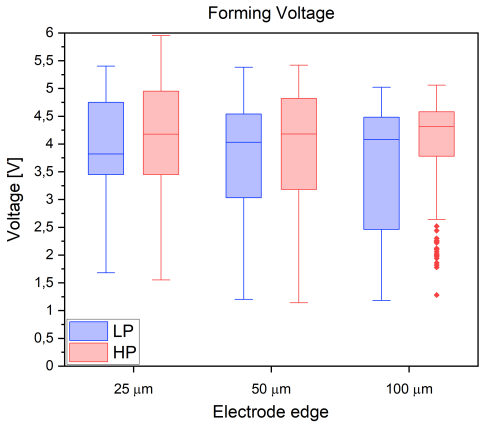

Figure 3.3: *Global forming voltage box plots as a function of top electrode dimension for low (blue) and high (red) purity copper devices. Each box plot groups all devices data for the respective area and purity.*

From this results, a negative impact of active electrode material impurities on the device behavior variability can be deduced. Although an accurate understanding of physical and/or chemical reasons would require detailed material characterizations, hypothesis can be formulated. As reported by Celano *et al.* in ref. [81] formation of multiple filaments with different morphology, which alternately shortcuts the electrodes in different cycles, is a key phenomenon at the basis of switching variability. It can be hypothesised that uncontrolled impurities presence can lead to different composition between filaments. This effect would alter stochastically filaments properties, causing variability increasing. For what concerns resistances, compositional variation would cause an additional resistivity difference between filaments. This could have strong impact on resistance variability, taking into account that the R_{HRS} measured values are low enough to consider tunnel resistance negligible (as described in section 1.2.1.4). Regarding voltages variability, the presence of uncontrolled impurities can give rise to parallel redox processes - such as impurities redox - which would introduce additional uncertainty. This hypothesis is supported by cyclic voltammetry results, as described in section 3.2. The independence of HP electroforming voltage variability could be caused by impurities distribution. Their lower concentration, indeed, increases the probability of having homogeneous copper regions at the interface, especially at low dimension. Being compositional equivalents, they would show similar oxidation energies, leading to a greater number of possible equivalent filament. Low purity copper instead, has higher probability of compositional variation at the interface. For this reason, a lower density of equivalent anodic dissolution centers can

be expected. Smaller electrode area would so reduce the number of possible concurrent filaments, causing standard deviation contraction. As reported by Al-Mamun *et al.* in [82], also interface roughness can play an important role in forming variability. It is however excluded by XRR measurements, which roughness results are comparable: 0.342 nm for LP and 0.339 nm for HP samples. As a final remark, implantation of impurities during the sputtering deposition of copper top electrode cannot be excluded at present, leading to a possible higher contamination of the oxide layer in LP samples.

3.2 Cu/Ta_2O_5 interface properties

For high and low purities of the 25*25 µm^2 copper top electrode, CV was used to analyze the interface properties of $Pt/Ta_2O_5/Cu$ samples. Figure 3.4 shows voltammograms obtained for each sample. Different sweep rates were investigated. For comparability reasons, only measurements with $SR = 370\,\frac{mV}{s}$ are shown. The observed (and later discussed) properties are the same for all different sweep rates.
Top-left figure reports peak labeling used in results discussion: the most negative reduction peak is named **A**, the less negative one **B** and the oxidation one **C**. It must be noticed that in the first cycle, two reduction peaks are present and no oxidation peak can be resolved. From the second cycle only one reduction peak is observed (probably a superposition of A and B) and one oxidation peak arises. For simplicity, this peak will be called B as well. As reported by Tappertzhofen *et al.* in ref. [83], Cu standard redox potentials can be considered to have the same trend of reactions in aqueous solution. With this assumption, peak A would be related to Cu^{2+}/Cu reduction, B to Cu^{+}/Cu reduction and C to an overlapping of Cu^{+}/Cu^{+} and Cu/Cu^{2+} oxidations. LP samples produces oblique reduction peaks, due to superposition with leakage current. This component cannot be mathematically excluded since its characteristics is unknown. For this reason, flex point with higher absolute value is chosen as peak voltage, introducing however additional uncertainty to the measure. It can also be observed a current magnitude reduction from the second cycle caused by typical copper passivation, i.e. formation of a copper oxide layer [84]. Even if a precise criterion for quantitative passivation is difficult to be defined, it is graphically deduced that it has stronger impact on HP devices, suggesting higher tendency of high purity copper electrode to react with oxygen ions. Being peak current magnitude proportional to the reaction rate, two other hypothesis can be made. In LP cells, the impurities less noble than Cu (such as Ni or Fe) could participate to parallel redox processes. It is also possible that their presence increase copper electrode catalytic activity toward moisture. In both cases, these processes could occur at voltage compara-

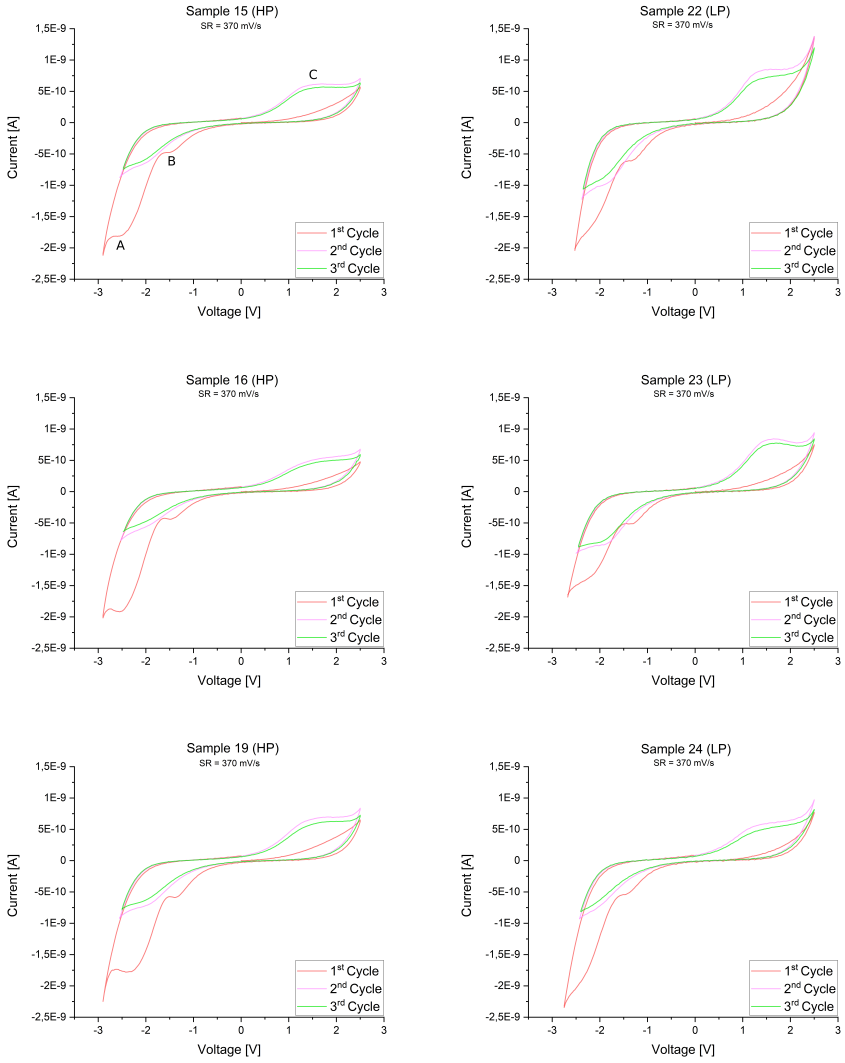

Figure 3.4: *Cyclic voltammetry measurements for all the sample measured. For sake of simplicity, only curves with sweep rate* $SR = 370\,\frac{mV}{s}$ *are shown.*

ble to copper ones, contributing to peak growth.

Samples are measured at different time lapse from production. In details, HP devices measurements took place at 125 days aging, while LP ones at 70 days. In order to exclude different aging influence on results, low purity samples are measured also at 125 days and results are reported in figure 3.5 and table 3.3. As it can be observed, only reduction peaks currents in the first cycle are affected. This effect can be adducted to copper dissolution which leads to increased density of species in the diffusion layer. Peak voltages (V_{peak}) are instead not affected, permitting to exclude aging impact on this work

data. It must be noticed that this comparison is performed at $SR = 370\,\frac{mV}{s}$ only, but is assumed to be valid for all the measurements.

Peak Voltage [V] (cycle 1)		
Peak	**70 Days**	**125 Days**
A	-2.525 ± 0.115	-2.517 ± 0.038
B	-1.483 ± 0.076	-1.400 ± 0.066

Peak Voltage [V] (cycle 2)		
Peak	**70 Days**	**125 Days**
B	-2.167 ± 0.038	-2.133 ± 0.029
C	1.775 ± 0.087	2.000 ± 0.130

Peak Voltage [V] (cycle 3)		
Peak	**70 Days**	**125 Days**
B	-2.233 ± 0.063	-2.158 ± 0.038
C	1.875 ± 0.303	2.092 ± 0.063

Table 3.3: *Peak voltage mean data for 70 and 125 days old low purity copper devices.*

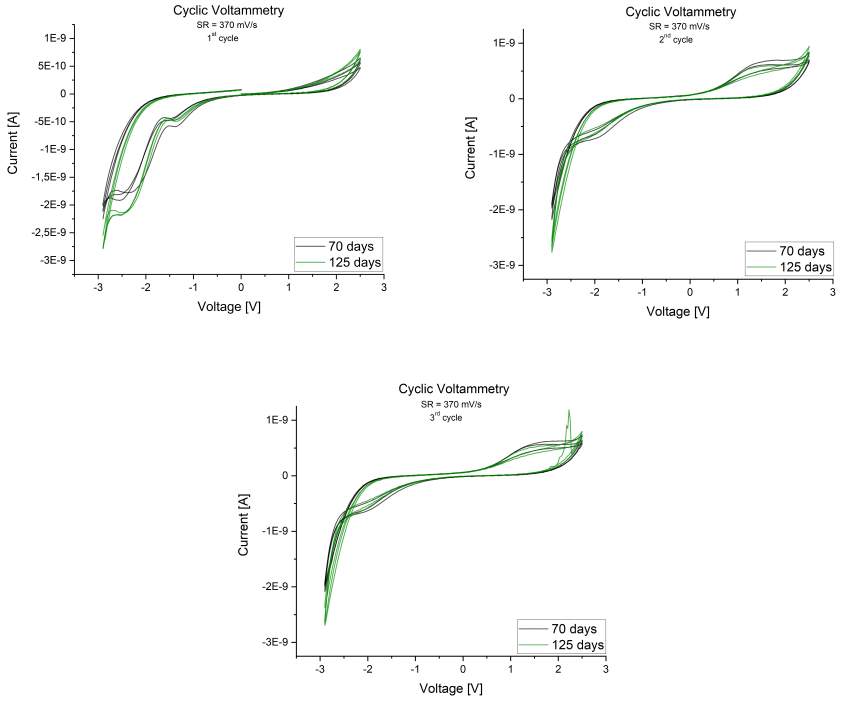

Figure 3.5: *Cyclic voltammetry measurement comparisons at 70 days (black) and 125 days (green) aging for low purity copper devices.*

Figure 3.6 depicts exemplary voltammograms at different sweep rates for samples 22 (HP) and 15 (LP). Table 3.5 reports peak voltages data statistics for each SR obtained by normal distribution fitting over all samples. It can be noticed that HP and LP voltage uncertainty intervals always overlap, except from the case marked with an asterisk. This

mismatch can be considered caused by difficulty in defining precise peak position. It is confirmed by null standard deviation in HP value, which is very likely an elaboration artifact. Global result, however, indicates peak voltage independence on purity at every sweep rate. Being V_{peak} relative to the energy needed from the ion to overcome the energy barrier and take part to the reaction [78], it can be supposed an invariance in the free energy profile by changing copper purity.

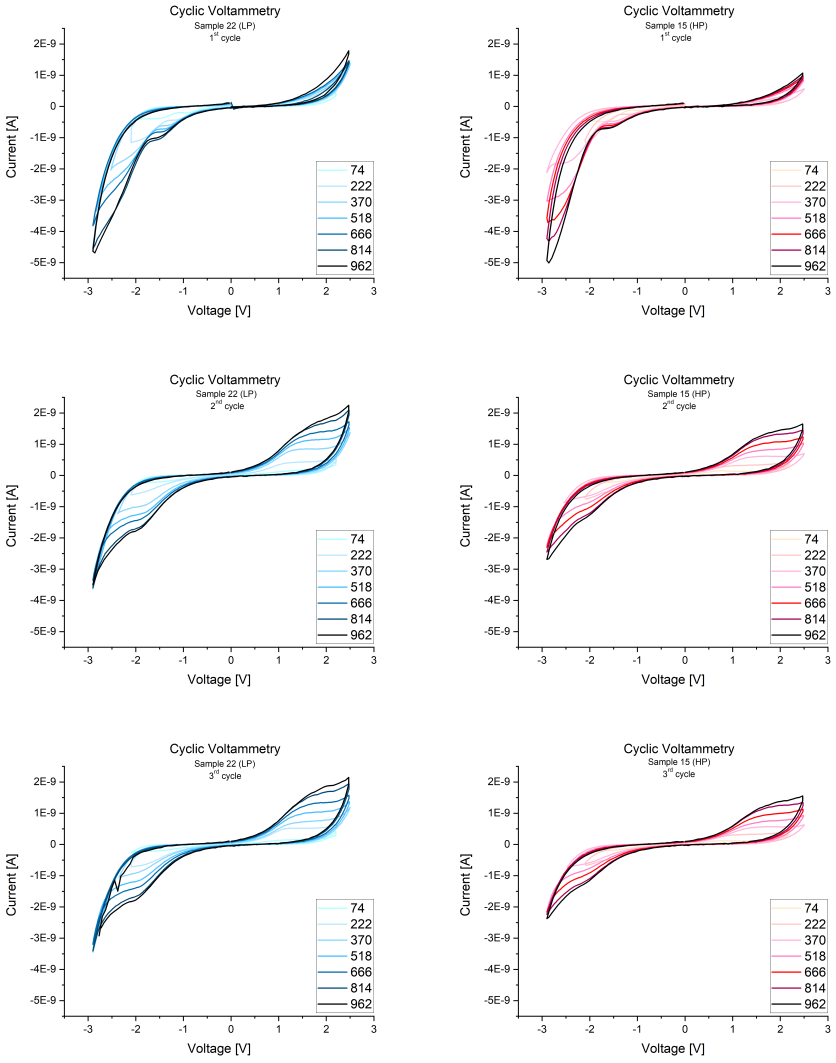

Figure 3.6: *Cyclic voltammetry measurements as a function of sweep rates. Low purity copper devices are shown on left while high purity on right. Legend reports sweep rates values in* $\frac{mV}{s}$.

A further analysis is performed by evaluating exponential V_{peak} - SR characteristics through fitting. In general, it is observed a shift of oxidation and reduction peak voltage magnitudes towards higher values when sweep rate is increased. Equations 3.1 and 3.2 represent curves used for fitting, where A, τ, t_0, and R_0 are fitting parameters. R_0 and τ data are shown in table 3.4 together with their uncertainty for each peak. Figure 3.7 shows V_{peak} - SR scatter plots together with fitted curves. Also in this case, all data result compatible, indicating same sweep rate dependence. Peaks shift is a well known effect of irreversible redox processes, caused by charge transfer inhibition at fast scan rate [85]. In this condition, reaction rates are dominated by ion diffusion which forces a minimum time needed for an ion to take part to the reaction and so higher voltages at faster SR. For this reason, HP and LP samples can be deduced to have the same copper diffusion coefficient and so mobility, according to Nernst-Einstein equation (eq. 2.12). Table 3.6 reports mobilities of three HP and LP devices, evaluated through procedure explained in section 2.2.2. Considering the presence of reduction current in the Randles–Sevcik equation (eq. 2.11), and its variation with time observed in aging measurements, two devices with same aging are used. It can be seen that ion mobility values are in the same order of magnitude and do not show any trend, confirming deduction made for SR dependence. It can be concluded that copper redox barriers at electrode/oxide interface and ion mobility are equal for HP and LP copper. Furthermore, the presence of more impurities in LP sample leads to higher reaction rates, possibly caused by the arising of parallel reactions at the interface. This effect could contribute to higher variability in I-V sweeping measurements, due to the uncontrolled distribution and composition of the impurities.

$$V_{peak} = A \cdot e^{-\frac{SR}{\tau}} + V_0 \tag{3.1}$$

$$V_{peak} = A \cdot e^{R_0 \cdot SR} + V_0 \tag{3.2}$$

Fitting Parameters (cycle 1)		
Peak	**HP**	**LP**
A ($\tau\,[mV/s]$)	351.293 ± 104.339	364.064 ± 84.051
B ($\tau\,[mV/s]$)	274.980 ± 55.792	305.142 ± 84.940

Fitting Parameters (cycle 2)		
Peak	**HP**	**LP**
B ($\tau\,[mV/s]$)	143.127 ± 80.566	275.827 ± 106.338
C ($R_0\,[s/mV]$)	4.060E-3 ± 1.160E-3	5.800E-3 ± 1.500E-3

Fitting Parameters (cycle 3)		
Peak	**HP**	**LP**
B ($\tau\,[mV/s]$)	129.481 ± 68.918	333.158 ± 152.841
C ($R_0\,[s/mV]$)	30.138E-3 ± 27.380E-3	4.630E-3 ± 2.540E-3

Table 3.4: *Fitting data of voltage dependence on swep rate for each peak.*

Peak A Voltage [V] (cycle 1)		
SR $[\frac{\mathbf{mV}}{\mathbf{s}}]$	**HP**	**LP**
74	-1.778±0.231	-1.855±0.182
222	-2.015±0.009	-2.040±0.026
370	-2.442±0.159	-2.533±0.126
518	-2.625±0.070	-2.707±0.020
666	-2.595±0.145	-2.775±0.026
814	-2.713±0.084	-2.805±0.055
962	-2.773±0.150	-2.860±0.000

Peak B Voltage [V] (cycle 1)		
SR $[\frac{\mathbf{mV}}{\mathbf{s}}]$	**HP**	**LP**
74	-0.978±0.077	-0.995±0.089
222	-1.235±0.023	-1.140±0.069
370	-1.467±0.038	-1.475±0.090
518	-1.517±0.053	-1.470±0.070
666	-1.545±0.104	-1.545±0.069
814	-1.650±0.055	-1.558±0.084
962	-1.625±0.113	-1.603±0.075

Peak B Voltage [V] (cycle 2)		
SR $[\frac{\mathbf{mV}}{\mathbf{s}}]$	**HP**	**LP**
74	-1.638±0.341	-1.642±0.026
222	-1.905±0.184	-1.625±0.023
370	-2.150±0.115	-2.242±0.038
518	-2.112±0.158	-2.217±0.053
666	-2.055±0.130	-2.205±0.000
814	-2.163±0.127	-2.218±0.064
962	-2.123±0.099	-2.232±0.075

Peak C Voltage [V] (cycle 2)		
SR $[\frac{\mathbf{mV}}{\mathbf{s}}]$	**HP**	**LP**
74	0.945±0.343	0.758±0.020
222	1.645±0.242	1.400±0.400
370	1.800±0.205	1.983±0.257
518	1.960±0.195	2.018±0.246
666	2.025±0.078	2.025±0.078
814	2.237±0.064	1.943±0.168
962	2.210±0.113	2.145±0.000

Peak B Voltage [V] (cycle 3)		
SR $[\frac{\mathbf{mV}}{\mathbf{s}}]$	**HP**	**LP**
74	-1.592±0.319	-1.687±0.018
222	-2.025±0.040	-1.630±0.035
370	-2.208±0.128	-2.258±0.058
518	-2.147±0.073	-2.252±0.020
666	-2.280±0.094	-2.310±0.026
814	-2.237±0.138	-2.328±0.032
962	-2.232±0.135	-2.297±0.075

Peak C Voltage [V] (cycle 3)		
SR $[\frac{\mathbf{mV}}{\mathbf{s}}]$	**HP**	**LP**
74	1.287±0.430	0.900±0.104
222	1.635±0.148	1.555±0.139
370	1.858±0.202	1.950±0.254
518	1.843±0.040	1.867±0.107
666	2.145±0.104	2.175±0.104
814	2.182±0.032	2.200±0.146
962 *	2.080±0.000	2.167±0.038

Table 3.5: *Peak A, B and C voltage mean values and relative standard deviation at different sweep rates (SR) for all cycles. The raw marked with * represents the single case in which values intervals do not overlap.*

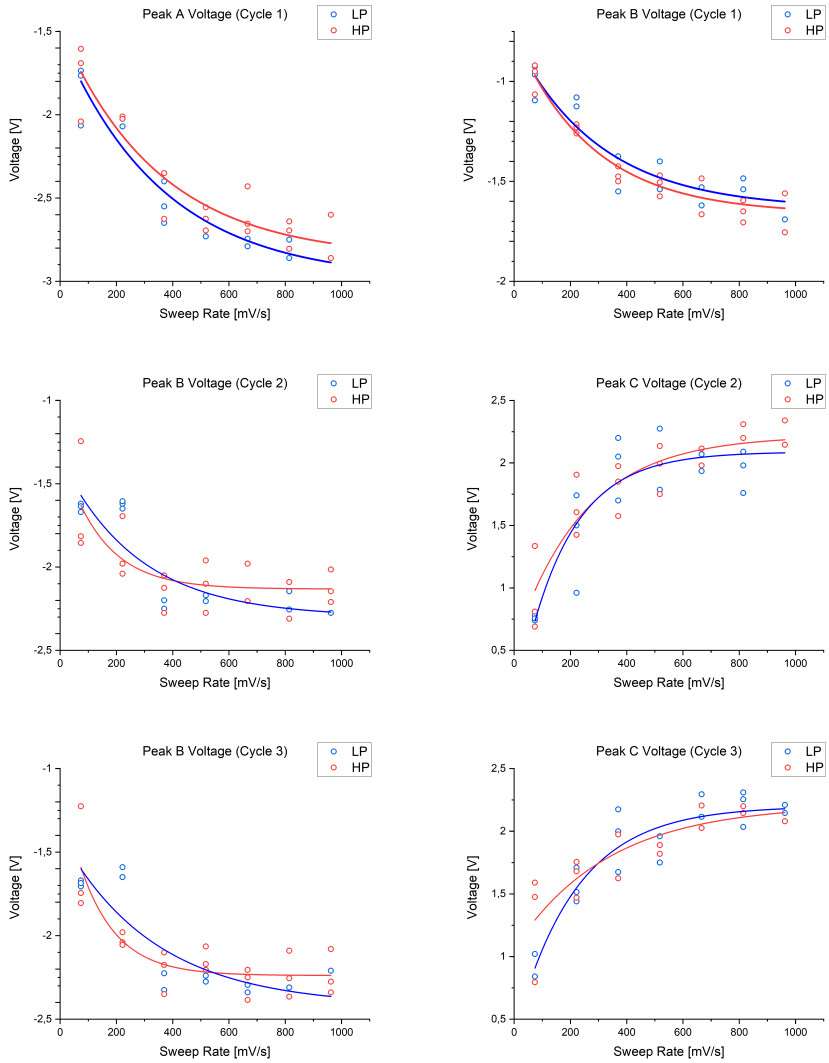

Figure 3.7: *Cyclic voltammetry peak voltages as a function of sweep rate for all cycles. Circles represents raw date while solid lines respective exponential fitting. High purity copper measurements are reported in red and low purity copper ones in blue.*

Cu mobility (μ) $[\frac{cm^2}{Vs}]$	
HP	**LP**
8.959E-11	1.890E-11
1.330E-10	3.599E-11
6.210E-11	1.010E-10

Table 3.6: *Evaluated copper ion mobility. Each value corresponds to a different device.*

3.3 Switching kinetics

Pulse measurements are performed on $Pt/Ta_2O_5/Cu$ devices with $25*25\,\mu m^2$ electrode areas after reaching stable bipolar switching during I-V sweeping. Figure 3.8 shows set time box plots as a function of applied voltage for high and low purity copper top electrode. Table A.6 (in appendix A) reports measured data while table 3.7 relative statistical parameters. It can be observed that standard deviations are too high for permitting mean values comparison. It is however important to underline that low purity copper devices demonstrate, at each voltage, the possibility of setting with lower time - i.e. are able to switch faster - even if with low probability. In details, at $V_{app} = 1.7\,V$, LP can show set time up to 50 ns, while HP only 2 µs.

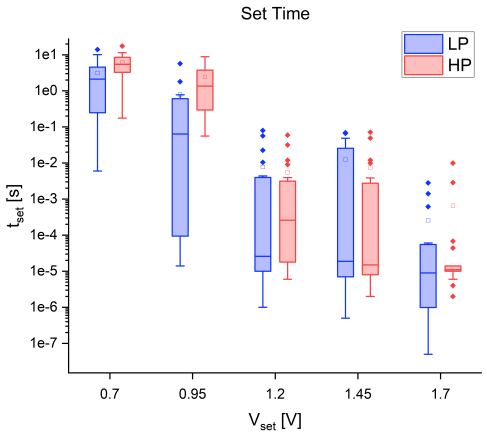

Figure 3.8: *Set time box plots for low purity (blue) and high purity (red) copper as a function of applied voltage.*

Focusing on standard deviation, it can be noticed a trend in St.Dev. percentual values. HP variability is progressively increasing with applied voltage and overcomes LP one starting from 1.2 V. The different behavior that was observed during I-V sweep analysis can be considered partially caused by cells easy breaking down during pulse measurements, which forces each set of data to consists of multiple devices. For this reason, a possible device to device variability contribution is added to cycle to cycle one. Furthermore, it is possible that a single cell is less variable in I-V sweeps with respect to pulse measurements due to different kinetics under stimuli of different nature. Moreover, it must be taken into account that the standard deviation is higher for HP devices in a voltage range which exceeds the applied voltage during I-V sweeping.
In order to understand switching kinetics, as described in section 1.2.1.3, a two phase

Set time [s]						
V_{app} [V]	**Mean [s]**		**St.Dev. [s]**		**St.Dev. [%]**	
	HP	**LP**	**HP**	**LP**	**HP**	**LP**
0.7	6.246	3.119	3.997	3.735	63.987	119.763
0.95	2.427	0.803	2.722	1.734	112.140	215.886
1.2	5.530E-03	7.730E-03	1.364E-02	1.874E-02	246.725	242.243
1.45	7.410E-03	1.232E-02	1.874E-02	2.070E-02	252.974	167.993
1.7	6.542E-04	2.578E-04	2.280E-03	6.307E-04	348.844	244.676
Average St.Dev.			**1.351**	**1.102**	**204.934**	**198.112**

Table 3.7: *Set time statistics data. Mean value, absolute and percentual standard deviation (St.Dev.) are reported. Each row shows data for a different applied voltage (V_{app}), while last row report standard deviations average values.*

exponential fit is performed on the raw data. Nucleation region is considered to be out of the measuring range since it is usually observed below 0.2 V, as reported by Menzel *et al.* in ref. [38]. Starting from general data trend, 0.7 V - 1.2 V and 1.2 V - 1.7 V was chosen as fitting intervals. Figure 3.9 reports separately HP and LP box plots and respective fits.

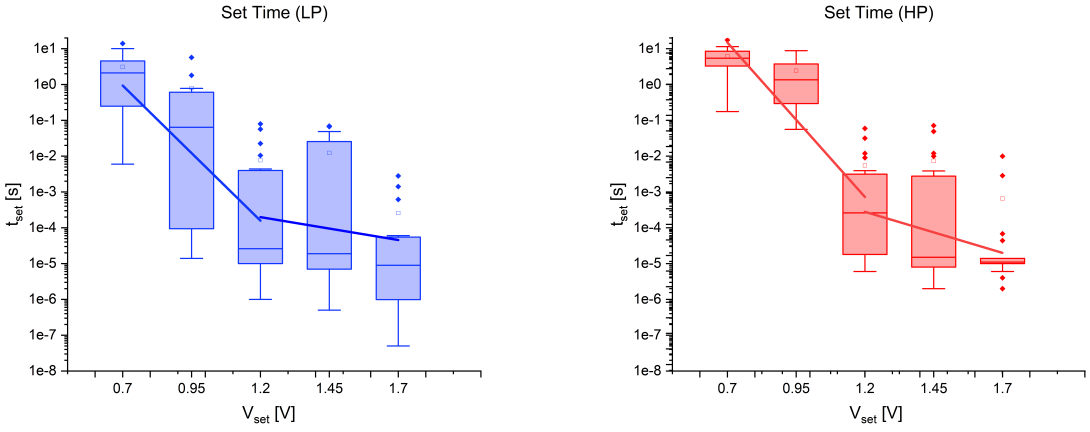

Figure 3.9: *Set time box plots as a function of applied voltage and exponential fittings. Low purity copper devices (blue) are shown on left while high purity (red) on right.*

The fits are compared in figure 3.10 and their slopes are reported in table 3.8. The latter could be expressed in two different units, s/V and mV/dec. The last one is typically used for cells comparisons, while the first one could be used to evaluate the charge transfer coefficient α. Slope uncertainties are overlapping, so no variation with copper purity can be deduced. However, LP devices show a significant lower set time at low voltage. This

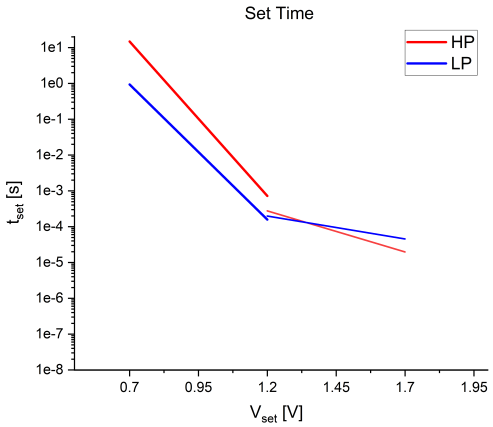

Figure 3.10: *Set time as a function of voltage exponential fit curves comparison. High purity copper fitting is reported in red and low purity copper one in blue.*

Slope				
Purity	**LP**		**HP**	
Voltage range [V]	**0.7-1.2**	**1.2-1.7**	**0.7-1.2**	**1.2-1.7**
Slope [s/V]	17.378±2.097	2.943±1.900	19.861±1.576	5.272±1.750
Slope [mV/dec]	132.50	782.31	115.93	436.73

Table 3.8: *Fitting curve slopes in s/V and mV/dec.*

could be possibly explained by the higher reaction rate observed in cyclic voltammetry measurements (as described in section 3.2), which imply easier electron transfer and so faster switching in this voltage range. Moreover, Joule heating can play a role in set transition as discussed in section 1.2.2.4. As reported by Hust *et al.* in ref. [86], impurity presence increases copper thermal resistance favoring local heating. This effect could contribute to the observed fast switching of the samples with low purity copper. Considering that cathodic reactions are dominant during set process, α can be evaluated by means of equation 1.39, where only reductions are supposed rate limiting. Since it is not evident which kind of copper ion reduction occurs, and so the number z of electrons exchanged, evaluation is performed with $z = 1$ (Cu_+/Cu), $z = 2$ (Cu_{2+}/Cu) and $z = 1.5$ (a combination of previous two). Results are shown in table 3.9. Since literature studies propose $\alpha = 0.5$ as the most probable value in ECM cells [87], Cu^+/Cu can be considered as the dominant reduction process during set for both HP and LP cells.

Charge transfer coefficient (α)		
z	**LP**	**HP**
1	0.449	0.514
1.5	0.300	0.342
2	0.225	0.257

Table 3.9: *Charge transfer coefficient (α) extracted from fitting slopes. Evaluation is performed for z values equal to 1, 1.5 and 2.*

Chapter 4

Conclusions

In this work the impact of copper active electrode purity on the electrical behavior of $Pt/Ta_2O_5/Cu$ stack ECM memristive devices was studied. In particular, it were analyzed quasi-static figures of merit during forming and stable switching, electrochemical reactions at active elctrode/oxide interface and switching kinetics extracted from set time - voltage characteristics.

First part focused on the influence of purity on the forming and sweeping behavior by using I-V sweeps technique. During forming, low purity copper devices demonstrated a tendency in having lower variability while, after reaching stable switching, a growth in variability with impurities concentration increase was detected. Latter result was adducted to the presence of impurities in the filament, leading to local change in energy profiles, reaction rates (as supported also by cyclic voltammetry measurements) and resistivity. Low purity devices showed a forming variability reduction with active electrode scaling. This trend was guessed to be caused by a lower density of interfacial copper region possessing equivalent anodic dissolution reaction potentials with respect to high purity cells. For this reason, a significant reduction of possible competitive filaments was hypothesized to take place by shrinking the area. For high purity devices no trend was observed, suggesting higher similar composition electrode surface areas.

In the second part, electrochemical reactions at electrode/oxide interface was studied by means of cyclic voltammetry. Peaks voltages invariance with purity was observed, indicating no variations in redox reactions activation energies. Devices exposed also similar peak dependence on sweep rate, from which equivalent copper ions diffusion coefficients and mobilities was deducted. This hypothesis was confirmed by analytical evaluation

through Randles-Sevcik and Nernst-Einstein equation. The unique noticeable variation was in cycle to cycle electrode passivation, which is detected to be stronger for high purity copper, suggesting higher propension to reaction with oxygen ions. Furthermore, it were supposed for low purity samples increased reaction rates caused by less noble impurities reactions and improved catalytic activity towards moisture.

In the third part, switching kinetics was investigated by analyzing set time - voltage characteristics under constant voltage pulse measurements. From similar slopes in the electron transfer and ion diffusion rate limited regions, it was concluded equality in the charge transfer coefficient. Considering that typical value reported in literature is approximately 0.5, dominance of single electron transfer in cathodic reduction was evinced. Regarding raw time measurements, low purity cells demonstrated faster switching up to $t_{set} = 50\,ns$, while high purity ones showed as minimum value $t_{set} = 2\,\mu s$. This discrepancy was adducted to LP copper faster electron transfer due to higher reaction rates. A Joule heating contribution due to higher LP thermal resistance could not be excluded. Finally, greater variability is observed for high purity devices at $V_{app} \geq 0.95\,V$, suggesting possible different cells behavior between sweep and pulse stimuli.

These results suggest that impurities could have a positive effect on reaction rates, improving electron transfer and leading to faster switching. As a drawback, their uncontrolled nature could cause reproducibility issues. From the applicative standpoint, purity induced improved variability of switching can result fundamental both for digital and analog implementations. Particular attention must be paid to forming-free devices since high purity could have a detrimental effect when filament is not formed yet, as seen in electroforming measurements. If further experimental results would confirm this hypothesis, a better approach could be using low purity copper with miniaturized electrode area. Regarding memory application, where pulsed voltage stimuli are typically used, a more careful analysis must be performed. Indeed, a purity beneficial effect on switching variability is obtained at low voltages. In contrast, measured set time in this range are not compatible with applicative requirements and low purity cells show the capability of switching in significant lower time. For this reason, purity could have a negative impact in this voltage interval and pulse measurements analysis should be performed on more optimized cells in order to understand if it can be beneficial for this application.

In conclusion active electrode purity study showed to be a key point in the understanding of material parameters and memristive devices behavior relationship. It is a crucial

element in the definition of complete design rules for the realization of specific devices for target applications. Further investigations must still be done in order to globally understand impurities effect. An extension of this work could be done by following different possible strategies. Active electrode material can be changed in order to better understand the interplay between base metal composition and impurity amount. The latter can also be reduced or increased, studying so the relation between purity and device operations in a wider range. Considering that this work focused on the role of uncontrolled impurities, they could be inserted with controlled composition and distribution. Finally, inert electrode material could be substituted e.g. with titanium nitride, since platinum is report to form hillocks [88]. This protrusions cause high current peaks during reset processes, reducing control in filament dissolution and possibly contributing to variability. These analysis could represent a crucial part in electrode engineering for precise cell properties tuning.

Bibliography

[1] Moore G.E., "Cramming more components onto integrated circuits", in *Electronics*, v. 3, n. 8, April 1965.

[2] Prodromakis T., Toumazou C., Chua L.O., "Two centuries of memristors", in *Nature Materials*, v. 11, June 2012.

[3] Theis T.N., Wong H.S.P., "The end of Moore's law: a new beginning for information technology", in *IEEE Computing in Science and Engineering*, v. 19, June 2016.

[4] Lanza M. et al., "Recommended methods to study resistive switching devices", in *Advanced Electronic Materials*, v. 5, September 2018.

[5] Chen A., Datta S., Hu X.S., Niemier M.T., Rosing T.S., Yang J.J., "A survey on architecture advances enabled by emerging beyond-CMOS technologies", in *IEEE Design and Test*, v. 36, February 2019.

[6] Hoentschel J., Carter R. and Rice B., "VLSI-CMOS device technology scaling landscape based on fully-depleted SOI and 3D-FinFET technologies for the internet of everything era", in *The Electrochemical Society*, v. 77, 2017.

[7] Gale E., "TiO2-based memristors and ReRAM: materials, mechanisms and models (a review)", in *Semiconductor Science and Technology*, v. 29, 2014.

[8] Hoffman J., Pan X., Reiner J. W., Walker F. J., Han J. P., Ahn C. H., Ma T. P., "Ferroelectric field effect transistors for memory applications.", in *Advanced Materials*, v. 22, 2010.

[9] Apalkov D. et al., "Spin-transfer torque magnetic random access memory (STT-MRAM)", in *ACM Journal on Emerging Technologies in Computing Systems*, v. 9, 2013.

[10] Raoux S., Welnic W. and Ielmini D., "Phase change materials and their application to nonvolatile memories.", in *Chemical Reviews*, v. 110, 2010.

[11] Menzel S., Böttger U., Wimmer M., "Physics of the Switching Kinetics in Resistive Memories", in *Advanced functional materials*, v. 25, June 2015.

[12] Wu M., Ting Y, Chen J. and Wu W., (2019). "Low power consumption nanofilamentary ECM and VCM cells in a single sidewall of high-density VRRAM arrays", in *Advanced Science*, v. 6, 2019.

[13] Boukhobza J. and Pierre O., "Flash memory integration: performance and energy issues.", *Elsevier*, 2017.

[14] Zahoor F., Azni Z., Tun Z. and Khanday F. A., "Resistive random access memory (RRAM): an overview of materials, switching mechanism, performance, multilevel cell (mlc) storage, modeling, and applications.", in *Nanoscale Research Letters*, v. 15, April 2020.

[15] Jung M., Shalf J. and Kandemir M., "Design of a large-scale storage-class RRAM system.", in *Proceedings of the 27th international ACM conference on International conference on supercomputing*, June 2013.

[16] Dong X., Jouppi N. P. and Xie Y.,"A circuit-architecture co-optimization framework for evaluating emerging memory hierarchies", in *2013 IEEE International Symposium on Performance Analysis of Systems and Software (ISPASS)*, April 2013.

[17] Kvatinsky S., Belousov D., Liman S., Satat G., Wald N., Friedman E.G., Kolodny A., Weiser U.C., "MAGIC – Memristor Aided LoGIC", in *IEEE Transactions on Circuits and Systems II: Express Briefs*, v. 61, November 2014.

[18] Debjyoti B., Luca A. and Anupam C., "Technology-aware logic synthesis for ReRAM based in-memory computing", in *2018 Design, Automation & Test in Europe Conference & Exhibition (DATE)*, March 2018.

[19] Meenatchi J. et al., "Analyzing the monolithic integration of a ReRAM-based main memory into a CPU's die", in *IEEE Micro*, v. 39, September 2019.

[20] Sun Z., Pedretti G., Ambrosi E., Bricalli A., Wang W., Ielmini D., "Solving matrix equations in one step with cross-point resistive arrays", in *PNAS*, v. 116, n. 10, March 2019.

[21] Zoppo G., Marrone F. and Corinto F., "A continuous-time learning rule for memristor–based recurrent neural networks.", in *26th IEEE International Conference on Electronics, Circuits and Systems*, November 2019.

[22] Prakash A. and Hwang H., "Multilevel cell storage and resistance variability in resistive random access memory", in *Physical Sciences Reviews*, v. 1, 2016,

[23] Ielmini D., Waser R., "Resistive switching: from fundamentals of nanoionic redox processes to memristive device applications", *Wiley*, March 2016.

[24] Linn E., Rosezin R., Kügeler C and Waser R., "Complementary resistive switches for passive nanocrossbar memories", in *Nature Materials*, v. 9, April 2010.

[25] Nardi F., Larentis S., Balatti S., Gilmer D. C. and Ielmini D., "Resistive switching by voltage-driven ion migration in bipolar RRAM - Part I: experimental study", in *IEEE Transactions on Electron Devices*, v. 59, September 2012.

[26] Strukov D.B., Snider G.S., Stewart D.R., Williams R.S., "The missing memristor found", in *Nature*, v. 453, May 2008.

[27] Chua L.O., "Memristor - The missing circuit element", in *IEEE Transactions on Circuit Theory*, v. CT-18, n. 5, September 1971.

[28] Vongehr S. and Meng X., "The missing memristor has not been found", in *Scientific Reports*, v. 5, June 2015.

[29] Valov, I., Linn, E., Tappertzhofen, S,Schmelzer S., Van Den Hurk J., Lentz F. and Waser R., "Nanobatteries in redox-based resistive switches require extension of memristor theory", in *Nature Communications*, v. 4, April 2013.

[30] Linn, E., Menzel S., Ferch S. and Waser R., "Compact modeling of CRS devices based on ECM cells for memory, logic and neuromorphic applications", in *Nanotechnology*, v. 24, September 2013.

[31] Abdalla H. and Pickett M. D., "SPICE modeling of memristors", in *2011 IEEE International Symposium of Circuits and Systems*, May 2011.

[32] Yakopcic C., Taha T. M., Subramanyam G., Pino R. E. and Rogers S., "A memristor device model", in *IEEE Electron Device Letters*, v. 32, September 2011.

[33] Hamann C. H., Hamnett A. and Vielstich W., "Electrochemistry", *Wiley-VCH*, ed. 2, February 2007.

[34] Simmons J. G., "Generalized formula for the electric tunnel effect between similar electrodes separated by a thin insulating film", in *Journal of Applied Physics*, v. 34, June 1963.

[35] Valov I., Waser R., Jameson J. R. and Nozicki M. N., "Electrochemical metallization memories - fundamentals, applications, prospects", in *Nanotechnology*, v. 22, May 2011.

[36] Ambrogio S., Magyari-Köpe B., Onofrio N., Islam M., Duncan D., Nishi Y. and Alejandro Strachan A., "Modeling resistive switching materials and devices across scales", in *Journal of Electroceramics*, v. 39, June 2017.

[37] Zhao X., Li M., Xu H., Wang Z., Zhang C., Liu W., Ma J. and Liu Y., "Forming-free electrochemical metallization resistive memory devices based on nanoporous TiOxNy thin film", in *Journal of Alloys and Compounds*, v. 656, January 2016.

[38] Menzel S., Tappertzhofen S., Waser R., Valov I., "Switching kinetics of electrochemical metallization memory cells", *Phys. Chem. Chem. Phys.*, v. 15, March 2013.

[39] Karpov V. G., Kryukov Y. A., Mitra M., and Karpov I. V., "Crystal nucleation in glasses of phase change memory", in *Journal of Applied Physics*, v. 104, September 2008.

[40] Waser R., Bruchhaus R. and Menzel S., "Nanoelectronics and Information Technology", *Wiley-VCH*, ed. 3, 2012.

[41] Menzel S., Waters M., Marchewka A., Böttger U., Dittmann R. and Waser R., "Origin of the ultra-nonlinear switching kinetics in oxide-based resistive switches", in *Advanced Functional Materials*, v. 21, September 2011.

[42] Sondheimer E. H., "The mean free path of electrons in metals", in *Advances in Physics*, v. 50, 2001.

[43] Tappertzhofen S., Valov I. and Waser R., "Quantum conductance and switching kinetics of AgI-based microcrossbar cells", in *Nanotechnology*, v. 23, March 2012.

[44] Menzel S., Böttger U.and Waser R., "Simulation of multilevel switching in electrochemical metallization memory cells", in *Journal of Applied Physics*, v. 111, January 2012.

[45] Jeong, D.S., Schroeder, H., Breuer, U. and Waser, R., "Characteristic electroforming behavior in Pt/TiO2/Pt resistive switching cells depending on atmosphere", in *J. Appl. Phys.*, v. 104, December 2008.

[46] Waser R. and Aono M., "Nanoionics-based resistive switching memories", in *Nanoscience and Technology*, August 2009.

[47] Li, W.X., Österlund, L., Vestergaard, E.K., Vang, R.T., Matthiesen, J., Pedersen, T.M., Lasgsgaard, E., Hammer, B., and Besenbacher, F., "Oxidation of Pt(110)", in *Physical Review Letters*, October 2004.

[48] Waser R., "Bulk Conductivity and Defect Chemistry of Acceptor-Doped Strontium Titanate in the Quenched State", in *Journal of the American Ceramic Society*, v. 74, August 1991.

[49] Koveshnikov S., Matthews K., Min K., Gilmer D., Sung M., Deora S., Li H., Gausepohl S., Kirsch P. and Jammy R., "Real-time study of switching kinetics in integrated 1T/ HfOx 1R RRAM: Intrinsic tunability of set/reset voltage and trade-off with switching time", in *2012 International Electron Devices Meeting*, December 2012.

[50] Ielmini D., Nardi F., and Balatti S., "Evidence of voltage-driven set/reset processes in bipolar switching RRAM", in *IEEE Trans. Electron Devices*, v. 59, n. 8, August 2012.

[51] Diokh T., Le-Roux E., Jeannot S., Gros-Jean M., Candelier P., Nodin J. F., Jousseaume V., Perniola L., Grampeix H., Cabout T., Jalaguier E., Guillermet M. and De Salvo B., "Investigation of the impact of the oxide thickness and RESET conditions on disturb in HfO2-RRAM integrated in a 65nm CMOS technology", in *2013 IEEE International Reliability Physics Symposium*, April 2013.

[52] S. Yu , Y. Wu , H. Wong, "Conduction mechanism of TiN/HfOx/Pt resistive switching memory: A trap-assisted-tunneling model", in *Appl. Phys. Lett.*, v. 99, August 2011.

[53] Cao M. G., Chen Y. S., Sun J. R., Shang D. S., Liu L. F, Kang J. F. and Shen B. G., "Nonlinear dependence of set time on pulse voltage caused by thermal accelerated breakdown in the Ti/HfO 2 /Pt resistive switching devices", in *Appl. Phys. Lett.*, v. 101, November 2012.

[54] Alibart F., Gao L., Hoskins B. D. and Strukov D. B., "High precision tuning of state for memristive devices by adaptable variation-tolerant algorithm", in *Nanotechnology*, v. 23, January 2012.

[55] Nishi Y., Schmelzer S., Böttger U. and Waser R., "Weibull analysis of the kinetics of resistive switches based on tantalum oxide thin films", in *2013 Proceedings of the European Solid-State Device Research Conference*, September 2013.

[56] Nishi Y., Menzel S., Fleck K., Böttger U. and Waser R., "Origin of the SET kinetics of the resistive switching in tantalum oxide thin films", in *IEEE Electron Device Letters*, v. 35, February 2014.

[57] Schmelzer S., "Ultra thin oxide films for dielectric and resistive memory applications", *Doctoral thesis*, *RWTH Aachen University*, February 2013.

[58] Safi I. "Recent Aspects concerning DC Reactive Magnetron Sputtering of Thin Films: A Review." in *Surface & Coatings Technology*, v. 127, 2000.

[59] Gudmundsson J. T., "Physics and technology of magnetron sputtering discharges.", in *Plasma Sources Science & Technology*, v. 29, September 2020.

[60] Horwitz C. M., "Rf sputtering–voltage division between two electrodes", in *Journal of Vacuum Science & Technology A1*, v. 60, 1983

[61] Kelly P. J., and Arnell R. D., "Magnetron sputtering: a review of recent developments and applications." in *Vacuum*, v. 56, March 2000.

[62] Mandracci P., "Lecture notes", *Politecnico di Torino*, 2019.

[63] Coloma Ribera R., "Growth and thermal oxidation of Ru and ZrO2 thin films as oxidation protective layers", March 2017.

[64] Yasaka M., "X-ray thin-film measurement techniques V: X-ray reflectivity measurement", in *The Rigaku Journal*, v. 26, 2010.

[65] Agustín-Sáenz C. et al., "Broadband antireflective coating stack based on mesoporous silica by acid-catalyzed sol-gel method for concentrated photovoltaic application", in *Solar Energy Materials and Solar Cells*, June 2018.

[66] Kiessig H., "Untersuchungen zur totalreflexion von röntgenstrahlen.", in *Ann. Phys.*, v. 402, 1931.

[67] Hyun-Su K., "Interference lithography with extreme ultraviolet light", *Doctoral thesis*, *University of Southampton*, December 2016.

[68] Souk J. et al., "Flat panel display manufacturing", *Wiley*, August 2018.

[69] Bornside D.E., Macosko C.W., Scriven L.E., "On the modeling of spin coating", in *Journal of Imaging Technology*, v. 13, 1987.

[70] Haberfehlner G., "3D nanoimaging of semiconductor devices and materials by electron tomography", *Doctoral thesis*, *Université de Grenoble*, September 2013.

[71] Mack C. A., "Field guide to optical lithography", *SPIE*, 2006.

[72] Bellah M., Christensen S. M., Iqbal S.M, "Nanostructures for medical diagnostics", in *Journal of nanomaterials*, v. 2012, 2012.

[73] Galeano J. A., Sandoz P., Zarzycki A., Robert L. and Jaramillo J. M., "Microfabrication of position reference patterns onto glass microscope slides for high-accurate analysis of dynamic cellular events", in *TecnoLógicas*, v. 20, n. 39, 2017.

[74] Leitao D. C., Macedo R. J., Silva A. V., Hoang D. Q., MacLaren D. A., McVitie S., Cardoso S., and Freitas P. P., "Optimization of Exposure Parameters for Lift-off Process of Sub-100 Features Using a Negative Tone Electron Beam Resist.", in *12th IEEE International Conference on Nanotechnology*, August 2012.

[75] Microchemicals®, "Fundamentals of microstructuring", *Application notes.*

[76] Elgrishi N., Rountree K. J., McCarthy B. D., Rountree E. S., Eisenhart T. T., and Dempsey J. L., "A Practical Beginner's Guide to Cyclic Voltammetry.", in *Journal of Chemical Education*, v. 95, 2018.

[77] Tappertzhofen S., Menzel S., Valov I., and Waser R., "Redox Processes in Silicon Dioxide Thin Films Using Copper Microelectrodes.", in *Applied Physics Letters*, v. 99, November 2011.

[78] Bard A. and Faulkner L., "Electrochemical Methods: Fundamentals and Applications", *John Wiley and Sons*, 2001.

[79] Kim W., Menzel S., Wouters D. J., Guo Y., Robertson J., Roesgen B., Waser R., and Rana V., "Impact of Oxygen Exchange Reaction at the Ohmic Interface in Ta2O5-based ReRAM Devices.", in *Nanoscale*, v. 8, August 2016.

[80] Guarnieri V., Biazi L., Marchiori R., Lago A., "Platinum metallization for MEMS application. Focus on coating adhesion for biomedical applications.", *Biomatter*, v. 4, April 2014.

[81] Celano U., Goux L., Belmonte A., Opsomer K., Detavernier C., Jurczak M., and Vandervorst W., "Conductive filaments multiplicity as a variability factor in CBRAM.", in *2015 IEEE International Reliability Physics Symposium*, April 2015

[82] Al-Mamun M., Chakraborty A., Li Y., and Orlowski M. K., "Impact of surface roughness of the electrodes on the resistive switching in ReRam devices", in *ECS Trans.*, v. 97, 2020.

[83] Tappertzhofen S., Mündelein H., Valov I. and Waser R., "Nanoionic transport and electrochemical reactions in resistively switching silicon dioxide", in *Nanoscale*, v. 4, March 2012.

[84] Lübben M. and Valov I., "Active electrode redox reactions and device behavior in ECM type resistive switching memories.", in *Advanced Electronic Materials*, v. 5, september 2019.

[85] Jamilpanah L. and Mohseni S. M., "Facilitate measurement of electrochemical reactions in redox-based memristors by simply thickening the electrolyte layer.", in *Physica Status Solidi, PSS-RRL, Rapid Research Letters*, v. 12, March 2018.

[86] Hust J. G., Lankford A. B., "Thermal conductivity of aluminum, copper, iron, and tungsten for temperatures from 1 K to the melting point.", *National Bureau of Standards, Boulder, CO (USA)*, June 1984.

[87] Tsuruoka T., Valov I., Tappertzhofen S., Van Den Hurk J., Hasegawa T., Waser R., and Aono M., "Redox Reactions at Cu,Ag/Ta2O5 Interfaces and the Effects of Ta2O5 Film Density on the Forming Process in Atomic Switch Structures.", in *Advanced Functional Materials*, v. 25, June 2015.

[88] Kweon S. Y., Choi S. K., Yeom S. J., and Roh J. S., "Platinum Hillocks in Pt/Ti Film Stacks Deposited on Thermally Oxidized Si Substrate.", in *Japanese Journal of Applied Physics*, v. 40, June 2001.

Appendix A

Measured data

Set Voltage					
Mean [V]		St.Dev. [V]		St.Dev. [%]	
HP	LP	HP	LP	HP	LP
0.658	0.736	0.126	0.296	19.210	40.251
0.738	0.969	0.143	0.264	19.417	27.257
0.654	0.931	0.150	0.709	23.004	76.200
0.591	0.931	0.159	0.709	26.940	76.200
0.662	0.688	0.171	0.179	25.788	25.963
0.666	0.820	0.355	0.237	53.340	28.898
0.688	1.012	0.199	0.365	28.989	36.080
0.573	0.846	0.201	0.373	35.139	44.142
0.649	1.182	0.221	0.554	34.031	46.893
0.835	0.872	0.222	0.439	26.630	50.309
0.711	0.982	0.203	0.233	28.501	23.746
0.497	0.911	0.239	0.314	47.998	34.511
0.466	0.928	0.131	0.246	28.192	26.535
0.478	-	0.154	-	32.225	-
0.600	-	0.181	-	30.215	-
0.823	-	0.213	-	25.917	-
0.686	-	0.178	-	25.862	-
0.689	-	0.196	-	28.498	-
0.841	-	0.276	-	32.860	-
0.814	-	0.211	-	25.862	-
0.778	-	0.234	-	30.038	-
0.821	-	0.235	-	28.595	-
0.658	-	0.170	-	25.768	-
0.700	-	0.170	-	24.344	-
0.655	-	0.188	-	28.644	-

Reset Voltage					
Mean [V]		St.Dev. [V]		St.Dev. [%]	
HP	LP	HP	LP	HP	LP
-0.288	-0.298	0.083	0.078	28.934	26.250
-0.324	-0.383	0.170	0.124	52.338	32.502
-0.339	-0.427	0.167	0.104	49.234	24.436
-0.244	-0.427	0.040	0.104	16.238	24.436
-0.284	-0.374	0.104	0.115	36.681	30.841
-0.257	-0.294	0.069	0.077	26.989	26.281
-0.251	-0.434	0.072	0.122	28.486	28.115
-0.221	-0.438	0.058	0.128	26.050	29.183
-0.237	-0.441	0.055	0.156	23.347	35.329
-0.287	-0.318	0.077	0.078	26.750	24.632
-0.262	-0.290	0.046	0.129	17.761	44.351
-0.229	-0.292	0.079	0.074	34.428	25.475
-0.199	-0.267	0.059	0.045	29.822	16.769
-0.210	-	0.046	-	21.970	-
-0.215	-	0.041	-	19.223	-
-0.258	-	0.052	-	20.021	-
-0.232	-	0.037	-	15.808	-
-0.296	-	0.089	-	30.135	-
-0.283	-	0.083	-	29.326	-
-0.276	-	0.080	-	29.115	-
-0.320	-	0.126	-	39.343	-
-0.243	-	0.070	-	28.878	-
-0.258	-	0.101	-	39.374	-
-0.243	-	0.093	-	38.258	-
0.655	-	0.188	-	28.644	-

Table A.1: *Set and reset voltages statistics data. Mean value, absolute and percentual standard deviation (St.Dev.) are reported. Each row shows data from a single device.*

High Resistance state					
Mean [Ω]		**St.Dev.** [Ω]		**St.Dev.** [%]	
HP	**LP**	**HP**	**LP**	**HP**	**LP**
2.471E+04	4.730E+05	4.589E+04	2.726E+06	185.709	576.375
3.258E+04	1.182E+05	1.589E+05	1.546E+05	487.629	130.797
1.232E+04	4.478E+05	1.731E+04	2.729E+06	140.457	609.301
1.247E+04	4.478E+05	7.973E+03	2.729E+06	63.932	609.301
9.845E+03	6.121E+04	7.937E+03	9.293E+04	80.616	151.809
1.848E+04	7.706E+05	1.196E+04	3.827E+06	64.725	496.613
1.786E+04	4.937E+05	1.103E+04	2.733E+06	61.748	553.486
2.249E+04	1.828E+05	1.173E+04	4.437E+05	52.152	242.780
1.607E+04	1.845E+05	8.888E+03	3.782E+05	55.310	205.055
2.042E+04	8.938E+05	1.225E+04	3.844E+06	59.988	430.038
1.482E+04	9.467E+05	8.985E+03	3.849E+06	60.618	406.560
1.735E+04	1.773E+05	8.444E+03	3.557E+05	48.662	200.673
1.161E+04	2.323E+05	8.031E+03	4.242E+05	69.148	182.620
1.412E+04	-	7.341E+03	-	51.979	-
2.150E+04	-	1.112E+04	-	51.708	-
2.582E+04	-	1.264E+04	-	48.969	-
1.728E+04	-	8.539E+03	-	49.415	-
1.850E+04	-	9.987E+03	-	53.995	-
1.617E+04	-	1.238E+04	-	76.548	-
1.749E+04	-	1.063E+04	-	60.758	-
1.753E+04	-	1.044E+04	-	59.547	-
1.346E+04	-	1.122E+04	-	83.337	-
9.699E+03	-	4.669E+03	-	48.139	-
1.993E+04	-	1.214E+04	-	60.917	-
2.306E+04	-	1.241E+04	-	53.825	-

Table A.2: *HRS resistance statistics data. Mean value, absolute and percentual standard deviation (St.Dev.) are reported. Each row shows data from a single device.*

Low Resistance state					
Mean [Ω]		**St.Dev.** [Ω]		**St.Dev.** [%]	
HP	**LP**	**HP**	**LP**	**HP**	**LP**
160.947	718.107	69.395	4176.390	43.117	581.583
165.660	507.540	124.990	1999.155	75.449	393.891
185.836	197.805	178.050	98.465	95.811	49.779
188.895	197.805	63.246	98.465	33.482	49.779
186.315	3339.215	88.388	23702.746	47.440	709.830
169.450	208.205	60.600	43.758	35.763	21.017
240.573	168.989	517.151	64.600	214.966	38.228
184.536	785.964	57.160	4617.260	30.975	587.464
166.355	119.312	64.825	43.731	38.968	36.653
160.020	199.834	86.419	71.620	54.005	35.840
201.503	307.023	104.164	1011.266	51.693	329.378
186.884	219.472	83.132	102.715	44.483	46.801
269.396	171.264	666.263	56.239	247.317	32.838
205.987	-	211.428	-	102.641	-
149.997	-	59.553	-	39.703	-
125.773	-	74.493	-	59.228	-
148.170	-	62.681	-	42.304	-
158.740	-	74.677	-	47.043	-
189.257	-	146.180	-	77.239	-
155.762	-	90.354	-	58.008	-
203.085	-	121.831	-	59.990	-
177.281	-	114.236	-	64.438	-
176.301	-	93.720	-	53.159	-
146.291	-	71.126	-	48.619	-
193.820	-	291.313	-	150.301	-

Table A.3: *LRS resistance statistics data. Mean value, absolute and percentual standard deviation (St.Dev.) are reported. Each row shows data from a single device.*

Resistance Ratio (R_{HRS}/T_{LRS})					
Mean		**St.Dev.**		**St.Dev. [%]**	
HP	**LP**	**HP**	**LP**	**HP**	**LP**
2.047E+02	3.374E+03	4.395E+02	1.879E+04	214.665	557.013
3.240E+02	6.043E+02	1.621E+03	9.281E+02	500.155	153.586
1.001E+02	1.736E+03	1.650E+02	9.464E+03	164.783	545.154
8.221E+01	1.736E+03	8.789E+01	9.464E+03	106.904	545.154
7.001E+01	2.444E+02	7.434E+01	3.767E+02	106.182	154.115
1.478E+02	4.555E+03	1.572E+02	2.368E+04	106.339	519.836
1.395E+02	4.512E+03	1.199E+02	2.735E+04	85.968	606.201
1.388E+02	1.147E+03	1.009E+02	3.072E+03	72.663	267.938
1.193E+02	1.491E+03	1.017E+02	2.660E+03	85.238	178.375
1.724E+02	5.946E+03	1.501E+02	2.909E+04	87.030	489.248
9.913E+01	6.655E+03	9.975E+01	2.916E+04	100.627	438.226
1.080E+02	1.076E+03	7.552E+01	2.389E+03	69.901	221.954
6.727E+01	1.576E+03	5.195E+01	3.349E+03	77.230	212.478
9.051E+01	-	6.649E+01	-	73.454	-
1.695E+02	-	1.197E+02	-	70.635	-
3.041E+02	-	2.494E+02	-	82.000	-
1.560E+02	-	1.342E+02	-	86.065	-
1.574E+02	-	1.420E+02	-	90.252	-
1.858E+02	-	2.258E+02	-	121.512	-
1.618E+02	-	1.447E+02	-	89.441	-
1.449E+02	-	1.738E+02	-	119.896	-
1.269E+02	-	1.970E+02	-	155.288	-
7.817E+01	-	6.933E+01	-	88.691	-
2.012E+02	-	1.953E+02	-	97.073	-
1.917E+02	-	1.459E+02	-	76.105	-

Table A.4: *Resistance ratio statistics data. Mean value, absolute and percentual standard deviation (St.Dev.) are reported. Each row shows data from a single device.*

Forming Voltage [25 µm]					
Mean [V]		**St.Dev. [V]**		**St.Dev. [%]**	
HP	**LP**	**HP**	**LP**	**HP**	**LP**
3.942	3.662	1.107	0.570	28.096	15.802
3.774	3.454	1.151	0.279	30.487	8.091
4.046	4.474	0.857	0.919	21.190	20.536
5.012	3.456	1.017	0.434	20.283	12.552
4.284	4.818	0.772	0.489	18.0174	10.141
3.502	-	0.864	-	24.666	-

Forming Voltage [50 µm]					
Mean [V]		**St.Dev. [V]**		**St.Dev. [%]**	
HP	**LP**	**HP**	**LP**	**HP**	**LP**
3.522	2.850	1.500	0.856	42.598	30.032
4.102	2.848	0.859	0.573	20.932	20.106
3.840	4.117	1.027	0.763	26.733	18.526
4.597	3.897	0.948	1.036	20.630	26.579
4.138	4.816	0.774	0.516	18.714	10.719
3.2224	-	0.836	-	25.945	-

Forming Voltage [100 µm]					
Mean [V]		**St.Dev. [V]**		**St.Dev. [%]**	
HP	**LP**	**HP**	**LP**	**HP**	**LP**
3.163	2.548	1.239	1.030	39.184	40.418
3.968	2.555	0.628	0.744	15.832	29.102
3.895	4.055	0.785	0.810	20.155	19.972
4.725	4.183	0.236	0.675	4.988	16.132
4.530	4.515	0.319	0.812	7.044	17.990
3.200	-	1.150	-	35.927	-

Table A.5: *Electroforming statistics data for devices with 25 µm, 50 µm and 100 µm edge top electrodes. Mean value, absolute and percentual standard deviation (St.Dev.) are reported. Each row shows data from a sample.*

Set time										
V_{app} [V]	**0.7**		**0.95**		**1.20**		**1.45**		**1.70**	
Purity	**LP**	**HP**	**LP**	**HP**	**LP**	**HP**	**LP**	**HP**	**LP**	**HP**
t_{set} [s]	2.620E+00	5.566E+00	6.420E-02	1.438E-01	2.600E-05	2.600E-04	6.000E-06	3.880E-03	6.000E-05	9.970E-03
	1.000E-02	1.576E+00	6.092E-02	2.434E+00	1.900E-03	8.000E-06	2.600E-05	9.960E-03	6.000E-06	1.000E-05
	1.500E-02	1.760E-01	6.940E-02	4.438E-01	2.259E-02	4.640E-04	1.150E-06	1.800E-05	1.800E-06	1.000E-05
	8.600E-01	3.264E+00	6.365E-02	4.130E+00	3.980E-03	3.600E-05	2.175E-04	2.600E-05	3.000E-06	1.200E-05
	5.480E+00	1.142E+01	1.160E-04	2.732E-01	1.042E-02	5.937E-02	6.660E-02	6.000E-06	3.000E-07	1.200E-05
	5.200E-01	2.388E+00	1.600E-02	4.044E-01	1.380E-03	3.930E-03	4.867E-02	1.400E-05	5.500E-07	2.000E-06
	6.000E-03	5.322E+00	1.400E-05	3.369E+00	5.661E-02	2.760E-04	3.000E-02	1.400E-05	8.000E-06	6.800E-05
	4.327E+00	3.292E+00	2.600E-05	1.545E+00	7.200E-05	6.000E-06	9.343E-04	4.000E-06	5.000E-05	1.400E-05
	1.007E+01	7.720E+00	7.200E-05	6.140E+00	6.000E-06	3.167E-02	4.422E-04	1.650E-03	4.000E-07	1.200E-05
	2.987E+00	7.480E+00	2.400E-05	9.800E-02	1.150E-06	7.740E-04	2.175E-05	2.000E-06	7.500E-07	2.000E-06
	2.027E+00	5.269E+00	1.600E-05	5.600E-02	2.600E-05	1.600E-05	1.200E-05	6.000E-06	4.000E-07	1.000E-05
	2.110E-01	8.329E+00	7.800E-01	3.000E-01	6.000E-06	3.010E-03	4.867E-02	3.600E-05	1.000E-06	1.000E-05
	1.345E+00	4.569E+00	5.600E-01	6.632E+00	6.000E-06	9.060E-03	6.000E-06	1.202E-02	4.430E-05	1.000E-05
	7.285E+00	1.747E+01	1.880E-03	1.161E+00	1.200E-05	2.400E-05	8.000E-06	1.000E-05	2.800E-03	4.000E-06
	1.397E+01	9.023E+00	1.799E+00	2.259E+00	1.000E-05	3.800E-05	5.000E-07	1.000E-05	1.410E-03	4.400E-05
	2.852E-01	9.649E+00	6.593E-01	2.900E-01	1.400E-05	4.600E-05	6.000E-07	4.000E-06	5.000E-08	1.200E-05
	4.785E+00	2.623E+00	6.652E-02	1.028E+00	1.000E-05	3.140E-03	1.200E-05	1.600E-05	1.000E-05	6.000E-06
	2.205E+00	3.673E+00	5.707E+00	7.092E+00	2.259E-02	1.192E-02	1.400E-05	1.000E-05	1.850E-06	1.400E-05
	8.000E-02	7.423E+00	5.707E+00	8.839E+00	4.390E-03	3.050E-03	8.000E-06	7.147E-02	6.160E-04	1.000E-05
	3.300E+00	8.689E+00	5.065E-01	1.909E+00	1.800E-05	2.000E-05	9.960E-03	4.902E-02	1.410E-03	2.850E-03
	-	-	-	-	1.400E-05	1.400E-05	1.400E-05	-	4.430E-05	-
	-	-	-	-	1.200E-05	1.600E-05	2.689E-02	-	6.160E-04	-
	-	-	-	-	1.000E-05	1.800E-05	2.431E-02	-	1.590E-05	-
	-	-	-	-	7.969E-02	-	2.918E-02	-	1.000E-05	-
	-	-	-	-	3.930E-03	-	3.081E-02	-	6.060E-05	-
	-	-	-	-	1.100E-03	-	8.260E-03	-	9.800E-07	-
	-	-	-	-	1.000E-06	-	6.915E-02	-	6.225E-06	-
	-	-	-	-	-	-	1.600E-05	-	3.554E-05	-
	-	-	-	-	-	-	1.000E-05	-	-	-
	-	-	-	-	-	-	1.800E-06	-	-	-
	-	-	-	-	-	-	3.000E-06	-	-	-
	-	-	-	-	-	-	1.850E-06	-	-	-

Table A.6: *Set time (t_{set}) measured data at different applied voltages (V_{app}).*